



UNIVERSITÀ DEGLI STUDI DI PADOVA

Dipartimento di Geoscienze
Direttore Prof. ssa Cristina Stefani

TESI DI LAUREA MAGISTRALE IN GEOLOGIA E GEOLOGIA TECNICA

Stima della potenza dissipata per attrito durante i terremoti: confronto tra faglie sperimentali e naturali.

**Estimate of frictional seismic power dissipation from
natural and experimental faults**

Relatore: Prof. Giulio Di Toro
Correlatori: Prof. Stefan Nielsen
Prof. Ashley W. Griffith

Laureanda: Angela Castagna

Mat: 1014299

ANNO ACCADEMICO 2012 / 2013

Contents

Abstract

Riassunto

Chapter 1 – Introduction : About earthquakes

- 1.1 Basics of earthquakes mechanics
- 1.2 Energy partitioning and power dissipation during earthquakes
- 1.3 Pseudotachylytes microroughness and frictional power dissipation

Chapter 2 – Methods

- 2.1 Field methods
 - 2.1.1 *Ortorectification and photomosaics*
- 2.2 Experimental methods
 - 2.1.2 *SHIVA and sample preparation*
- 2.3 Determination of microroughness
 - 2.3.1 *ArcGIS*
 - 2.3.2 *MatLab script*

Chapter 3 – Microroughness in natural faults (Gole Larghe Fault Zone)

- 3.1 Regional setting
 - 3.1.1 *The Adamello batholiths*
 - 3.1.2 *The Gole Larghe Fault Zone*
- 3.2 Microroughness in natural pseudotachylytes
 - 3.2.1 *The selected faults*
 - 3.2.2 *Microroughness in pseudotachylyte injection and fault veins*

Chapter 4 – Microroughness in experimental faults

- 4.1 Experiments with SHIVA
 - 4.1.1 *Mechanical data*
 - 4.2.2 *Microroughness in experimental pseudotachylytes*

Chapter 5 – Discussion

- 5.1 Comparison between natural and experimental microroughness
 - 5.1.1 *Microroughness in natural samples*
 - 5.1.2 *Microroughness in experimental samples*
 - 5.1.3 *Experimental microroughness measurements from optical and BSE-SEM images*
 - 5.1.4 *Comparison between natural and experimental samples*
 - 5.1.5 *Estimate of frictional power dissipated during earthquakes*

Chapter 6 – Conclusions

ABSTRACT

In the last decades, several approaches were applied to understand the physics of seismic faulting. In the field, the recognition of pseudotachylytes (solidified friction melts produced during seismic slip) which record seismic ruptures along a fault allowed to estimate, from exhumed faults, several earthquake source parameters, including the coseismic shear stress and the weakening distance that characterized the fault instability. In the laboratory, rotary shear rock friction apparatus allow to impose to rock samples of the size of glass a wide range of slip, slip velocities and normal stresses which approximate seismic deformation conditions. In particular, the possibility to acquire precise and accurate mechanical data, allows the determination of others earthquake source parameters such as the frictional power density (the product of slip rate with shear stress). This information is out of the range of seismological investigations, though is the power dissipated on a fault that controls earthquake-related processes (for instance, the temperature increase in the slipping zone is proportional to the power). In this thesis, we performed the microstructural analysis of natural pseudotachylytes collected from injection veins (tensile cracks) and fault veins (from extensional, neutral and compressional structural domains) and of artificial pseudotachylytes produced in the laboratory under controlled conditions (we used SHIVA, a rotary shear apparatus recently installed at the Istituto Nazionale di Geofisica e Vulcanologia in Rome). The goal was to use the microroughness of the pseudotachylyte-wall rock boundary as a gage of the frictional power dissipated on a fault during seismic slip. In fact, theoretical work (Nielsen et al., 2010) predicts that smoother is the fault surface, higher was the coseismic frictional power dissipated on the fault. To analyze the microroughness, we draw detailed profiles from optical microscope and Back Scatter Scanning Electron Microscope images of the pseudotachylyte-wall rock boundary in natural and experimental samples. The profiles were quantitatively described with a MatLab script by means of a characteristic asperity height (ω_0) and characteristic radii of a sphere that mimics the asperity shape (λ_{ave}). Our data set shows that ω_0 decreases with increasing frictional power density in artificial pseudotachylytes, and varies with the structural domain in natural pseudotachylytes, being the highest in tensional cracks (injection veins, where the frictional power dissipated is thought to be negligible) and the smallest in compressional domains (along fault veins, where the frictional power dissipated is higher). However, the microroughness of artificial pseudotachylyte has ω_0 values which are 3 to 10 times smaller than the ω_0 of the natural pseudotachylytes, independently of the structural domain of provenience of the latter. We speculate that this “systematic” difference, which impedes the quantitative determination of the power dissipated in natural samples, reflects the inherited roughness acquired during formation and evolution of natural faults before seismic faulting. Shortly, given the same length parallel to the slip vector, natural faults are rougher than artificial fault surfaces used in the laboratory. Though the results

of this thesis are extremely promising, additional theoretical and experimental work is required in order to gain from the determination of the microroughness in pseudotachylytes, quantitative estimates of the frictional power dissipated during an ancient seismic event at seismogenic depths.

RIASSUNTO

Negli ultimi decenni, per comprendere i meccanismi attivi su una faglia durante un evento sismico, sono stati impiegati diversi approcci. In campagna, il riconoscimento delle pseudotachiliti (fusi di frizione solidificati prodotti durante scivolamento su faglia) come segno inequivocabile di un antico evento sismico registrato da una faglia, ha permesso di ricavare importanti parametri della sorgente sismica, come la resistenza frizionale cosismica, la distanza di indebolimento (che è un parametro critico dell'instabilità delle faglie), il bilancio energetico, ecc. In laboratorio, l'impiego di apparati sperimentali tipo rotary che riproducono i rigetti (anche di diversi metri), le velocità di scivolamento (ca. 1 m/s) e gli sforzi normali tipici di un terremoto, ha consentito di misurare diversi parametri della sorgente sismica, tra cui la potenza dissipata per attrito (prodotto della velocità di scivolamento per la resistenza frizionale cosismica) durante un terremoto. Quest'ultimo parametro non è ricavabile dalle indagini sismologiche, benché sia la potenza dissipata su di una faglia che condiziona l'evoluzione di un evento sismico. In questa tesi, abbiamo effettuato un'analisi microstrutturale di campioni naturali di pseudotachiliti raccolti in diversi domini strutturali (sfruttando la rugosità alla scala metrica delle faglie) e campioni sperimentali prodotti con SHIVA, un apparato tipo rotary installato presso l'Istituto Nazionale di Geofisica e Vulcanologia a Roma. L'obiettivo è di trovare una correlazione tra l'evoluzione della microrugosità del contatto tra pseudotachilite e roccia incassante con la potenza frizionale dissipata; in laboratorio, con la potenza misurata durante gli esperimenti, in natura con i diversi domini strutturali: puramente tensionali (nessuna potenza frizionale dissipata), estensionale (bassa potenza), neutrale (media potenza) e compressionale (alta potenza dissipata). Infatti, modelli teorici (Nielsen et al., 2010) prevedono che la microrugosità decresca all'aumentare della potenza frizionale dissipata su di una faglia. Per misurare la microrugosità, abbiamo tracciato i profili del contatto pseudotachilite-roccia incassante (naturali e sperimentali) da immagini raccolte al microscopio ottico e al microscopio a scansione elettronica. Con uno script di MatLab abbiamo quantificato la microrugosità mediante due parametri, l'altezza caratteristica delle asperità (ω_0) e il raggio medio caratteristico di curvatura delle sfere che riproducono le asperità (λ_{ave}). I dati raccolti mostrano che nelle pseudotachiliti sperimentali, ω_0 decresce con la potenza dissipata e che nelle pseudotachiliti naturali, ω_0 decresce passando da un dominio strutturale puramente tensionale ad un dominio strutturale compressionale. Ma ω_0 è da 3 a 10 volte più grande nelle pseudotachiliti naturali rispetto a quelle sperimentali. Una possibile spiegazione di questa discrepanza è che la rugosità delle faglie naturali prima dello scivolamento sismico, è circa un ordine di grandezza maggiore, a parità di lunghezza di faglia parallelamente al vettore spostamento (ca. 150 mm), dei campioni sperimentali. Questa discrepanza, dovuta alla rugosità acquisita dalle faglie naturali durante la loro evoluzione e che non può essere riprodotta in laboratorio, impedisce al momento attuale l'estrapolazione dei dati sperimentali in natura e di quantificare la potenza dissipata

nelle faglie naturali. Benché questi dati preliminari siano estremamente promettenti, è necessario un ulteriore studio teorico e sperimentale per ottenere una stima quantitativa delle potenze frizionali dissipate durante antichi eventi sismici a profondità sismogenetiche.

Chapter 1 Introduction : About earthquakes

1.1 Basics of earthquakes mechanics

When the crust is undergone to stress it deforms elastically (and plastically) and eventually it can break along faults releasing elastic energy in the form of seismic waves: the earthquake. Once the rupture propagates, at speed of about 3-5 km/s, the two wall rocks slid one against other at a slip rate of about 1 m/s (Heaton, 1990). The elastic strain energy accumulated in hundreds of years in the rocks is released in few seconds (Heaton, 1990; Scholz, 2002).

From seismological investigations, the macroscopic parameters that are possible retrieve from the seismic inversion analysis are (Kanamori and Rivera, 2006):

- the seismic moment, M_0
- the static stress drop, $\Delta\sigma_s$
- the radiated energy, E_R
- the rupture speed, V_s and directivity
- the fracture energy, E_G

The Seismic Moment (M_0) allows to measure the size of an earthquake in terms of energy (J):

$$M_0 = G A u$$

by considering the physical characteristics of the earthquakes:

G = rock shear modulus (30 GPa)

A = fault rupture area

u = average displacement

However, these “seismological” indirect techniques yield incomplete information on fundamental issues of earthquake mechanics, such as the dynamic fault strength and the energy budget of an earthquake during seismic slip remain unconstrained (Di Toro et al, 2009). So, to gain direct information on physico-chemical and mechanical processes that allow the nucleation and the slip in a fault surface, in recent years many fault-drilling projects have been undertaken in several active faults (i.e. San Andreas Fault, USA; Chelungpu Fault, Taiwan; etc.). Fault drilling allows to collect data in real-time and in-situ, such as the strain rate or the pore pressure, high-quality seismological data from seismometers located at depth and, in addition, the possibility to extract samples to analyze in

laboratory. But it has some limitations, because drilling is confined at shallow depth (< 3 km till today) and covers only a little portion of entire fault zone volume (few tens of centimeters in diameter at most!), and the costs are extremely high (about 20 M\$ for the SAFOD project or drilling of the San Andreas Fault at Parkfield, California). Another approach to get information about earthquake physics is the study of exhumed faults: by recognition of fault rock that are not undergone structural overprinting, alteration during exhumation and with presence of tight geological constraints is possible to determine ambient conditions during seismic faulting.

To date, the only fault rock recognized as a signature of an ancient earthquake is pseudotachylyte (Cowan, 1999). Tectonic pseudotachylyte is the result of solidification of friction-induced melts produced during seismic slip and consists of lithic clasts of host rock suspended in a glassy-like matrix (Shand, 1916; Sibson, 1975). To investigate how frictional melts are produced and to determine the mechanical behavior (friction coefficient *latu sense*, etc.), in the last 25 years were exploited frictional welding machines (Spray, 1987) and were specifically designed rotary shears that reproduce in the laboratory the extreme deformation conditions typical of seismic faulting (Shimamoto, 1990; Di Toro et al., 2010).

During an earthquake the potential-elastic strain energy stored in rock is released. From Kanamori (2006) the total energy budget is:

$$E_T = E_R + E_{NR}$$

where E_T is the total energy, E_R is the radiated energy and E_{NR} in the non-radiated energy. E_R can be estimated from seismic waves. The term of E_{NR} , can be divided into:

$$E_{NR} = E_F + E_G$$

where E_F is the frictional work done against resistance to sliding and is called frictional energy; while E_G is the fracture energy, the work done against the resistance to fault extension at the fault tip and includes all the energies due to plastic yielding and cracking, the latent heat for thermal pressurization, etc. E_R can be determined by seismological data, and so we can estimate the value of E_G . But the friction energy cannot be estimate. Since the absolute value of friction controls the physics of an earthquake, the estimate of the friction coefficient, frictional energy and frictional power is of some relevance to understand the physics of an earthquake. In this thesis, the attention is focused on the frictional behavior at a point of fault, to establish how much frictional power is dissipated during seismic slip. In particular, in this thesis, to determine the frictional power dissipated during seismic faulting we focused on the evolution of the roughness of the boundary between the pseudotachylyte and the wall rocks in natural and experimental rocks. When power is dissipated on a frictional interface, the temperature raises and it triggers different weakening mechanisms such as flash heating (Goldsby and Tullis, 2011)

silica-gel lubrication (Goldsby and Tullis, 2002; Di Toro et al., 2004), melt lubrication (Di Toro et al., 2006b) and several other (for a review, Di Toro et al., 2011; Niemeijer et al., 2012). From the analyses of mechanical data, it's clear how the combination of normal stress VS slip rate (MW/m^2 , power or work rate) rather than normal stress VS slip (MJ/m^2) are responsible of activation of weakening mechanism (Di Toro et al., 2012).

1.3 Pseudotachylytes microroughness and frictional power dissipation

Pseudotachylyte is the only evidence, recognized until now, of ancient seismicity in an exhumed fault. Pseudotachylytes are now recognized as the result of comminution and friction-induced melting along a fault plane during seismic slip (Spray, 1995). So, pseudotachylyte is solidified friction melt: consists of lithic clasts suspended in a glassy-cryptocrystalline matrix (Shand, 1916) of more mafic composition with respect to the host rock. Frictional melt might lubricate fault surfaces (Di Toro et al., 2006). The mafic composition is because, for instance in the case of a tonalitic rock, mineral like biotite (hydrous phase and Fe-Mg rich) has a lower melting point ($650\text{-}700^\circ\text{C}$) with respect to other minerals (in this case, quartz and plagioclase, 1700°C and 1200°C respectively): this results in selective melting of the lower melting point minerals (biotite) and an enrichment in the melt of Fe and Mg.

If we focus on the on the frictional work, \mathbf{W}_f , dissipated during seismic slip, this is partitioned in

$$\mathbf{W}_f = \mathbf{Q} + \mathbf{U}_s$$

where \mathbf{Q} is heat and \mathbf{U}_s is surface energy. Most of the work is converted to heat (\mathbf{U}_s is probably negligible compared to frictional heat, e.g., Pittarello et al., 2008), so the amount of heat production during seismic slip on the fault is

$$\mathbf{W}_f = \mu (\sigma_n - p_p) \mathbf{d} \approx \mathbf{Q}$$

where μ is the friction coefficient, σ_n is the normal stress, p_p is the pore fluid and \mathbf{d} is the co-seismic slip. The heat flux generated per unit area of the fault is (McKenzie and Brune, 1972)

$$\mathbf{q} \approx \mu (\sigma_n - p_p) \mathbf{V}$$

where \mathbf{V} is the slip rate.

The thermal penetration distance \mathbf{x} in the bounding host rock as a function of slip duration \mathbf{t} is

$$\mathbf{x} \approx (\kappa \mathbf{t})^{0.5}$$

where κ is the thermal diffusivity. It's clear that production of heat is large even for small slips, given the high normal stress and the high particle velocities localized in slipping zone. When melt is formed, part of this is squeezed out in injection vein or pool along fault plane.

In recent years, the study of melt dynamics has been the object of several studies for its implications in earthquake physics: this resulted in hundreds of dedicated experiments that reproduce seismic deformation conditions.

Nielsen et al (2008; 2010) proposed a model for frictional evolution during seismic slip in the presence of melts. A key role is the roughness of the melt-wall rock interface. The roughness depends by structural and mineralogical inhomogeneities (composition, grain size, etc.), and it is conditioned by selective melting of minerals, by the Gibbs-Thomson effect (local melting temperature increases around sharp corners of minerals, tending to eliminate them and returns a smooth profile) (Hirose and Shimamoto, 2003). Moreover, is the power dissipated at the frictional interface that should control the surface roughness. A model of a boundary interested by the evolution of temperature gradient due to the frictional power dissipated during slip is proposed by Nielsen et al (2010). In figure 3, are described the effect of a steeply (a,c) and gently (b,d) temperature gradient plus the contribution of the Gibbs-Thomson effect. The model predicts that in the case of a steeply gradient (high frictional power dissipated or high heat flow), since the isotherms are more dense than in the case of a gently gradient, the roughness of the interface results smoother as both low and high melting point minerals are melted (selective melting is less efficient). In the wall rocks, the temperature gradient is related to the shear stress (so to normal stress) and slip rate V . For the same conditions of shear stress and slip rate, Hirose and Shimamoto (2005), shown that the gradient is steeper at initial stage of experiments, and the surface evolves with slip from a quite smooth topography toward a rougher stage.

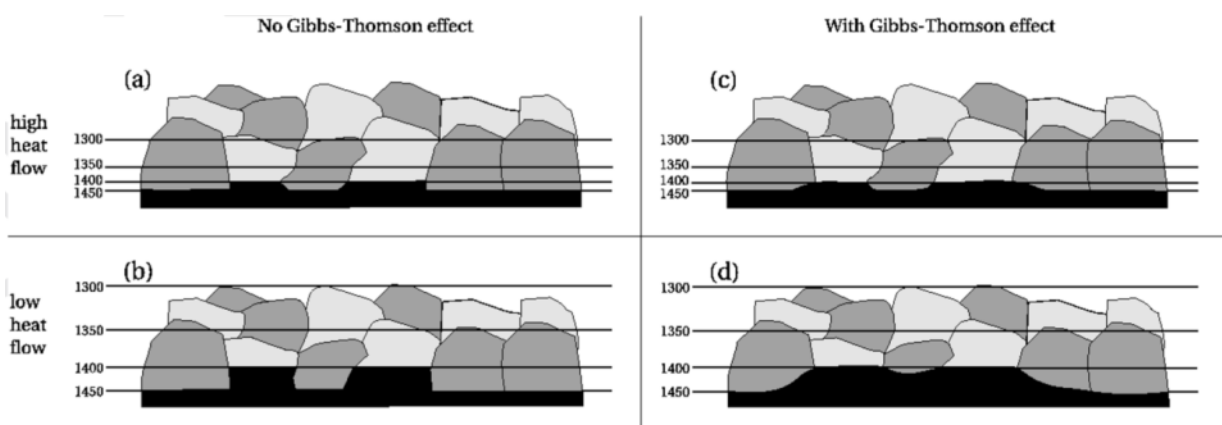


Figure 1 Melting boundary in a bi-mineral rock. Dark grains are minerals with higher melting point. The straight lines are isolines of temperature in the rock. **a)** and **b)** are steep and gently temperature gradient; **c)** and **d)** same temperature gradient but the boundary melt/rock is more smooth for the Gibbs-Thomson effect (Nielsen et al, 2010).

Microstructural analysis of fault and laboratory samples show that a minimum quantity of melt (now glass) remains trapped in the roughness of the boundary surfaces. The roughness of the boundary depends on the type of rock considered, on mineral grain size and on melting conditions (Hirose and

Shimamoto, 2003). When the melt is removed from the slip zone, contacting areas appear and are continually renewed across the surface. From Nielsen et al (2010), the convergence of these two rough elastic surfaces is investigated in a framework of Hertzian contacts, where isolated asperities supports locally plastic yield. But in this case, between the two rough- surfaces, a thin melt layer remains, impossible to squeeze out, so that the weight is supported by the asperities. To develop this concept, some theory about contact in rough surface is adapted to the case a fluid pressure present at the interface. Here we analyze the case of tonalitic rock in dry condition where a consistent layer of melt is product.

From Greenwood (1992) and Persson (2000) the frictional contact across an area \mathbf{A} can be simulated using \mathbf{N} spherical caps with average radius λ and a given probability distribution of height $\psi(z)$, and the separation between the two surfaces under a normal load \mathbf{F} is

$$\left(\frac{\omega}{\omega_0}\right)^2 = 2 \log \left(N \omega_0^{3/2} \lambda^{1/2} \frac{4}{3(1-\nu_p^2)} \frac{E}{F} \right) - 5 \log \left(\frac{\omega}{\omega_0} \right)$$

ν_p and \mathbf{E} are the Poisson ratio and the Young modulus respectively. The definition of ω , ω_0 and λ is illustrated in figure 4.

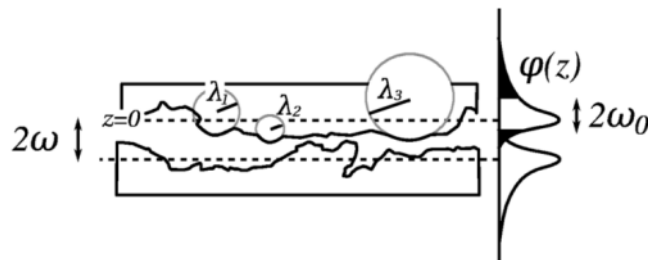


Figure 2 Definition of ω (average thickness of melt), ω_0 (characteristic elevation of asperities), λ (average radius of asperities). The dotted line represents a reference line that coincides with the average value of the elevation density distribution $\psi(z)$. Interstitial space is filled of melt and 2ω is defined as the average thickness of the melt.

According to this approach, the roughness of the melt-rock interface can be linked to the temperature gradient and consequently to the power dissipated at the frictional interface.

Chapter 2 – Methods

2.1 Field methods

2.1.1 Ortho-rectification and photomosaics

To create 2-dimensional fault profiles (intersection of the fault surfaces with the glacier-polished outcrop surface), photos were first ortho-rectified and then merged in photomosaics. Ortho-rectification is a technique which removes from the photo (1) the distortion due to spherical aberration (optical lens of the camera), (2) the effects of perspective (out-of-zenith position of the camera with respect to the ground or tilt-effect (Fig. 5a), and (3) reduces the effects due to the relief (in-homogeneities of the outcrop surface (Fig. 5b). Ortho-rectification allows to obtain not distorted images and photomosaics (by joining several ortho-rectified images) with a constant scale where the features are in their “real” position.

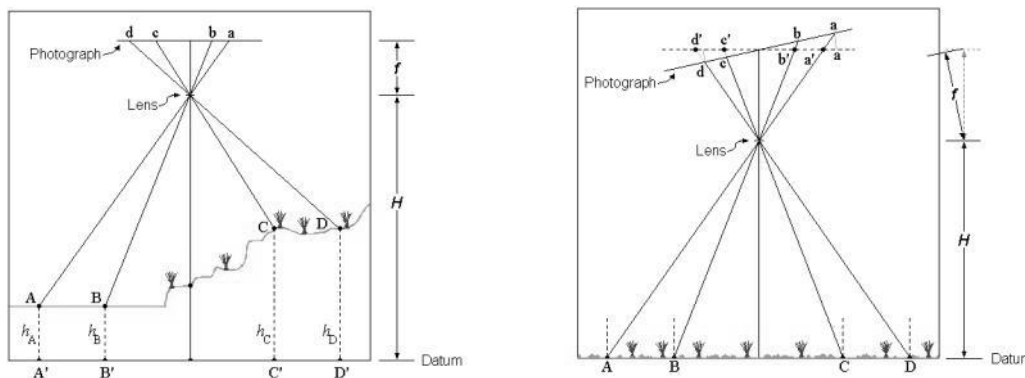


Figure 3 a) Relief effect and b) tilt effect.

2.2 Experimental methods

2.2.1 SHIVA and sample preparation

To understand mechanics of seismic faulting, in the last 45 years rock friction experiments were mainly conducted with a bi-axial and tri-axial apparatus. This experimental approach allowed the investigation of the frictional instabilities responsible of earthquake nucleation. However, the low slip rate ($<10 \mu\text{m/s}$) and displacement ($<10 \text{ mm}$) that these apparatus impose to the rock samples, do not permit to investigate physico-chemical processes triggered at seismic deformation conditions (slip rates on average of 1 m/s and displacements up to 50 m) and the rheology of fault materials under these extreme deformation conditions.

In the 1980s, installation of first high-pressure rotary apparatus by prof. Tullis, was the first attempt to obtain data under extreme deformation typical of earthquakes. Then, other rotary shear apparatus were installed in the 1990s (i.e. rotary shear apparatus HV-1 and HV-2 by T. Shimamoto, etc). Experiments performed with rotary shear allowed the identification (though some of them are still debated) of several co-seismic weakening mechanisms, including melt lubrication (Hirose and Shimamoto, 2005; Spray 2005; Di Toro et al. 2006), thermal decomposition (Han et al. 2007; Brantut et al. 2008) and silica gel lubrication (Goldsby and Tullis 2002; Di Toro et al. 2004).

In the last years, rotary shear apparatus were designed to better reproduce the slip rate, normal stress and power dissipated during seismic slip. SHIVA (Slow to High Velocity Apparatus) was installed in Rome at INGV institute in 2009. This new apparatus is the most powerful (280 kW) rotary shear installed worldwide, and can impose slip rates up to 6.5 m/s and normal stress up to 50 MPa on samples 30/50 mm int/ext in diameter.

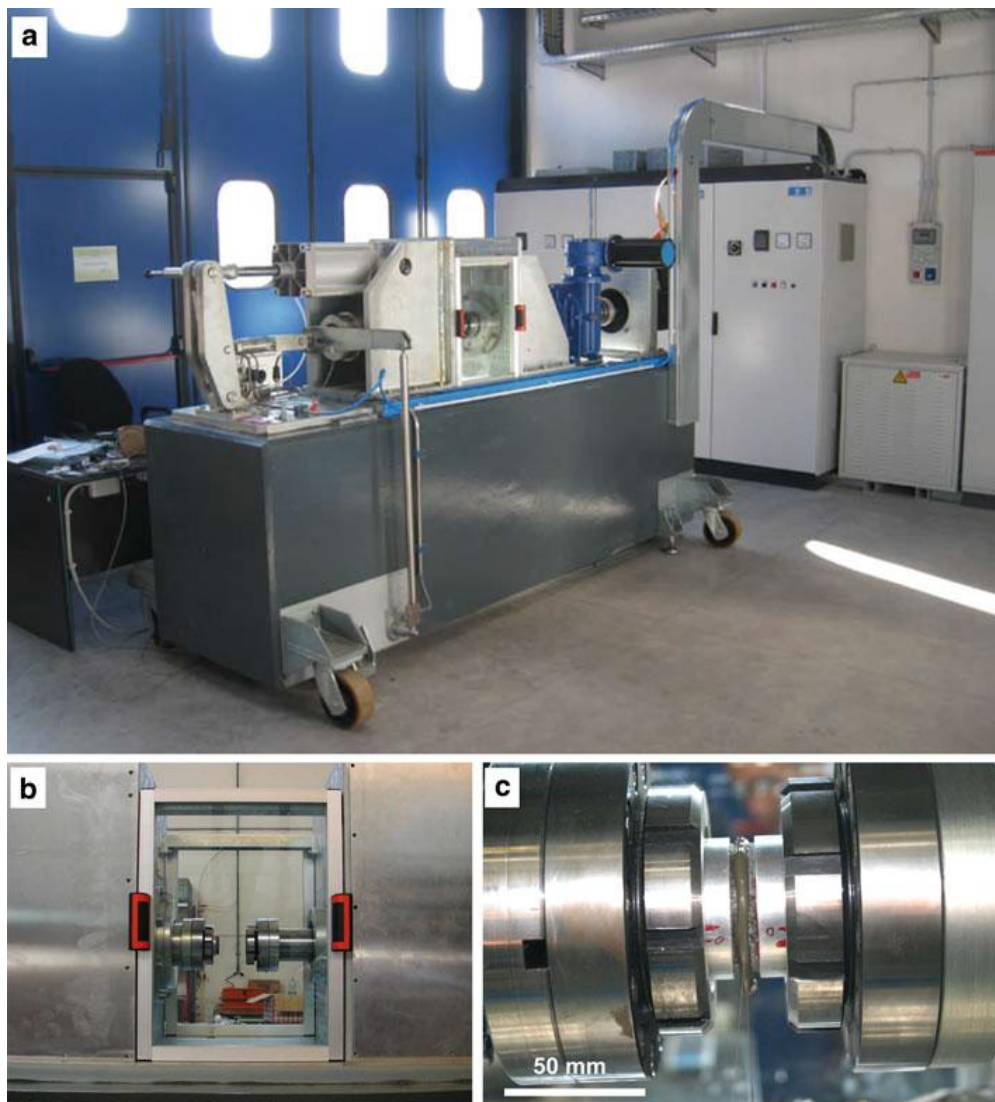


Figure 4 a) Photo of SHIVA at INGV laboratory. b) and c) Details of sample chamber.

SHIVA has a horizontal setup, with a length of about 4 m, a width of about 0,9 m and weight of 4000 kg. Samples are put in sample chamber at the end of two columns (one of these is stationary) (Fig.6 b) and c) and axial load is applied via an air-actuated pneumatic piston. In figure 7 is reported a detailed image of all SHIVA's component. SHIVA shown that this machine can impose a wide range of slip velocities (10 $\mu\text{m/s}$ to 6,5 m/s for hollow-shaped samples) and of accelerations (from 0 to 6.5 ms^{-2} in 0.1 s or 65 ms^{-2} under a normal stress of 50 MPa), allowing the investigation of entire earthquake cycle (nucleation, seismic slip and post-seismic deformation). Samples for SHIVA can be made as solid cylinder or hollow-shaped cylinder with an external diameter of 50 mm and internal diameter of 30 mm.



A new state-of-the-art tool to investigate rock friction under extreme slip velocities and accelerations: SHIVA

Andr Nemesj, Giulio Di Toro^{1,2}, Stefan Nielsen¹, Steven Smith¹, Ashley Griffith¹, Piergiorgio Scarfaro¹, Gianni Romeo¹, Giuseppe di Stefano¹, Fabio di Felice¹ and Sofia Mariano¹
¹ Istituto Nazionale di Geofisica e Vulcanologia, Via di Vigna Murata 605, 00143 Rome, Italy
² Dipartimento di Geoscienze, Universit di Padova, Italy

Poster T23-1950
 Tuesday 15-12-2009 13:40

Introduction

Despite considerable effort over the past several decades, the mechanics of earthquakes rupture remain largely unknown. In order to complement fault drilling projects and field and seismological observations, recent friction experiments strive to reproduce as closely as possible in-situ (natural) conditions of slip velocity and acceleration on intact and fault rocks. In this contribution, we present a novel state-of-the-art experimental rotary shear apparatus (SHIVA or Slow to High Velocity Apparatus) capable of shearing ring-shaped samples (40/50 mm in/extern. diameter) at sliding velocities up to 9 m/s, accelerations of ~ 40 m/s^2 and normal stresses up to 50 MPa. In comparison with existing high speed friction machines, this apparatus extends the range of sliding velocities, normal stresses, sample size and, more importantly, accelerations. We aim to perform experiments on rock samples of a variety of compositions using slip velocities and accelerations that simulate slip velocity functions that occur during earthquakes. In addition, we plan to develop a pore fluid system and a pressure vessel in order to perform experiments that include the physical-chemical processes that occur during slow interseismic periods. Moreover, experiments will be run where we control the shear stress rather than the slip rate. By doing so, we will be able to simulate the transient load variation expected during seismic failure on natural faults and measure the related dynamic weakening, frictional evolution and slip velocity on the sample. The characterization of rock frictional behavior under combined conditions of low to high slip velocity and extreme and rapidly variable load, is expected to provide important insights into the mechanics of earthquakes.

Engines & coupling

A Low backlash flexible below couplings to allow torque transmission. Torque limit is 1500 Nm.
 B Large brushless (i.e. frictionless) engine with nominal power of 44 kW and peak power up to 270 kW.
 Rotation speed up to 3820 RPM or 9 m/s on a 40/50 sample
 C Small engine with nominal power of 5.15 kW. Rotation speed up to 5790 RPM and minimum sliding velocity of 1 $\mu\text{m/s}$
 D Gearbox with a ratio 1.225 which results in a reduction of speed of the small engine so that the maximum velocity on a 40/50 samples is 6 mm/s.
 E Sprag clutch to allow a transition between the large and small engine without the loss of motion and torque. For more detail, see below.

Inverter/controller

- Controls current and frequency of output to the engines.
 - Displacement of internal angular encoders of the engines.

Torque measurement

A: Arm halts rotary movement
 B: Sealed "S" beam type loadcell (full-scale 3 kN and resolution of 0.9 N) measures shear stress up to ~100 MPa and 0.03 MPa resolution for 40/50 samples

Rotary displacement

RESM encoder with SINGUM reader head
 Scale marks each 20 μm
 Resolution = 0.2 μm

Air-actuated loading system

A: Air-actuated hydraulic piston supplies a maximum pressure of 6 bar or 18 kN
 B: Arm increases thrust to 50 kN or 70 MPa of normal stress on 40/50 samples
 C: Loadcell (full scale 50 kN, resolution 2.5 N) measures normal load up to 70 MPa with 0.035 MPa resolution on 40/50 samples
 D (not visible): LVDT (full scale 50.8 mm, resolution 50 μm) measures shortening. In future, a LVDT with 1 μm resolution will be placed next to the sample.
 E: Air actuator to control pressure on the piston.

Low-to-high velocity transition sprag clutch

Anti roll over (ARO) hardened Sprags
 Springs ensure the Sprags are at full contact at any moment in time, eliminating all motion loss.
 Sprags in normal engagement position. Both the inner and outer race rotate.

Real-time data acquisition

Compact-Rio (National Instruments) programmable automation controller allows for real-time data acquisition and control

Sample holders

Design for sample holder for gouges and fluids
 spacious chamber allows for incorporation of several devices such as a pressure vessel, vacuum chamber and a furnace.
 Apparatus sized for 40/50 mm ring-shaped samples

First tests

"Standard" velocity-sleeping tests with "instantaneous" acceleration to explore RSF parameters, in particular the characteristic slip distance.
 Tests with a slip velocity function as input (to mimic actual slip velocity during an earthquake)

First test: using solid 50 mm cylinder of gabbroic rock at ~8 MPa and ~5 m/s demonstrates the power capacity of the apparatus.

CONCRETE BASE (3700 KG)
 3.5 meters

PERFORMANCE

for 40/50 mm in/extern. samples

Parameter	MAX	MIN	RES.
σ_n (MPa)	70	0.5 ?	0.035
v (mm/s)	9000	0.001	---
a (m/s^2)	40	??	--
d_s (μm)	=	0	0.2

Acknowledgments
 This work is funded by the European Research Council Starting Grant no. 320716 (SHIVA project). The authors gratefully acknowledge the support of the computer and facility manager of the machine workshop (DIP) Rome who constructed the apparatus.

Figure 5 Poster with explained all SHIVA's components.

In the experiments described in this thesis we used hollow cylinders. To obtain them, we first drilled a tonalite rock slab about 45 mm thick with a diamond drill bit of 50 mm internal diameter. In this way we produced the rock cylinders. Then, to produce the hollow-shaped cylinders we made an internal hole of 30 mm in diameter and about 4 mm deep with a lathe (with diamond tools). Subsequently, the

rock cylinder was inserted into an aluminum ring of approx 40 mm in height and 50 mm in internal diameter. The rock cylinder was then glued to the external aluminum ring with an epoxy resin (Araldite 20 20). After 48 hours, when epoxy was hardened, the part of rock coming out from jacket was worked with lathe to obtain a smooth surface. After this refining and polishing, the rock coming out from ring is 1-2 mm in height and the walls of the tonalite samples were sustained by the external aluminum ring.

2.3 Determination of microroughness

To determine microroughness in natural and experimental faults we followed this procedure: (1) we drawn the pseudotachylite wall-rock boundary with the software ArcGIS 10; (2) converted the file format into spatial-referenced AutoCAD files; (3) imported the files in MatLab and (4) calculated roughness from ω_0 (characteristic asperities height) and λ_{ave} (the average wavelength) with a MatLab script created and give to us by courtesy of A.W. Griffith (see Appendix A).

2.3.1 ArcGIS

ArcGIS is a Geographic Information System (GIS) that integrates hardware, software and data for capturing, analyzing and managing all forms of geographically-referenced information. Furthermore, GIS allows an easy handling of images and data. We used GIS to create the pseudotachylite-wall rock boundaries from natural and experimental thin sections images (fig. 8). The polyline shapefile created with ArcGIS is a geospatial data format for storing geometric location and for attributing information about the shapes represented.

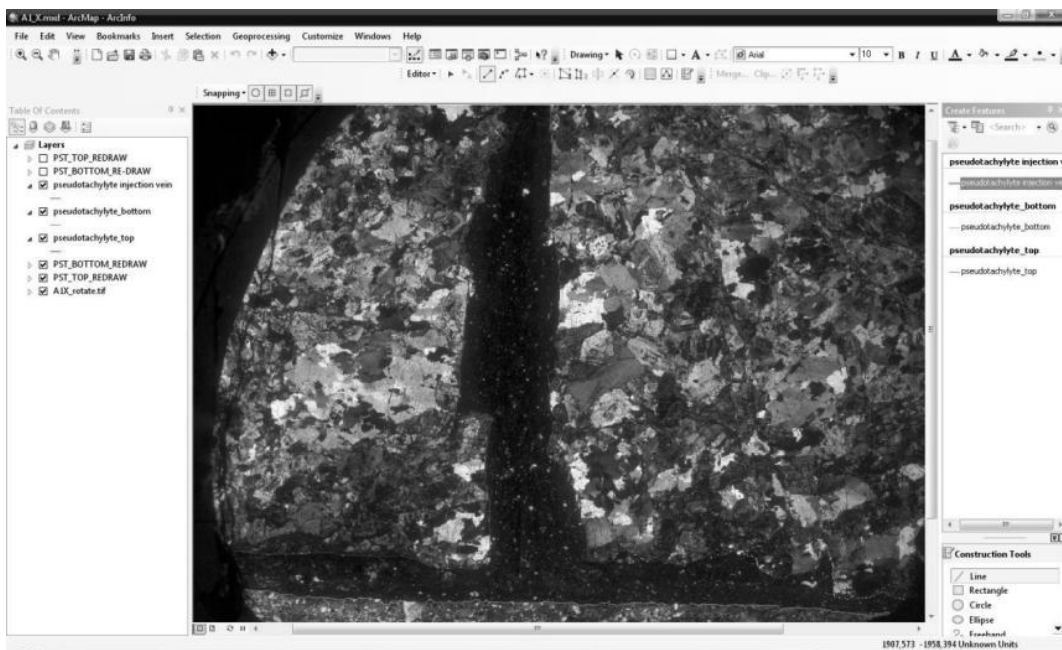


Figure 6 Example of ArcGIS environment utilized to draw pseudotachylite profile.

Polyline shapefile created are subsequently exported in Autocad file and converted with Dxf2xyz 2.0 (open source program) in a .xyz files.

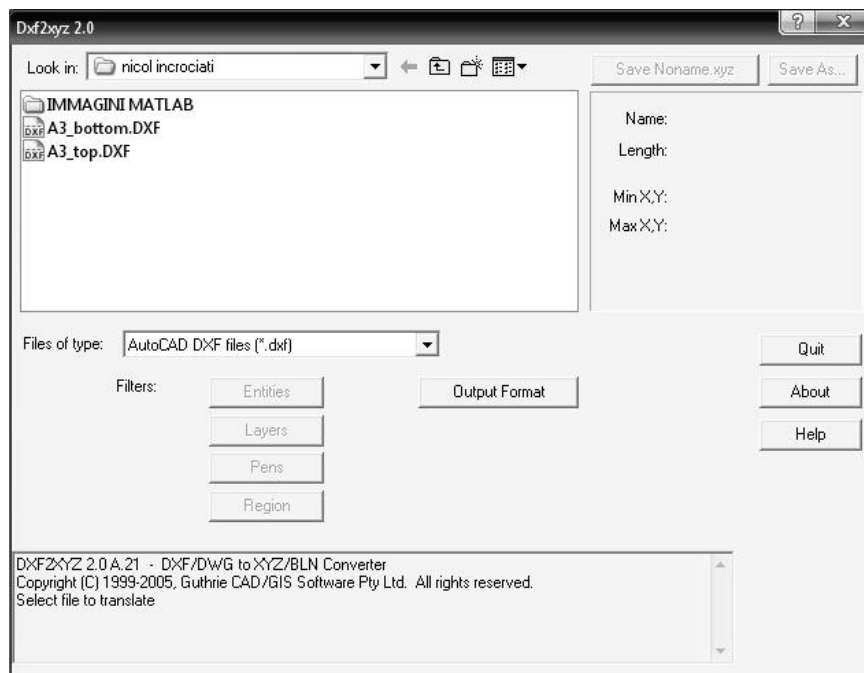


Figure 7 Dxf2xyz 2.0 program to convert autocad file in spatial-referenced file (.xyz).

2.3.2 MatLab script

MatLab is a program created for numerical computation, visualization and programming. With MatLab is possible to analyze data, develop algorithms and create models. In this thesis, MatLab is used to calculate the microroughness of pseudotachylyte-wall rock boundaries in natural and experimental faults. For a description of the MatLab script used here, see **appendix A**. Ideally, each point of the profile should have a single x-coordinate and a single y-coordinate. However, because of the presence of injection veins and other “embayments” along the profile (see Fig. 10) locally to one value of x might corresponds two or more y values. To solve this issue, which might result in paradoxical results in the determination of the micro-roughness, some profiles were locally smoothed and the embayments eliminated, as shown in Fig. 10 a) and b).

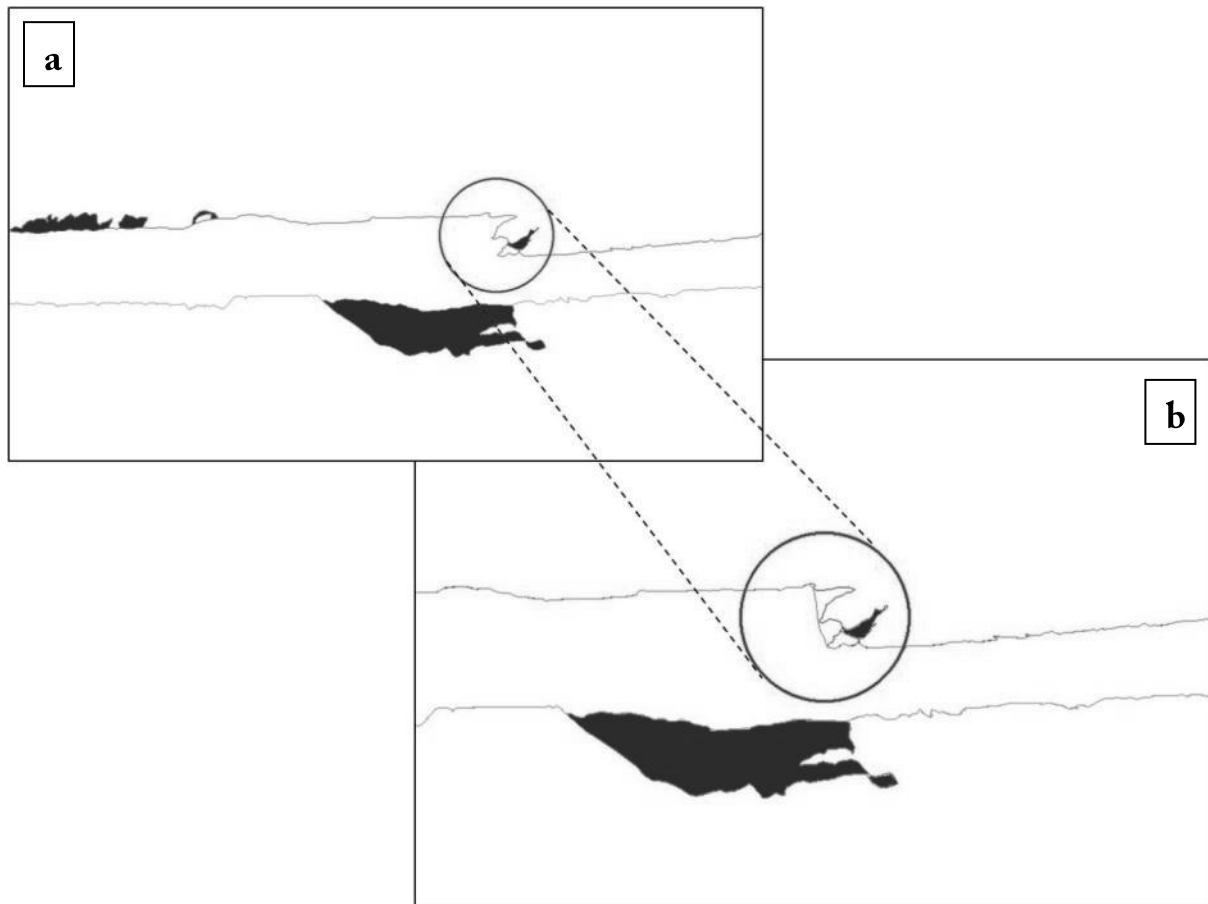


Figure 8 Simplified example of sketch that illustrate original drawn profile (a) and re-drawn profile (b). Biotite in brown color.

As result, by running the script we obtain 5 figures for each individual profile and the measurement of the characteristic asperities height, ω_0 , and of the characteristic average radius, λ_{ave} , (see appendix A for details). For each top and bottom profile, three values of ω_0 and λ_{ave} are calculated with a moving average of 3, 4 and 5, respectively. An average and standard deviation value is reported as single value for each top and bottom profile.

Chapter 3 Microroughness in natural faults (Gole Larghe Fault Zone)

3.1 Regional setting

The Adamello batholith consists of tonalitic to granodioritic rock exposed over 670 km² in the Italian Southern Alps (Callegari&Brack, 2002), delimited to the north by Tonale Line and to the east by the Giudicarie Line.

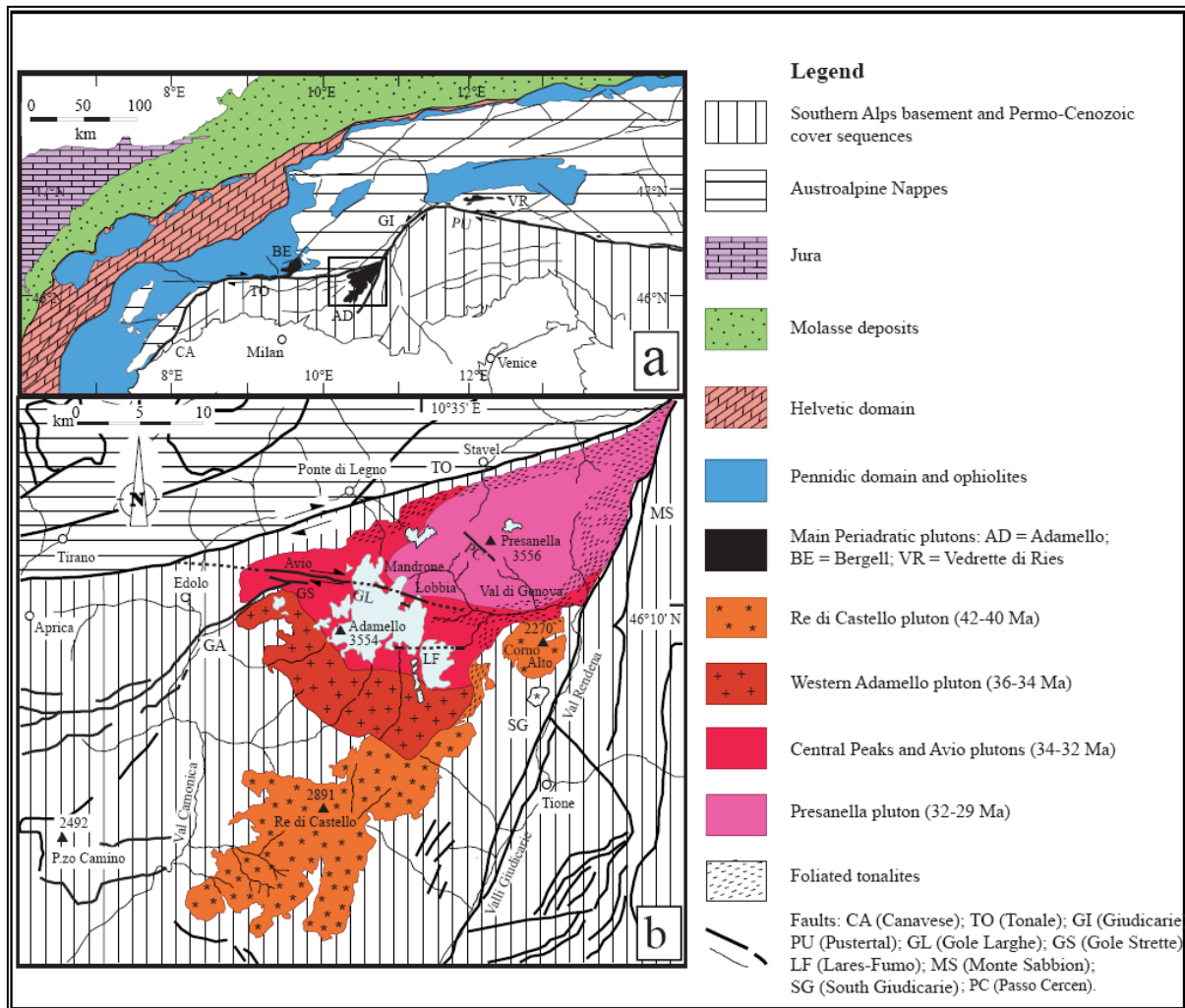


Figure 9 a) Simplified map of the Alps with represented the Periadriatic Lineament as solid line and b) Adamello batholith map with indicated the Gole Larghe Fault Zone (GL).

3.1.1 The Adamello batholith

The first geological map (1:75.000) of the Adamello massif was edited by W. Salomon in his extraordinary work “Die Adamellogruppe” (1908-1910). After this, many scientist, in particularly from Padova University and ETH in Zurich, worked in this area to unravel the different geologic structures and petrologic/petrographic units and relationships. In particularly, Callegari and Brack summarized more

than fifty years of studies in the “Geological map of the Tertiary Adamello batholiths (Northern Italy). Explanatory notes and legend.” (2002).

The Adamello pluton, after re-called by Callegari (1985) batholith because composed by several individual plutons, is the largest (670 km²) and oldest (42-31 Ma) Tertiary intrusion along Periadriatic Lineament (PL). The PL is a fault system of about 700 km in length from Piedmont (NW Italy) to the Austrian-Slovenian border, and it separates the two main domains of the Alps: the north-verging metamorphic pile of Penninic-Austroalpine nappes and the south-verging thrusts and folds of Southern Alps. The Adamello batholith is the only one among the Periadriatic plutons intruded within the Southern Alps.

The composite nature of the batholith was recognized and documented for the first time by Trener (1912), who described six different magmatic bodies with different ages, basing on their intrusive intersection relationship. Trener’s work was re-interpreted thanks to the contributions of Bianchi & Dal Piaz (1948a), Bianchi *et alii* (1970) and finally with Rb-Sr dating on tonalitic rocks of each body conducted by Del Moro (1985 a,b).

The Adamello batholith is now divided into four superunits, distinguished in age and petrographical/mineralogical composition:

1. Re di Castello-Corno Alto superunit: 42-36 Ma; is the oldest of the intrusive bodies. Medium-fine grained biotite-hornblende tonalite to granodiorite.
2. Adamello: Coarse grained biotite-hornblende tonalitic to leucotonalite;
3. Avio-Central Peaks: Medium grained biotite tonalite;
4. Presanella: 32-29 Ma; biotite-hornblende tonalite

The mechanism of emplacement of the batholith was debated for long time. In the southern units stopping and ballooning are the mechanisms invoked to explain pluton intrusion (Brack, 1983, John&Blundy, 1993). In northern part, several data on metamorphic contact aureole and mylonite zone are collected to explain the emplacement (Werling, 1992, Stipp 2002, 2004). Combining these data with the previous data collected by Rinklin (1983, for the southern part), a pressure of emplacement can be estimated as > 0,2 GPa in the southern contact aureole and 0,35 GPa for the contact aureole (John Blundy, 1993) from the coexistence of quartz + andalusite + sillimanite + muscovite + K-feldspar (+ H₂O). Results highlight nearly identical emplacement conditions for the whole batholith. The bulk of the Adamello batholith, if compared with the deformation accommodated by the south verging thrust of the Val Trompia, it is referred as “un-deformed” in the literature, with the exception of the foliated tonalite kilometer belt along the NE border and along the contact between the Presanella and Avio Pluton. Along the Tonale fault, country rocks are foliated because subjected to a dextral strike-slip and to the contact metamorphism induced by Presanella intrusion. These evidences indicate that the Tonale

line was active during cooling of Presanella intrusion (30 to 32 Ma, Werling, 1992; Stipp et al 2002, 2004). The intrusion depth, considering an emplacement pressure between 0,2-0,35 GPa, and a rock density of 2650 Kg/m^3 can be inferred in the range of 9 to 13 km. However, several brittle faults cut the Adamello Massif: within these, the Gole Larghe Fault Zone.

3.1.2 The Gole Larghe Fault Zone

The studied outcrop is located at the base of Lobbia glacier in the upper Val di Genova (Fig. 12).

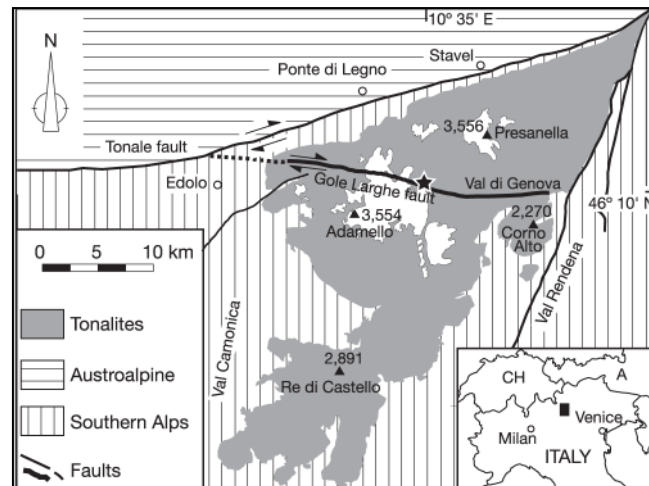


Figure 10 Sketch of Adamello batholith with indicated the interested outcrop along the Gole Larghe Fault Zone (star)

The Gole Larghe Fault Zone (GLFZ) extends from north of Edolo to the west, where the fault zone probably merges into the Tonale fault, to the Giudicarie Line to the east, cutting the entire Adamello batholith with E-W strike. Near Edolo, the intersection is close to the major bend of the Tonale fault from E–W to ENE–WSW.

The studied outcrop has been recently exposed (last 30 years) and the polished by the retreat of glacier, so that all the geological structures (joints, ductile shear zones, brittle faults, xenoliths, dikes, schlierens, etc.) are perfectly visible. The outcrop is within the Avio pluton, characterized by a medium-to-fine-grained (mm in size) tonalite composed by plagioclase (45-50%), quartz (25-30%), biotite (15-20%) and K-feldspar (1-5%). The pluton was interested by a late- to post- magmatic deformations. From the oldest to youngest we recognize:

- 1- Cooling joints (probably from 750° to 550° C ambient temperature)
- 2- Solide-state ductile shear zone (about 500° C)
- 3- Faults with indurated cataclasite and pseudotachylyte (about 250° C)
- 4- Zeolite-bearing veins and faults ($< 200^\circ$ C)

Field observations highlight how the shear zones (ductile and brittle) exploited pre-existing cooling joints, inheriting their orientation. Joints form a pervasive network within the pluton and are organized in different systems. Furthermore joints are segmented (from less than a meter to several tens of meters) along strike and this characteristic determines the partitioning of slip during both ductile and brittle reactivations (Pennacchioni et al, 2006).

The Gole Larghe fault zone shows an array of about 200 major sub-parallel faults, spaced 2–6m apart, and fault rocks include green indurated cataclasites (produced by brittle deformation without melting) overprinted by pseudotachylytes (that confirm the occurrence of ancient seismicity). Slickenlines on the fault surfaces and separated structural markers indicate a dextral transpressive strike-slip. The cumulative slip estimated from marker separations along some transects perpendicular to the GLFZ strike is about 1.1 Km over a bulk thickness of the fault zone of about 550 m (Di Toro and Pennacchioni, 2005).

In this fault zone, pseudotachylyte production occurred at 250-300 °C and at depth of 9-11 km. Analysis on these PST reveal relatively dry conditions (probably sub-hydrostatic fluid pressures) because the presence of fluids is usually at odds with production of frictional melts. Assuming low fluid pressure and a stress tensor in agreement with strike slip faulting, this results an effective normal stress on the fault at depth of 10 km between 110 MPa for hydrostatic pore pressure, and 182 MPa with no pore pressure (Di Toro et al., 2005).

3.2 Microroughness in natural pseudotachylytes

Typically, pseudotachylytes occur as fault veins and injection veins. When seismic rupture propagates, the stress field perturbation around a fault tip induces fracturing in the wall rock, followed by surface refinement through grinding and melting of initial gouge (Fig. 13) (i.e. Rice, 2006). Highly comminuted gouge melts when strain rate is higher. Melt produced in the slipping zone is mostly injected in pre-rupture fracture or in new fracture produced (i.e. injection vein) during propagation. But a small part of these remain in slipping zone (fault vein) creating a lubricated condition where the slip rate drops down. Melt presents in slipping zone cooling rapidly increasing the viscous strength and leading to the healing of rupture. All the process described occur in 1-10 seconds (Heaton, 1990), times typical of earthquakes. In the injection veins, melt cooling more slowly, from seconds to minutes, in function of melt peak temperature, temperature of host rock and the thickness of melt layer (Di Toro et al 2010).

In the GLFZ, injection veins are accurately studied by Di Toro et al, (2005) to investigate the relationship between the stress field pattern at the tip fault and the propagating rupture. Given a fixed rupture direction with different rupture velocities, in each models a tension region located in the southern block respect fault vein is obtained. In a case of rupture approaching the Rayleigh wave

velocity, the stress perturbation is maximized and results in an orientation of cracks (mode I or tensile) perpendicular to the fault plane (Fig. 14). This is consistent with the observations along the GLFZ (Fig.15).

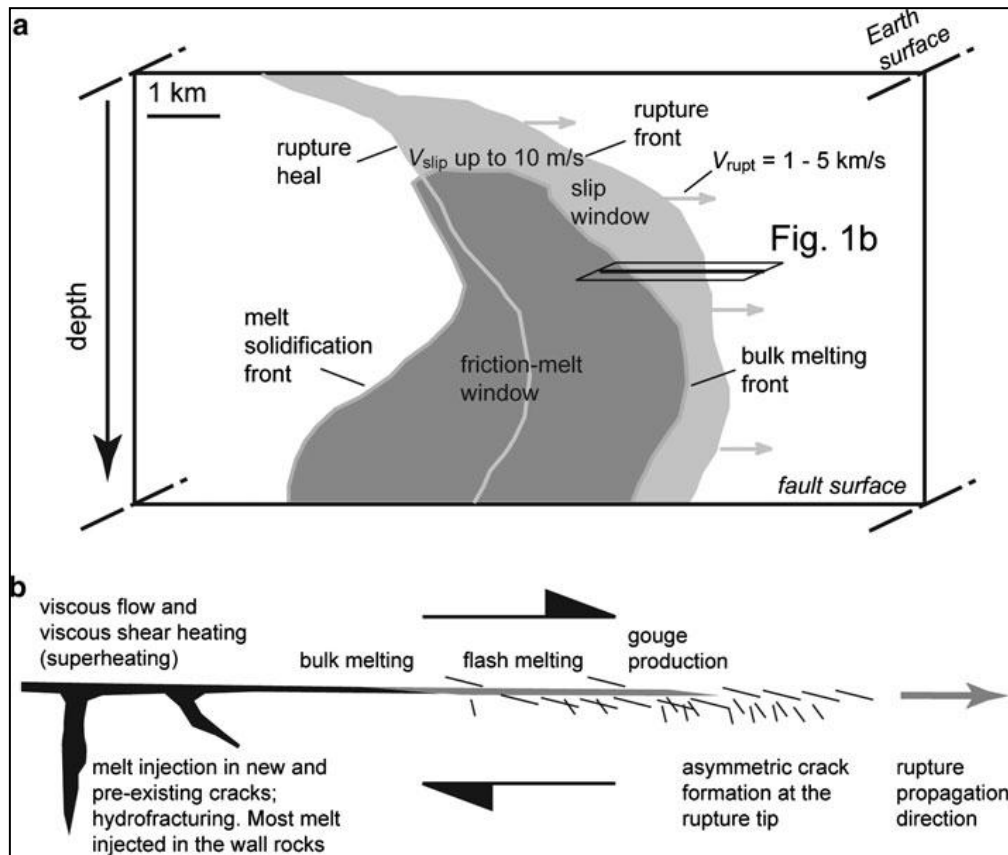


Figure 11 Production of pseudotachylite (modified from Swanson 1992) a) The fracture propagated toward the right side with a mode II crack. Fracture velocity is in a range of $1-5 \text{ km s}^{-1}$; behind this, the light grey area represents a slipping area overlapped by a dark grey area representing friction melt window. In this area, melt can survive for some time after slip stop. b) Enlargement of fig. a. Propagation of rupture front produces fractures in the lower block (see text). After gouge production and comminution, flash melting and bulk melting occur. Most melt is injected in new and pre-existing cracks.

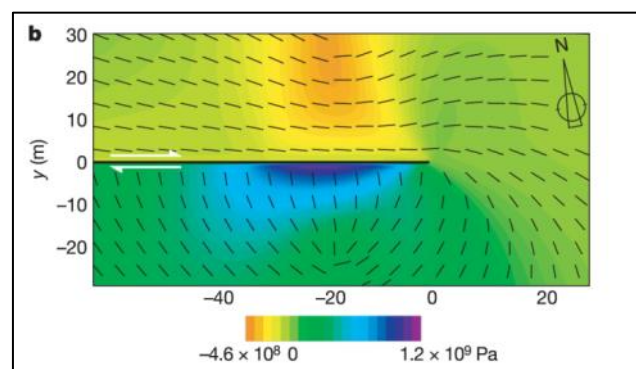


Figure 12 Tensile stress around fault tip modeled with constitutive parameters based on the Gole Larghe Fault Zone. Rupture velocity of $v=0,9 v_s$. Fracture propagation is from left to right (dextral strike-slip fault). Color orange-yellow represents negative (compression) stress, while blue represents positive (tension) stress. The black segments are local direction of maximum

tension: in this model, with this parameters, the maximum stress is oriented perpendicular to the fault plane in the southern block. This is consistent with the situation in GLFZ.

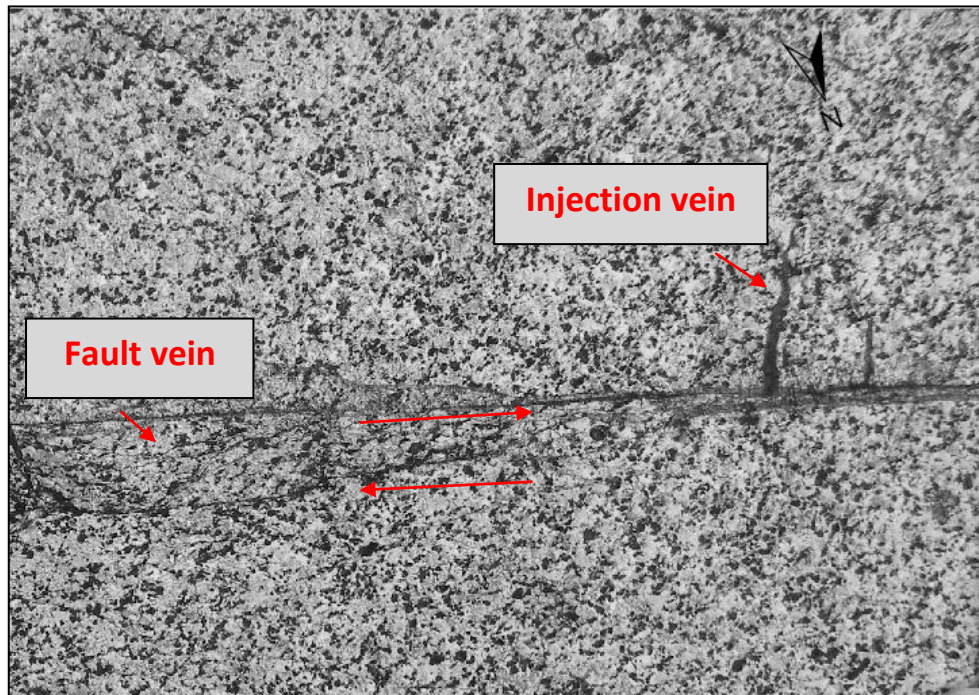


Figure 13 Real example of fault vein and injection veins in the GLFZ.

The roughness of natural fault surfaces is fractal (self-affine) both parallel and perpendicular to slip. The measured wavelength ranges from microns to tens of Km (e.g., Power et al., 1987; Lee and Bruhn, 1996; Sagy et al., 2007; Candela et al., 2009). Roughness causes local variations in field stress and displacement, and waviness or kinking of the fault surface can be a barrier to rupture growth and propagation (e.g., Nielsen and Knopoff, 1998; Kame et al., 2003; Bhat et al., 2004). So, the fault surface roughness exerts a fundamental control on the parameters affecting fault friction. For instance, [Griffith et al \(2010\)](#) investigated the role of fault surface roughness in controlling melt distribution and lubrication in exhumed strands of the GLFZ. From this analysis, it results that fault waviness causes heterogeneous melting along fault strike, in particular in contractional bends, where melting was enhanced by the higher stress normal to the fault. Because of fault waviness, contractional bends are accompanied by opening along extensional bends where frictional strength drops to zero and pseudotachylyte is accumulated.

Since the frictional power dissipated during seismic faulting is proportional to slip rate and to the stress normal to the fault (which is high in compressional jogs and low or negligible in extensional jogs), we selected four wavy faults. The idea was to seek for microstructural evidences (= different microroughness) to confirm the theoretical model proposed by Nielsen et al., 2010 and to estimate the frictional power dissipated during seismic slip. In particular, to reduce the role of different grain size and mineral composition in controlling fault surface microroughness, we selected only pseudotachylyte-

bearing faults (i.e. without indurated green cataclasites). We also selected injection veins because, since they are tensile cracks and not subjected to shear and frictional heating, they could be used as a microroughness reference in a host rock at a temperature of about 250° C before melt injection.

Selected fault	Sample	Domain
Fault 1_GPS	A1	Injection vein
	A2	Injection vein
Fault 2_GPS	A_02_02	neutral
	A_02_04	compres
Fault 3_GPS	A4	neutral
Fault 4_GPS	A5	extens
	A7	compres

Table 1 The selected fault and samples collected from different domain along faults.

3.2.1 The selected faults

In the GLFZ, the main faults strike mainly E-W with an average dip of 50-70° (Fig. 16). Samples were stem from these faults outcropping in glacially-polished outcrops dipping about 10-20° to the North. To obtain fault cores parallel to the dip of the fault and for safety reasons, the operator was drilling (and produced the photo-mosaics) by looking to the South. As a consequence, in the following description North is to the bottom.

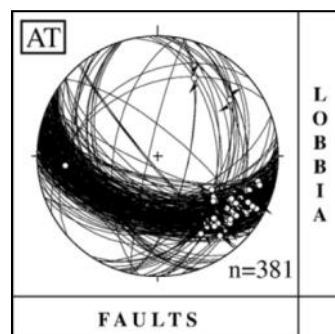


Figure 14 Stereoplot of structural data of Lobbia outcrop. Prevalent E-W strike is highlight. Open circles are poles of lineations and arrows are the sense of shear (Pennacchioni et al, 2006)

The selected faults were drilled about perpendicular to the outcrop surface. Slickenlines on fault surfaces decorated by cataclasites and pseudotachylytes (fault veins) dip shallowly to the east of about 34°. Given the well-polished outcrop surface, in the selected drilled faults, the fault surface was not exposed (i.e., it is well exposed the intersection of the fault surfaces with the outcrop surface) and we

considered the average slip direction (34° East). Thin sections for microroughness analyses were cut perpendicular to the fault surface and parallel to the average slip direction as shown in figure 17.

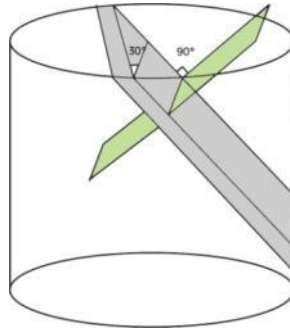
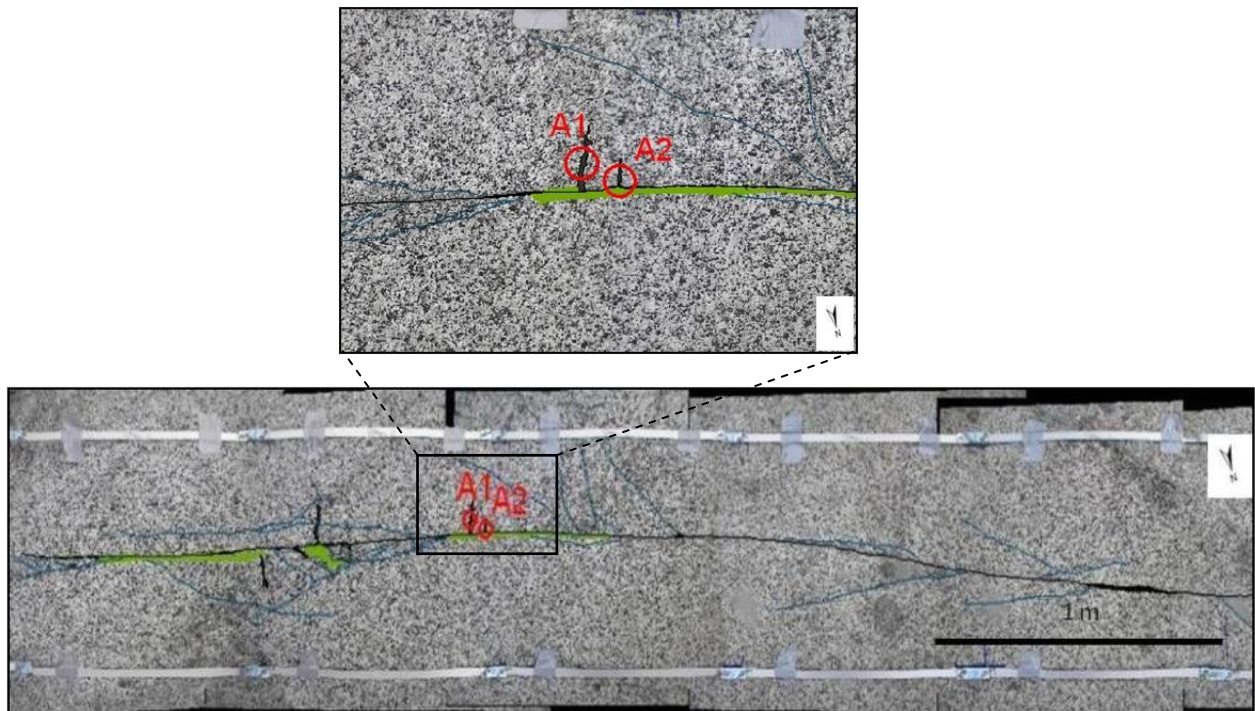


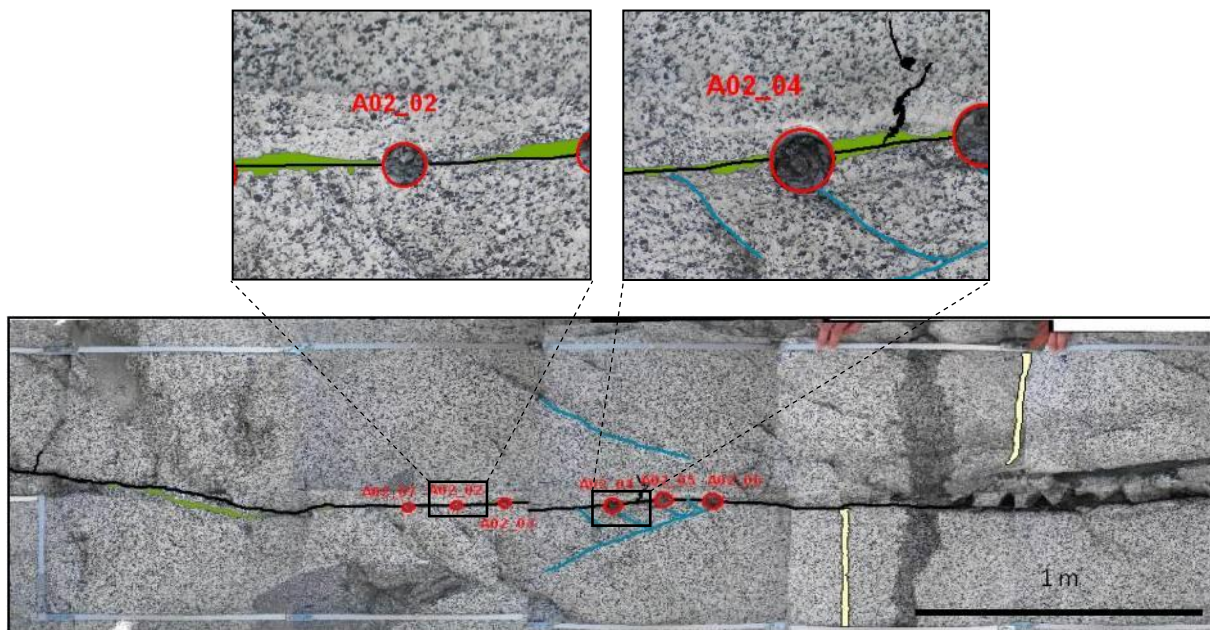
Figure 15 Simple sketch to show how thin sections (green in color) were cut perpendicular to the fault surfaces (gray in color) and parallel to the slip direction.

Fault 1: GPS AL04 (32T, 0621877 East, 5114408 North UTM)



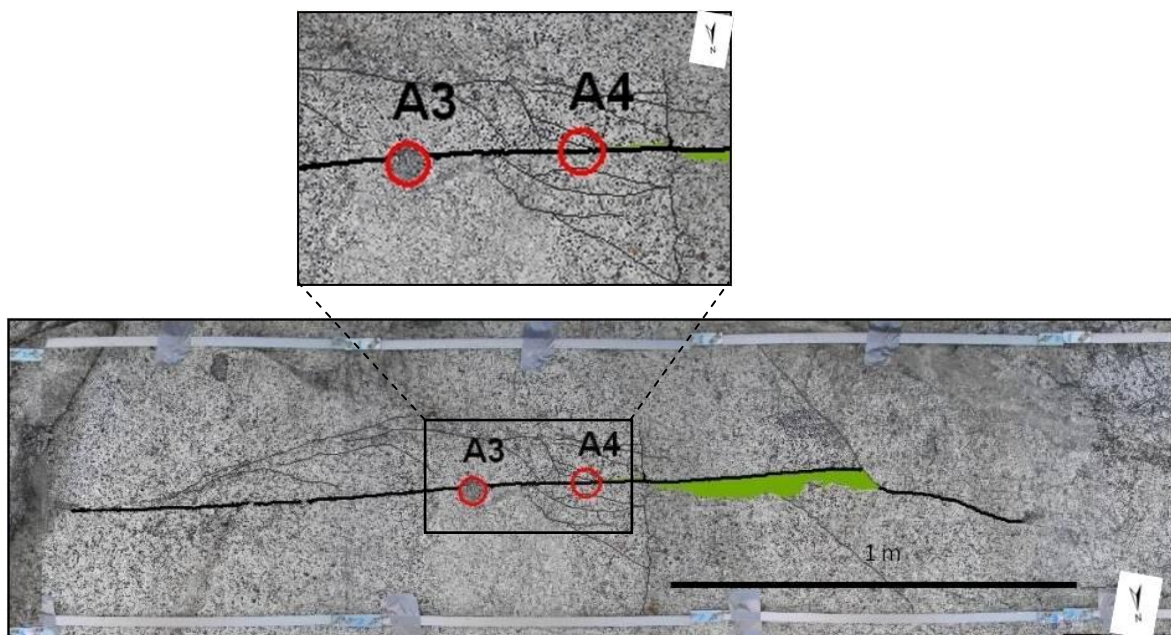
From this fault we sampled two injection veins. They were both injected towards the south-wall rock. Along the fault are present green in color indurated cataclases. Pseudotachylyte is present almost along the entire fault, as it is possible to see in the photomosaic. North is pointing downward.

Fault 2 GPS AL02 (32T, 0622074 East, 5114381 UTM)



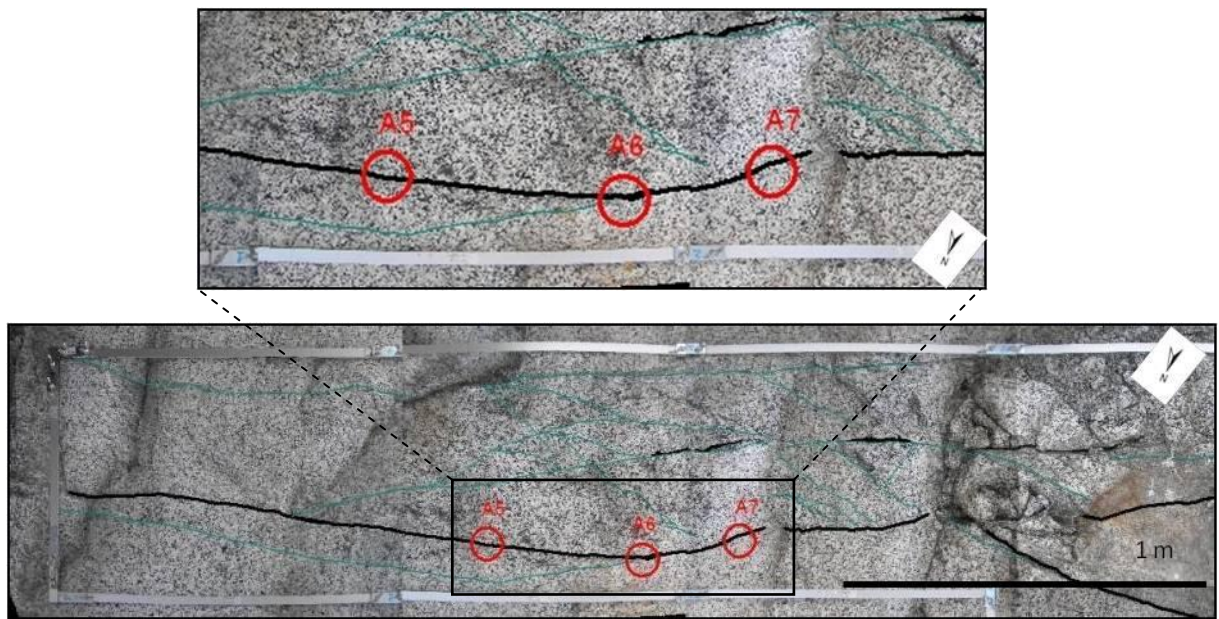
This fault (i.e., the intersection of the fault surfaces with the outcrop surface) presents a clear wavy behavior. Among the six samples collected, we choose only two samples to represent the “neutral” (A02_02) and the compressional (A02_04) domains (the fault is dextral: see the aplite dike separated of 0.28 m by the fault). North is pointing downward.

Fault 3 : GPS AL03 (32T, 0622058 East, 5114381 North UTM)



From this fault we analyzed only sample A4, representing a “neutral” domain. North is pointing downward.

Fault 4 : GPS AL05 (32T, 0622064 East, 5114385 North UTM)



Between the selected faults, this fault shows a strong curvature and wavy trend. Three samples were collected from the three different domains, but only A5 (extensional) and A7 (compressional) are analyzed here. Along fault there is no evidence of the presence of green indurated cataclasites. North is pointing downward.

3.2.2 Microroughness in pseudotachylyte injection and fault veins

A1 and A2: injection vein.

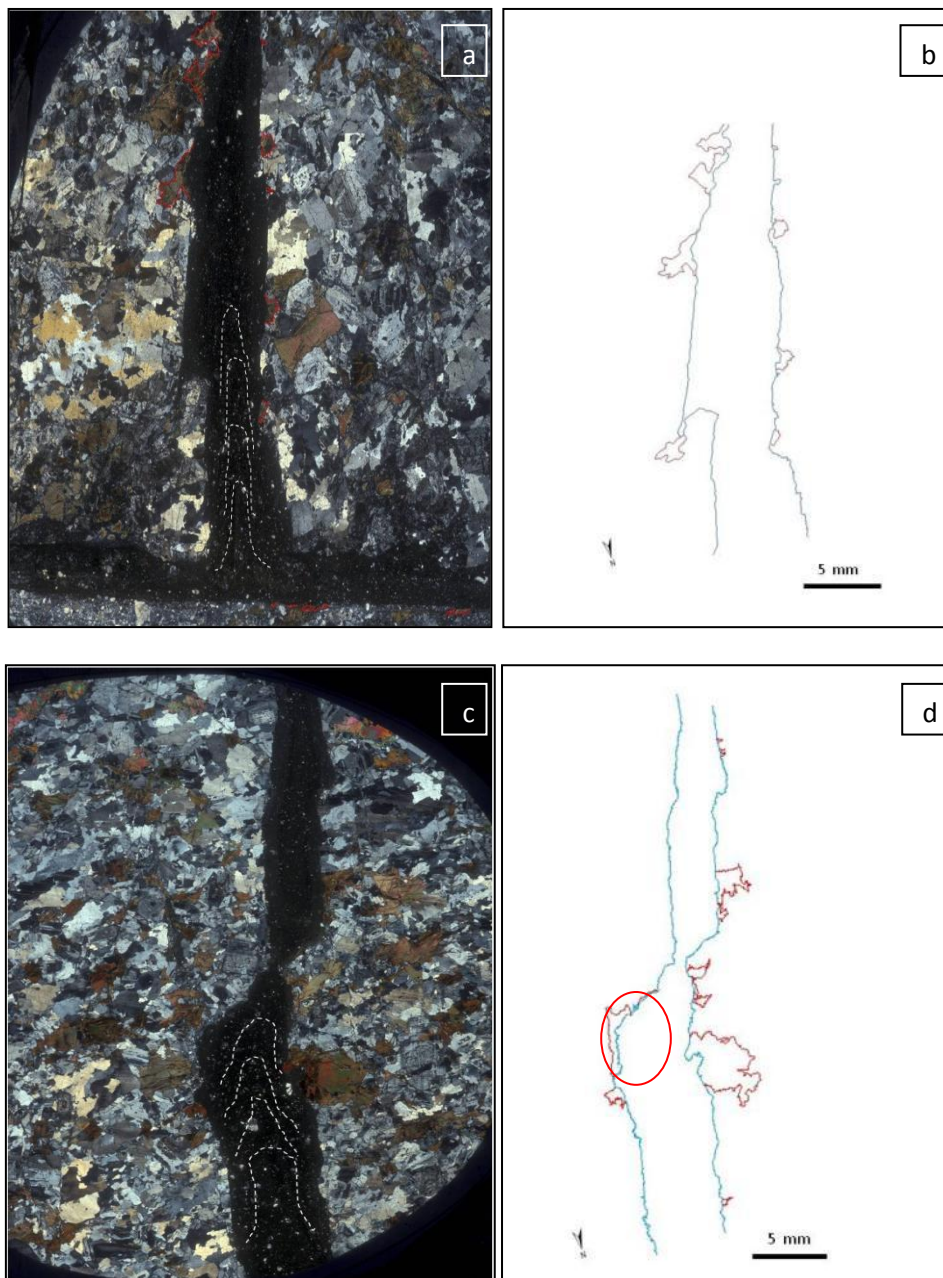


Figure 16 Photo of A1 (a-b) and A2 (c-d) sample (Fault 1) in thin section at crossed nicols. Injection vein: no slip, mode I or tensile fracture. Biotite is in red.

Sample A1: The lower boundary (i.e., the northern one) of the fault vein with the host tonalite is more cataclastic are less straight than the upper one. In the upper (towards the north) boundary, embayments are found where biotite is present in the wall rock. The injection vein in this thin section is 6-7 mm and 22 mm long. Along the injection vein, the pseudotachylyte-tonalite boundary is sharp when

quartz and plagioclase are present in the wall rock, and is less straight in the presence of biotite. Pseudotachylyte contains rounded lithic clasts of host rock (mainly quartz and plagioclase) embedded in a glassy-like matrix. The presence of flow structures (Fig 18a, white dashed lines) at the base of the injection vein evidences the mechanism of melt injection into the rock wall. We measured the micro-roughness of the two injection vein boundaries (fig 19) with MatLab (see Methods section 2.3.2). The resulting average and standard deviation values for ω_0 and λ_{ave} , are reported in the table 2. For injection vein, since these are cracks, the slip rate along the walls is 0 m/s and we attributed 0 MW/m² to the frictional power dissipated along these boundaries.

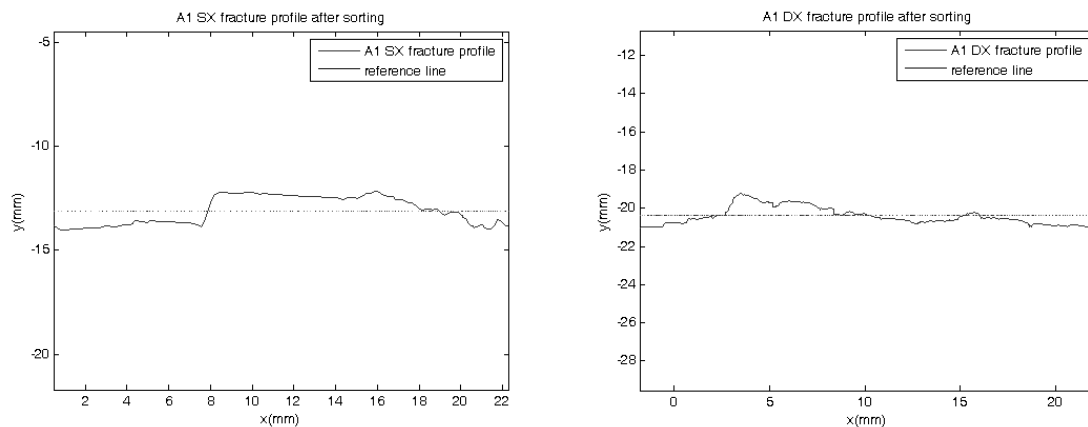


Figure 17 Profiles of sample A1 obtained with MatLab script. Left: east profile of injection vein A1. Right: west profile.

Sample A2: In this injection vein, as was the case of sample A1, the embayments along the pseudotachylyte-tonalite boundary are found in the presence of biotite in the wall rock, whereas the boundary is straight in the presence of quartz and plagioclase grains; “flow structures” are found (Fig. 18c). There is evidence of deformation by sub-grain rotation recrystallization of quartz in the wall rock (red circle, but not visible in this image). At the constriction of vein in proximity of the connection between two en-echelon segments (versus North, dextral step-over) the quartz grains are worn and determine a rough pseudotachylyte-tonalite boundary. This peculiar boundary geometry is found only here. Injection vein is 6-7 mm thick and 33 mm long (in the thin section). As was the case for sample A1, we attributed 0 MW/m² to the frictional power dissipated along these boundaries.

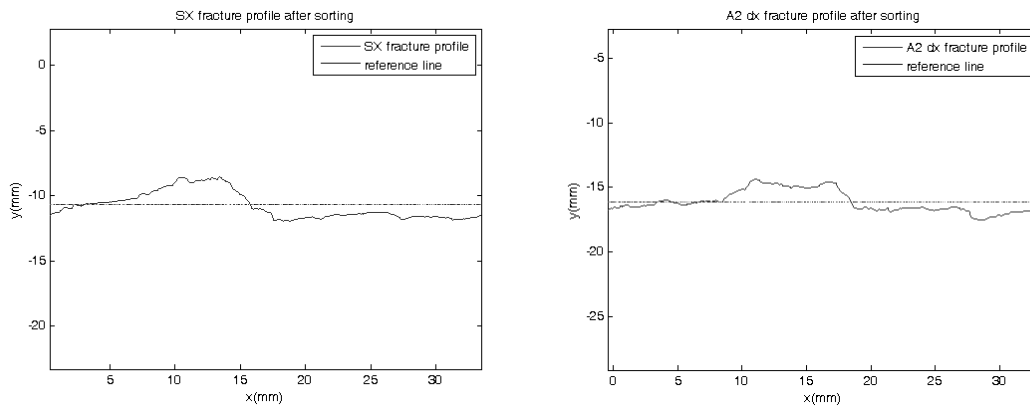


Figure 18 Profiles of sample A2 obtained with MatLab script. Left: east profile of injection vein A1. Right: west profile.

A02_02 and A4: neutral domain

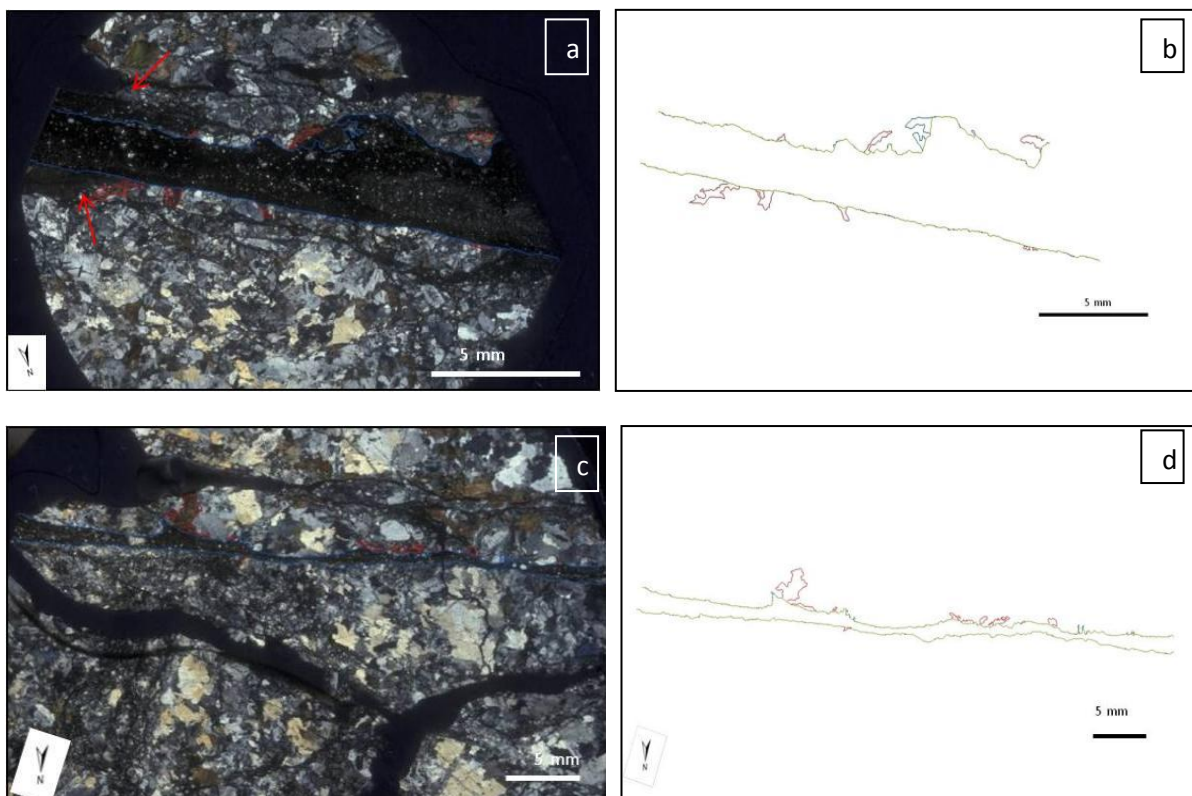


Figure 19. Neutral domains. Scan of thin sections (crossed nicols). **a)** Sample A02_02(Fault 2) and **b)** only drawn profile. **c)** Sample A4 (Fault 3) and **d)** profile only. Biotite in red. North is pointing downward.

Sample A02_02: the bottom profile (to the South) is more straight than the top one, where a large embayment in correspondence of biotite and very damaged quartz and plagioclase grains. In the fault vein, survivor clasts are more fine grained and rounded, whereas in the embayment clasts are angular not rounded and have larger grain size. The fault vein records more events of pseudotachylite production (left side of picture a, red arrows). In the thin section, the fault vein is 20 mm long.

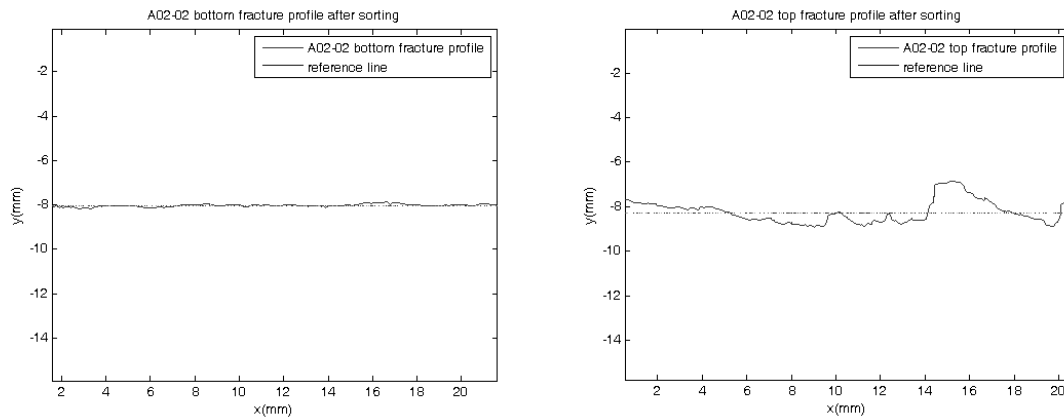


Figure 20 Profiles of sample A02_02 obtained with MatLab script. Left: bottom profile(to the North) of fault vein 2. Right: top profile (to the South)

Sample A4: in the bottom profile (to the north), the host rock has a more cataclastic fabric than in the top profile. The latter has big embayments corresponding to biotite grains in the wall rock which result in a larger micro-roughness of this profile with respect to the northern one (see ω_0 value in table for A4 sample). In the thin section, the fault vein is 33 mm long.

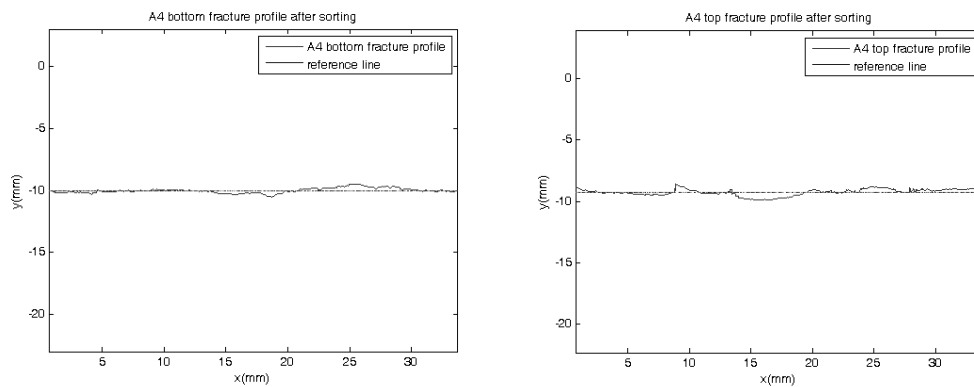


Figure 21 Profiles of sample A4 obtained with MatLab script. Left: bottom profile(to the North) of fault vein 2. Right: top profile (to the South)

A02_04 and A7: compressional domain

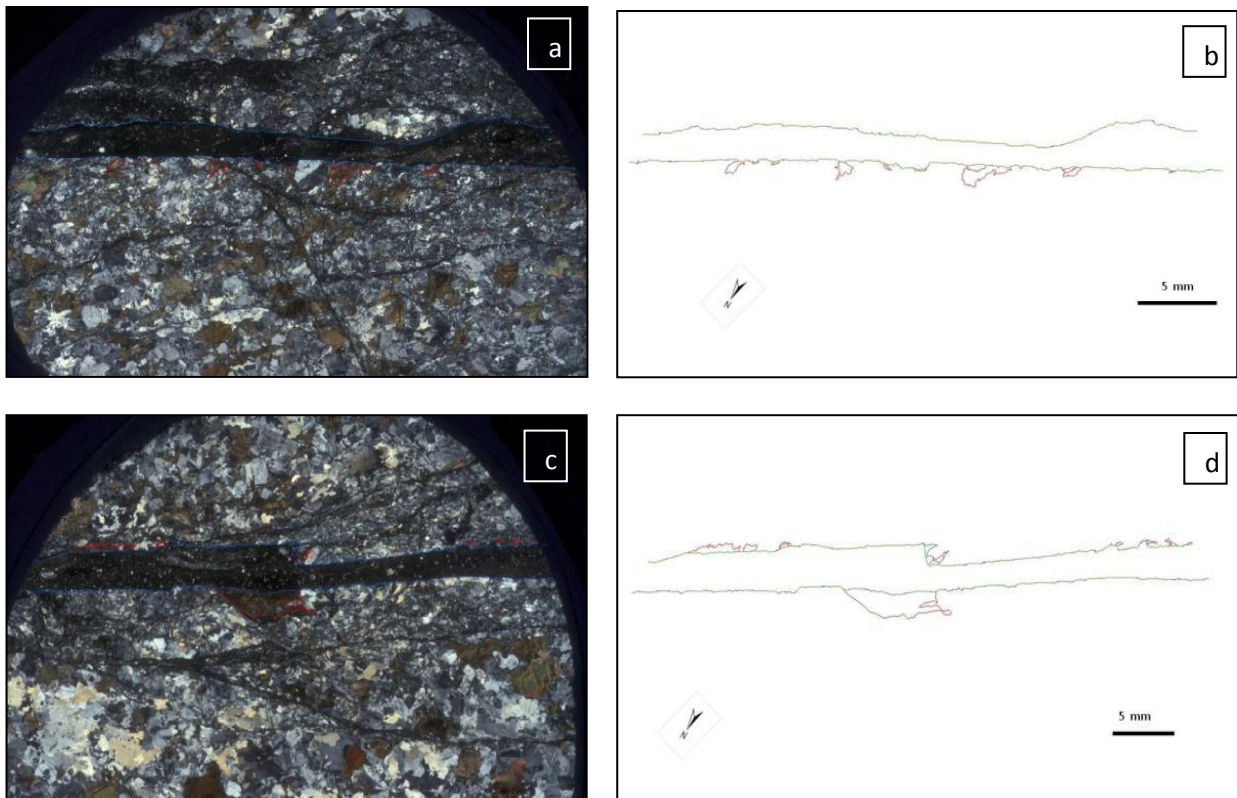


Figure 22. Compressional domain. Scan of thin sections (crossed nicols). **a)** Sample A02_04 (Fault 2) crossed nicols and **b)** profile drawn. **c)** Sample A7 (Fault 4) crossed nicols and **d)** profile drawn.

Sample A02_04: the top profile (to the south) is more irregular than the bottom profile. In the top profile a deep embayment is present in correspondence of a biotite grain in the wall rock and the transition from the biotite grain to the quartz grain is steep. In the pseudotachylyte matrix are present millimeter long agglomerates of quartz, plagioclase and biotite. In the scanned thin section the fault vein is 32 mm long (Fig. 24a).

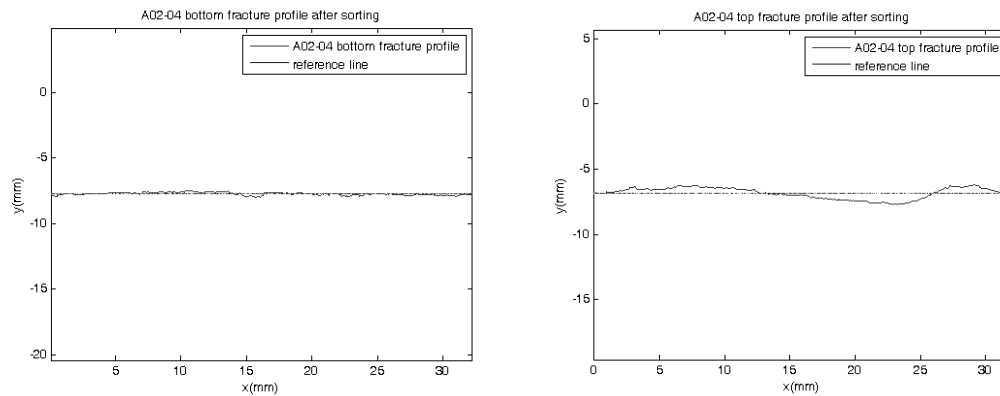


Figure 23 Profiles of sample A04_04 obtained with MatLab script. Left: bottom profile(to the North) of fault vein 2. Right: top profile (to the South)

Sample A7: also here the bottom profile (to the north) is more regular than the top profile. An about 5 mm long embayment in correspondence of a biotite grain interrupts the sharp bottom profile. A step of about 2 mm in the top profile is visible where an incipient fracture is developing (Fig 24c). In matrix there are few lithic clast embedded, and when present, they have a rounded shape and are < 100 μm in size. The fault vein in the thin section is 31 mm long.

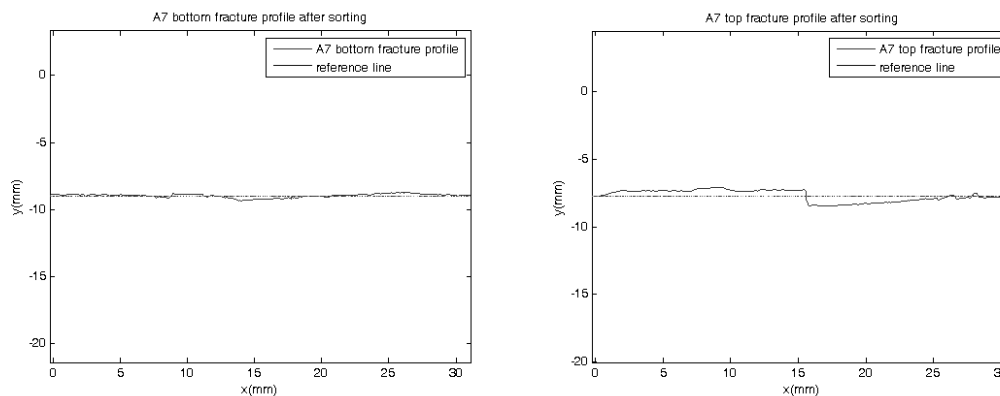


Figure 24 Profiles of sample A7 obtained with MatLab script. Left: bottom profile(to the North) of fault vein 2. Right: top profile (to the South)

A5: extensional domain

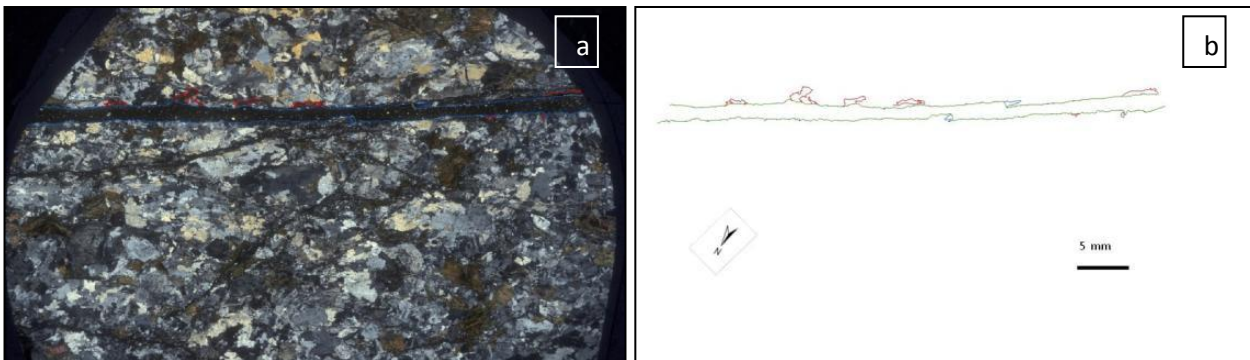


Figure 25 Extensional domain. **a)** Scan of thin section (crossed nicols) sample A5 (Fault 4) and **b)** profile drawn.

Sample A5 has more embayments in correspondence of biotite grains in the top profile (to the south) than in the bottom profile. The presence of cataclastic domains bordering the fault vein, both at the top and bottom profiles, is evidence of large wear of the wall rocks. Instead, when there is no evidence of damage in the grains in the wall rock at the contact with the pseudotachylyte, the profile is straight (Fig. 27). In the matrix there are few lithic clasts embedded. In the thin section the Fault vein is 31 mm long.

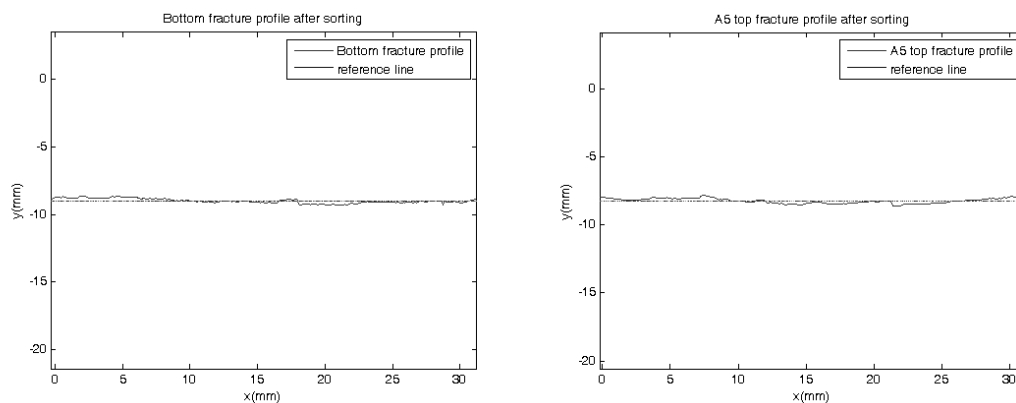


Figure 26 Profiles of sample A7 obtained with MatLab script. Left: bottom profile(to the North) of fault vein 2. Right: top profile (to the South)

Sample	Rock type	λ		ω_0		$\tau_{ss} V$
		(mm)	s.d.	(mm)	s.d.	(MW m ⁻²)
A1 dx (vs. West)	Tonalite	0,922	0,331	0,438	0,008	0
A1 sx (vs. East)	Tonalite	1,92	0,55	0,677	0,008	0
A2 dx (vs. West)	Tonalite	1,005	0,121	0,693	0,018	0
A2 sx (vs. East)	Tonalite	0,857	0,178	1,055	0,023	0
A2_02 top (vs. South)	Tonalite	0,855	0,318	0,464	0,004	70
A2_02 bottom (vs. North)	Tonalite	2,411	0,435	0,069	0,000	70
A02_04 top (vs. South)	Tonalite	0,912	0,088	0,407	0,004	100
A02_04 bottom (vs. North)	Tonalite	0,446	0,035	0,118	0,003	100
A4 top (vs. South)	Tonalite	0,540	0,115	0,229	0,004	70
A4 bottom (vs. North)	Tonalite	0,906	0,078	0,175	0,002	70
A7 top (vs. South)	Tonalite	1,326	0,283	0,422	0,000	100
A7 bottom (vs. North)	Tonalite	1,201	0,389	0,138	0,001	100
A5 top (vs. South)	Tonalite	1,576	0,534	0,183	0,002	50
A5 bottom (vs. North)	Tonalite	0,666	0,091	0,170	0,002	50

Table 2 In this table are summarize all MatLab data for natural samples from OM images. In the yellow column are reported indicative value of frictional power dissipated for the different structural domain.

Chapter 4 Microroughness in experimental faults

4.1 Experiments with SHIVA

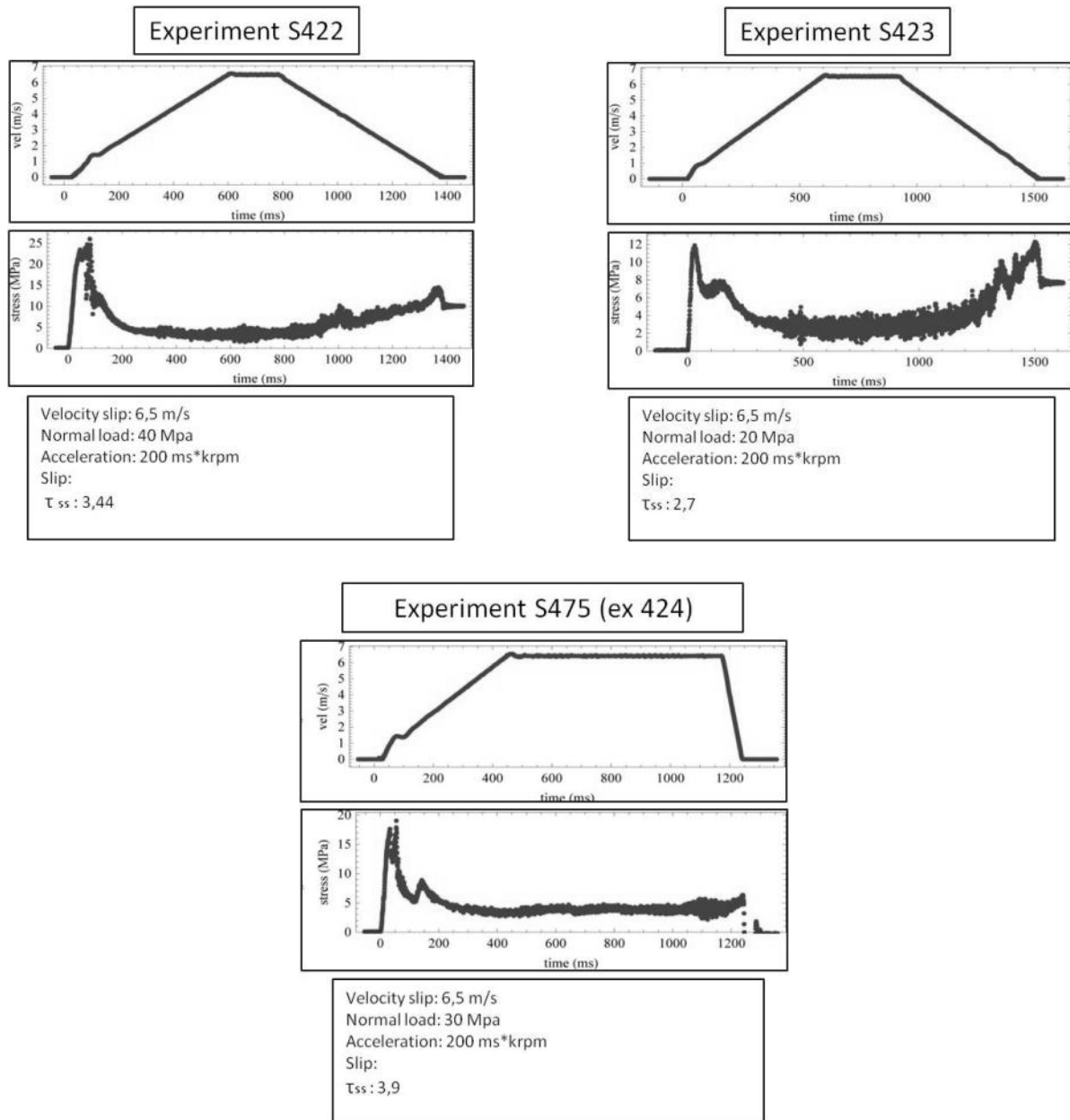
We performed three experiments with SHIVA on the Adamello tonalite to obtain micro-roughness data under controlled conditions of slip rate and normal stress (and thus for a known power density = τV [MW/m²]). These data will be compared with the micro-roughness measured in natural faults in section 5. Shear stress is determined by measuring the torque **T** and the normal load with two separate load cells (see Fig.7 in the section 2.2.1: the load cell that measures the torque is attached to the long arm departing from the axial column on the left side of SHIVA). Torque measurements are acquired at 25 kHz and, for cylindrical sample with known external radius r_{ext} and internal radius r_{int} , the instantaneous shear stress is (in MPa):

$$\tau = \frac{3T}{2\pi(r_{ext}^3 - r_{int}^3)} \quad (\text{Pa})$$

To gain microroughness data for different power densities, we performed the experiments at a target slip rate $V = 6.5$ m/s, but at different normal stresses (20, 30 and 40 MPa). For comparison, we included in this study an experiment (HVR376) performed on the same rock but under less extreme deformation conditions (normal stress = 20 MPa, Slip rate = 1.3 m/s). This experiment was performed with the rotary shear apparatus HV-1 installed in Kyoto (Di Toro et al., 2006).

4.1.1 Mechanical data

Here we reported only the data used to calculate the steady-state shear stress. For each experiment there are three graphs indicating velocity versus time and stress versus time. Graphs for HVR376 are missing, but steady-state and slip rate are reported in Table 3. In this table it is possible to read the frictional power dissipated in each experiment.



In experiment S422, the shear stress reaches a first peak of 25 MPa at the initiation of sliding, followed by an abrupt decrease in shear stress to 13-14 MPa, probably related to sample failure, and by a small second peak in shear stress (about 15 MPa). After the second peak, the shear stress decays towards steady-state (about 3.4 MPa), which is achieved in 0.2-0.3 s. After 1 s of slip, the sample is decelerated and shear stress increases. A similar evolution is observed for experiments S423 and S475. Also these experiments, performed at a lower normal stress, have a clear second peak (after 0.1-0.15 s) in shear stress. At the end of experiment S423 a significant re-strengthening concomitant to sample deceleration is observed. As observed and discussed in previous studies (Del Gaudio et al., 2009; Niemeijer et al., 2011) longer the deceleration, larger the re-strengthening. The curves are a bit noisy

because of discontinuous melt extrusion (samples are not laterally confined) during the experiment, and failure of rock bits. Nevertheless, with the exception of experiment S423, that broke after 0.4 s of slip, the shear-stress curves are neat. From the value of slip velocity at steady-state and from the steady state shear stress, we determined the frictional power dissipation for each experiment (Table 3).

Experiment	Rock type	Acceleration (ms ² *krpm)	Velocity (m/s)	Normal load (MPa)	Slip	Tss V (MW/m ²)
S422	tonalite	200	6.5	40	n.d.	22.36
S423	tonalite	200	6.5	20	n.d.	17.55
S475	tonalite	200	6.5	30	n.d.	25.50
HRV 376	tonalite	n.d.	1.3	20	n.d.	5.02 ± 0,15

Table 3 Mechanical data of the experiments discussed in this thesis.

Though the experiment S422 was performed at a higher normal stress (40 MPa) than S475 (30 MPa) the shear stress at steady-state of S422 is slightly smaller. The difference might be in the experimental error and it is not discussed here.

4.2.2 Microroughness in experimental pseudotachylytes

The same method (see section 2) applied to determine the micro-roughness of the pseudotachylyte-tonalite boundary in natural samples was applied to the experimental samples. In addition to Optical Microscope (OM) images, SEM images were collected to obtain detailed microphotomosaics allowing a more precise investigation of the microroughness. For a comparison, all profiles and data are reported below (Optical Microscope and SEM).

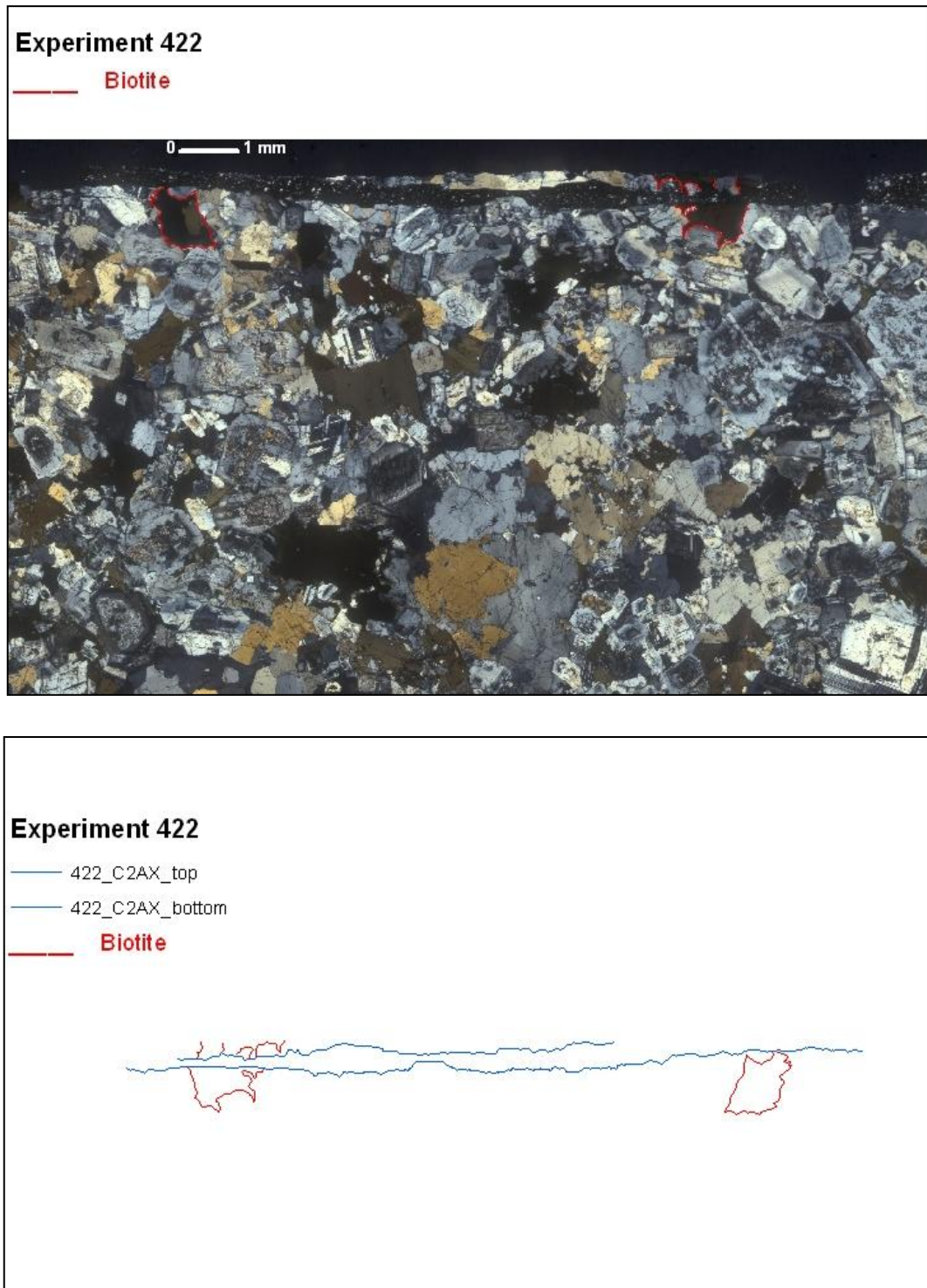


Figure 27 Experiment S422 in OM images (crossed nicols) and down profile drawn. Biotite in red.

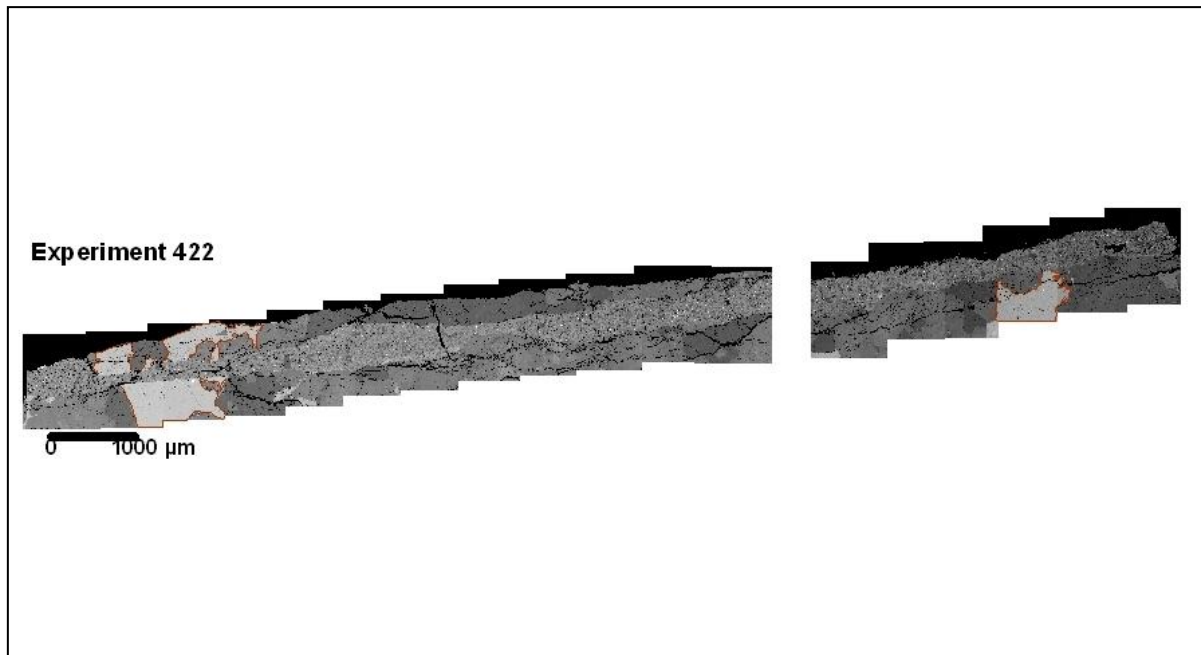
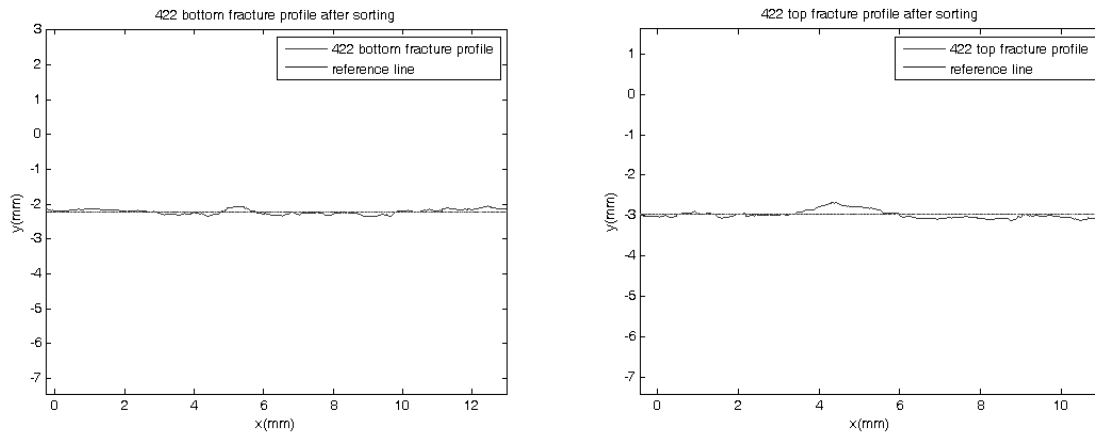


Figure 28 Experiment S422 in BSE-SEM images and down profile drawn. Biotite in red.



Experiment S422 was conducted at $V = 6.5$ m/s and $\sigma_n = 40$ MPa. The resulting frictional power dissipated was 22.35 MW/m². Under these extreme experimental conditions, the top and bottom profiles of the artificial pseudotachylyte – host rock boundaries are both straight. In particular, biotite minerals are sharply cut in the bottom profile. Instead, embayments form in correspondence of biotite in the top profile. The artificial pseudotachylyte has lithic clasts of quartz and feldspar (grain size ranging from <1 μm to 50 μm) suspended in the solidified melt (now glass) (Fig. 31). Feldspar clasts are rounded, whereas quartz clasts are angular in shape. The matrix is full of vesicles (diameters ranging from 1 to 20 μm) and hematite or magnetite grains (<10 μm in size, white color in SEM image) (Fig. 31).

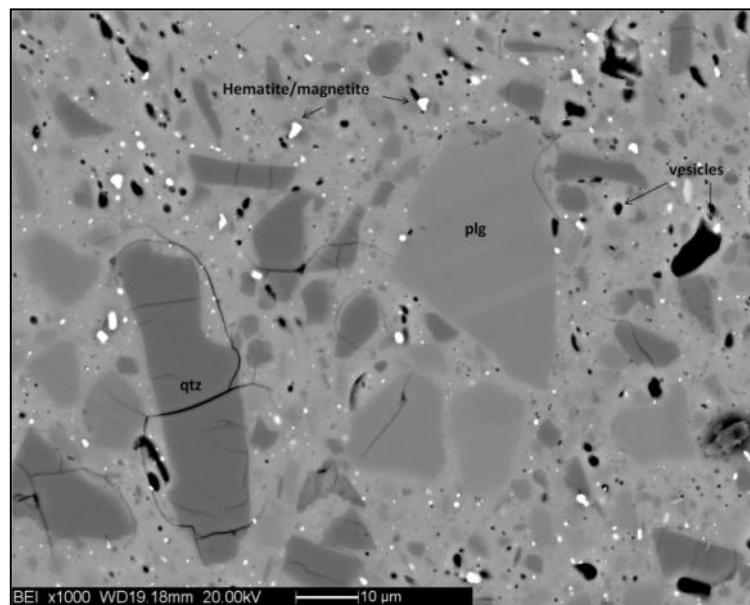


Figure 29 Back-scattered SEM image of the pseudotachylyte. Detail of vesicles, hematite/magnetite grains, rounded feldspar and angular quartz survivor clasts.

An angular survivor grain of apatite (melting point 1700°C) is found in the matrix. The fact that feldspar (melting point 1200°C) survivor clasts are rounded, are apatite and quartz (melting point 1700°C) grains are not, suggest that melt temperature was comprised between 1200 and 1700°C (Fig. 32).

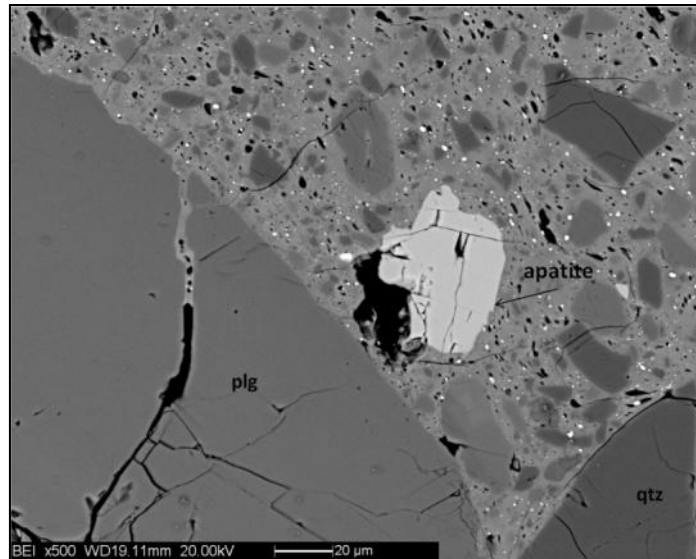


Figure 30 Detail of apatite mineral embedded in matrix. Note sharp boundary of the clast.

In the tonalite next to the pseudotachylyte, feldspar grains have aligned vesicles (usually along cleavage) interpreted as evidence of initial melting. Such alignments are found up to a distance of about 80 μm from the boundary with the pseudotachylyte (Fig. 33)

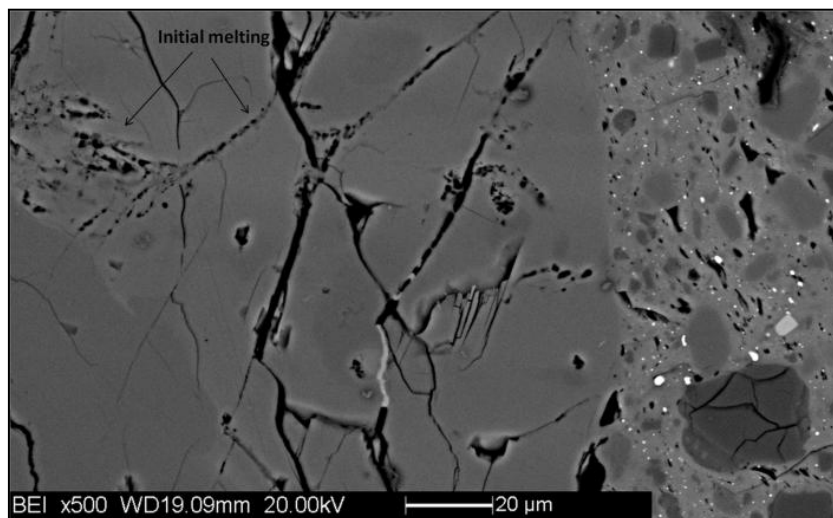


Figure 31 melting along fractures and cleavage surfaces inside feldspar grains in the wall rocks.

Similarly, biotite (melting point about 650°C) has evidences of melting (vesicles, etc.) up to a distance of 100 μm from the tonalite – rock pseudotachylyte boundary (Fig. 34).

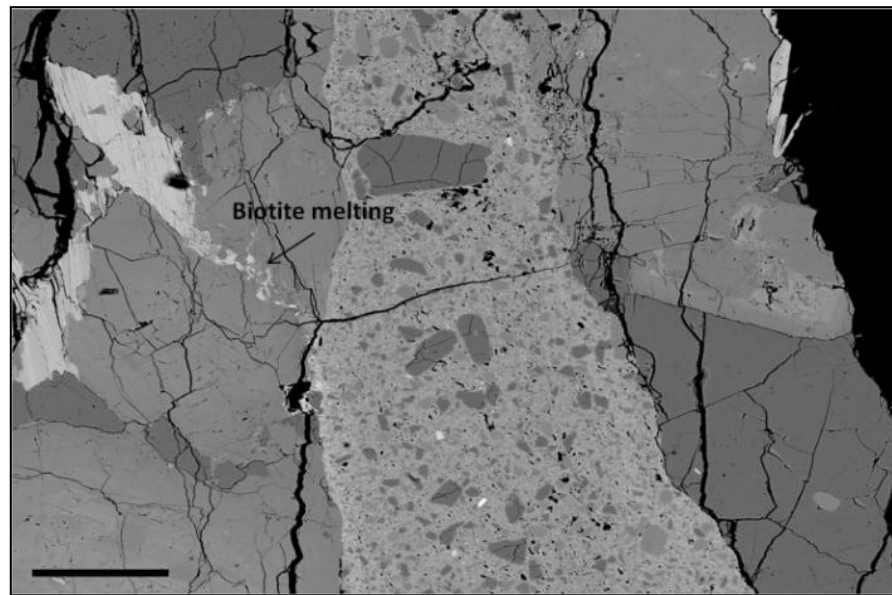


Figure 32 Melting Initial melting of biotite in the wall rocks. Biotite is entrapped between plagioclase and quartz minerals and melt tends to escape towards the fault vein to the right.

Initial melting of minerals (in the wall rocks) with different melting point and located at increasing distances from the fault vein can be used as gauge to estimate heat diffusion in the host-rock during the experiments, according to the relationship:

$$x \sim \sqrt{kt}$$

where k is the thermal diffusivity (about $10^{-6} \text{ m}^2/\text{s}$ for tonalite) and $t(\text{s})$ is time.

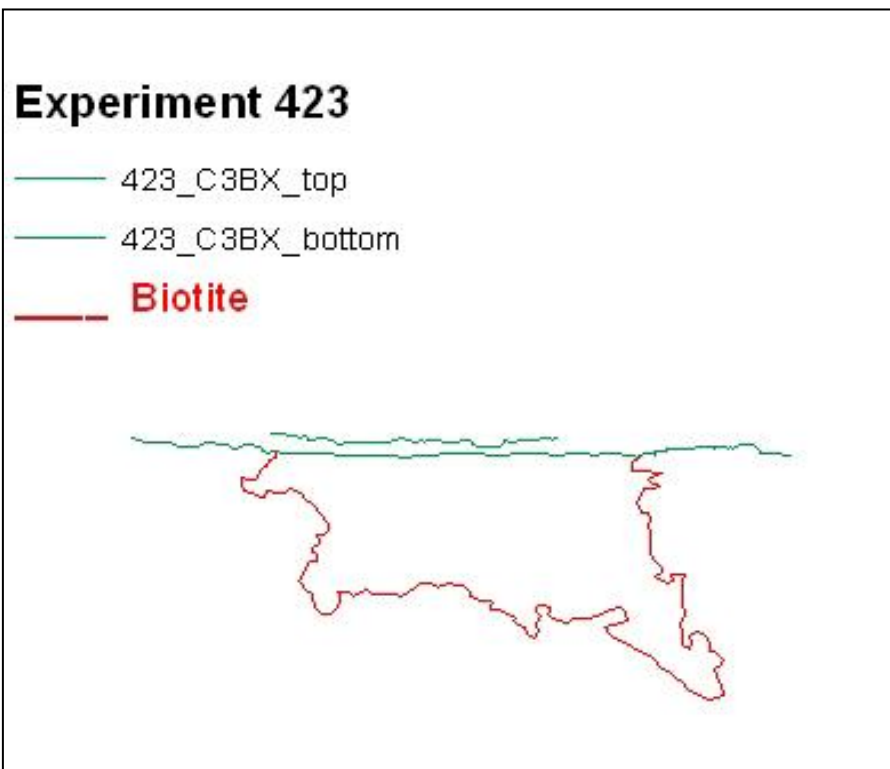
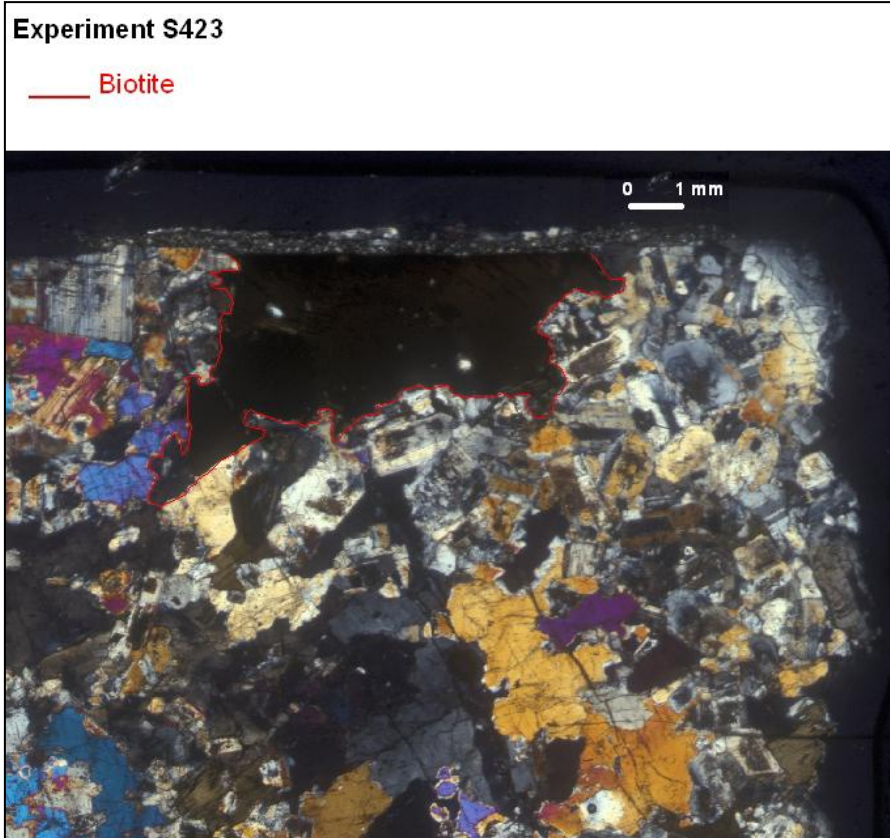


Figure 33 Experiment S423 in OM images (crossed nicols) and down profile drawn. Biotite in red.

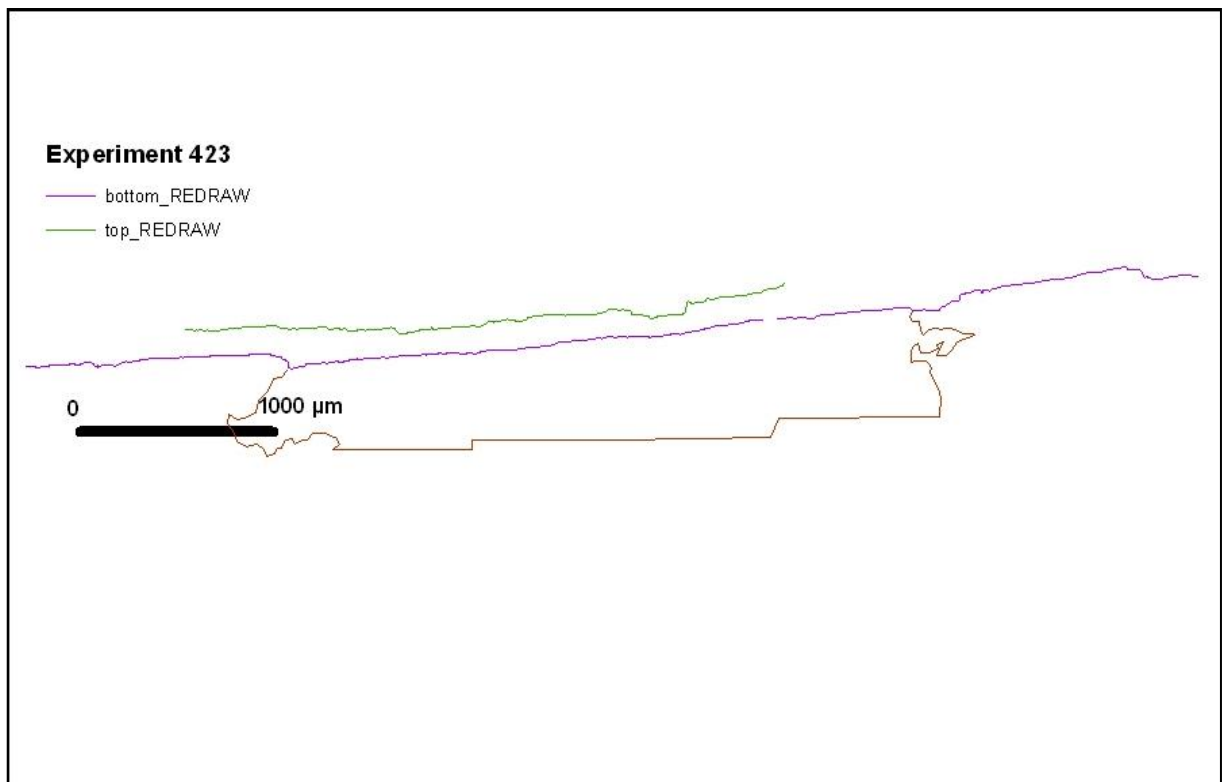
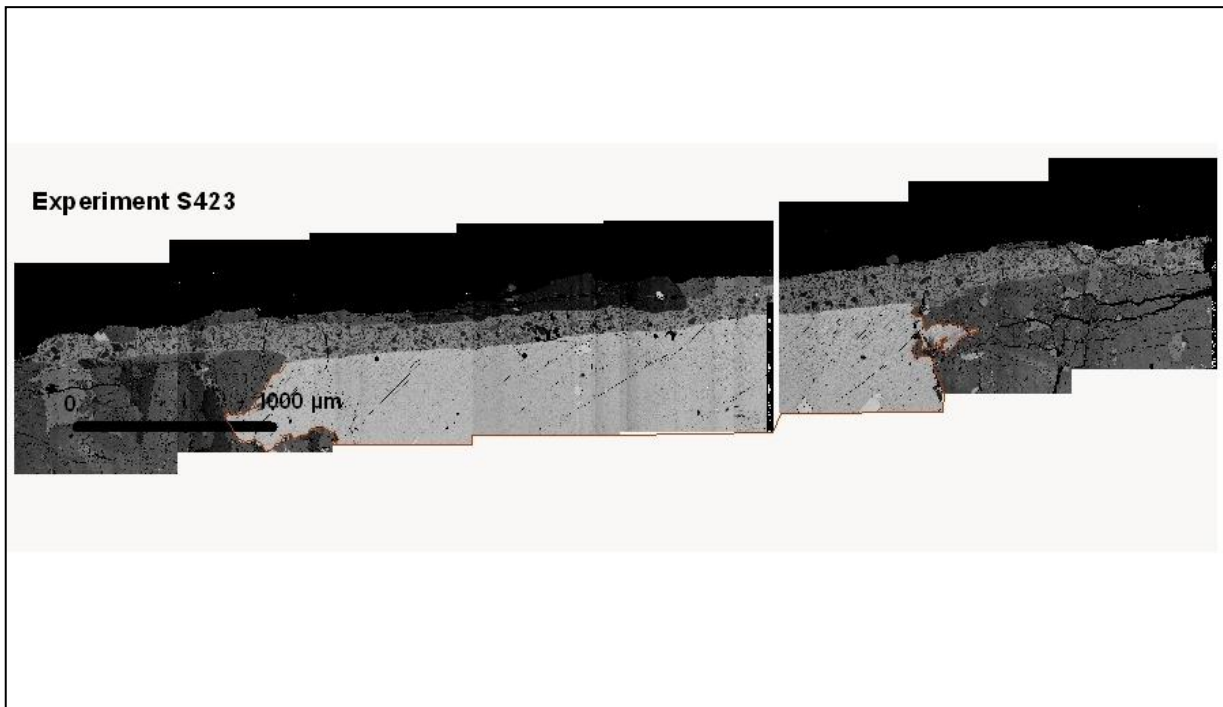
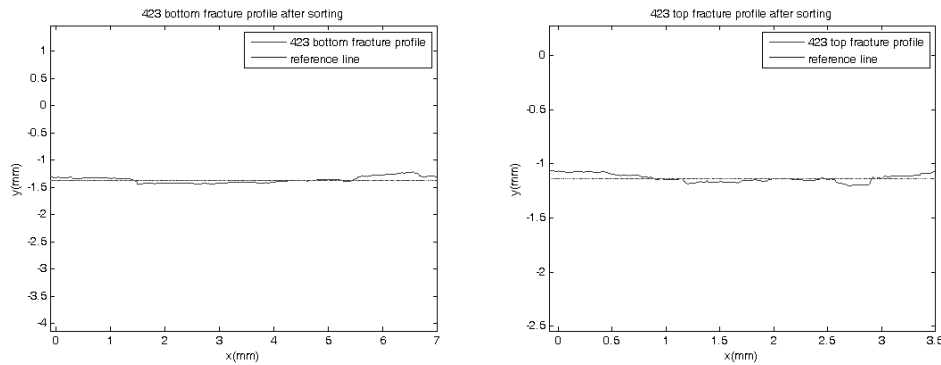


Figure 34 Experiment S423 in BSE-SEM images and down profile drawn. Biotite in red.



Experiment S423 was performed by imposing at a target slip rate $V = 6.5$ m/s and $\sigma_n = 20$ MPa. The resulting power dissipated at steady-state was 17.55 MW/m². In this case, the bottom profile is more irregular than top one (Table 3). A single biotite grain is present in the wall rocks: the pseudotachylyte-biotite boundary is straight and at embayment (in correspondence of the transition from biotite to feldspar grains in the tonalite wall rock) is about 10 μm deep. Similarly to S422, the pseudotachylyte consists of lithic clasts of quartz and feldspar (grain size ranging from < 1 μm to 50 μm) embedded in a glassy matrix. Suspended quartz grains have angular boundaries, whereas feldspars are more rounded. Vesicles, hematite or magnetite grains are less abundant if compared with experiment S422.

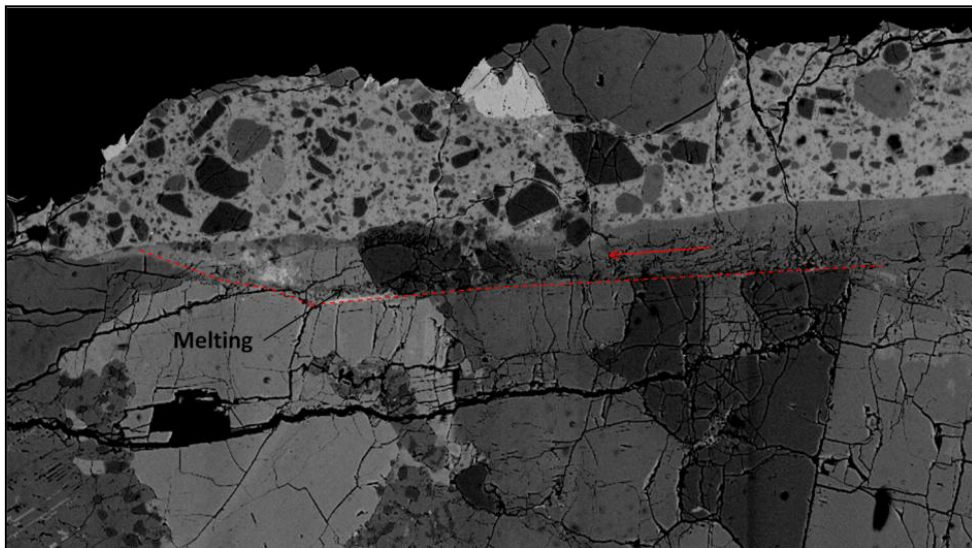


Figure 35 Particular of little shear zone

The pseudotachylyte-tonalite boundary shown in Fig. 37 evidences a truncated quartz grain which was separated with a sinistral sense of shear by a slipping zone (dashed red curve) in the wall rocks. The slipping zone is about 50 μm thick and decorated by solidified melt. Probably, incipient melting along cleavage and fractures in feldspar acted as a lubricant allowing slip in the wall rocks next to the main pseudotachylyte-bearing slip surface.

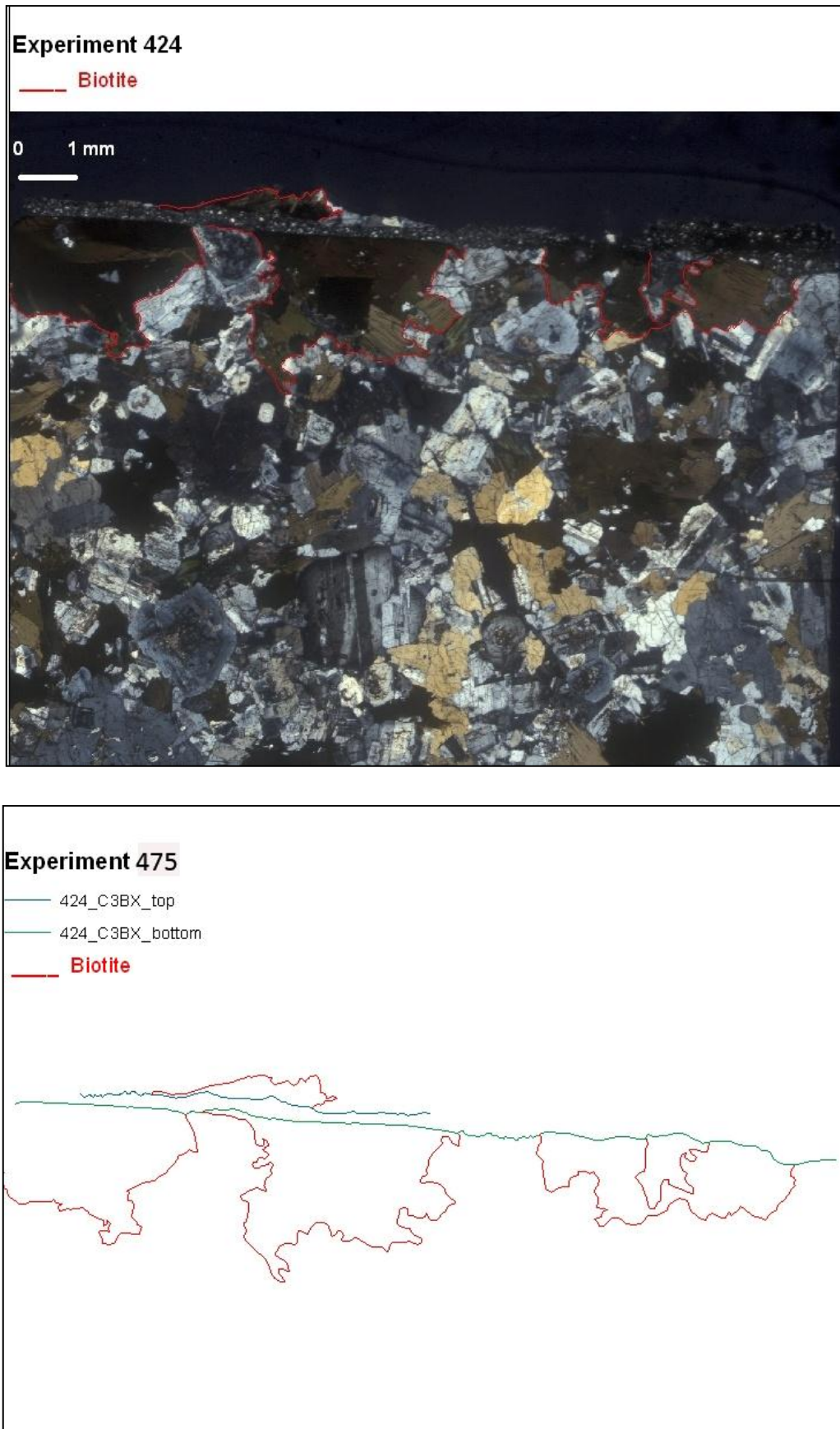


Figure 36 Experiment S475 in OM images (crossed nicols) and down profile drawn. Biotite in red.

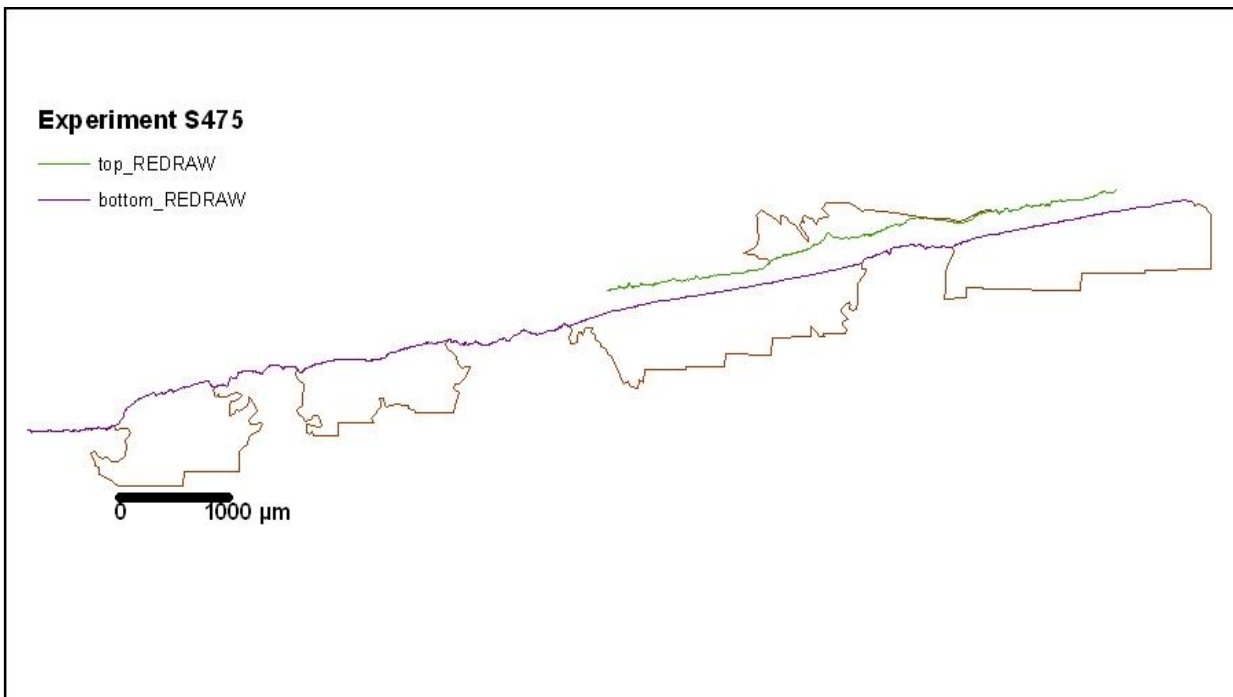
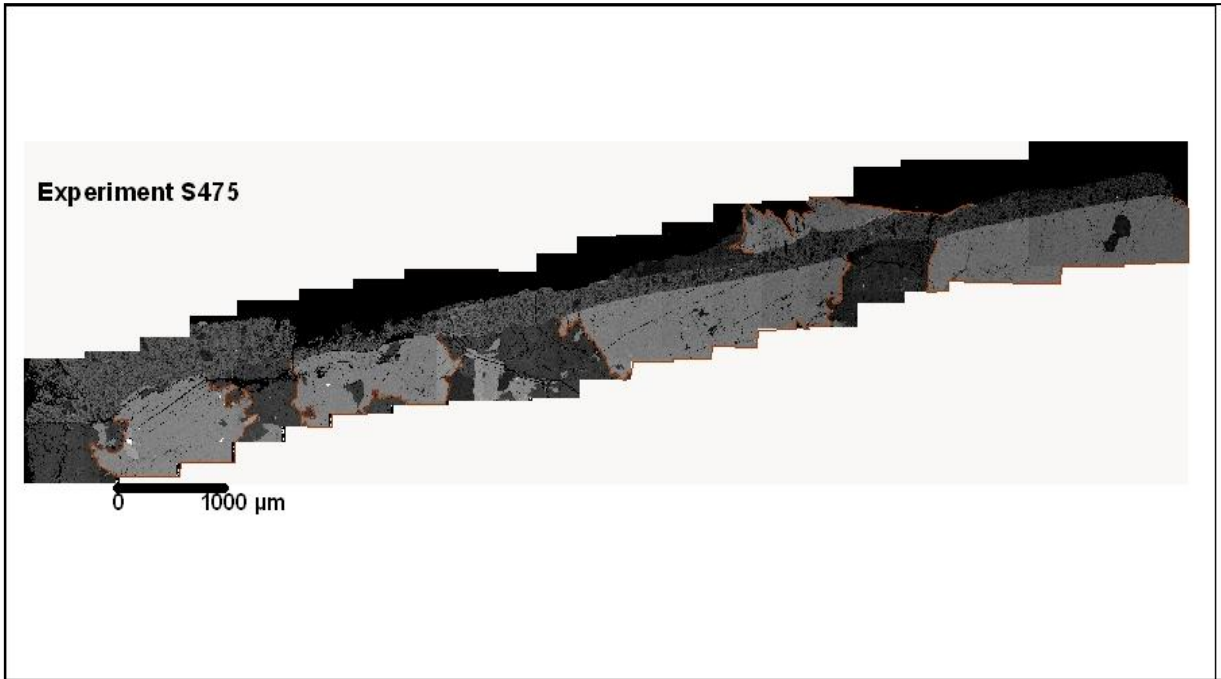
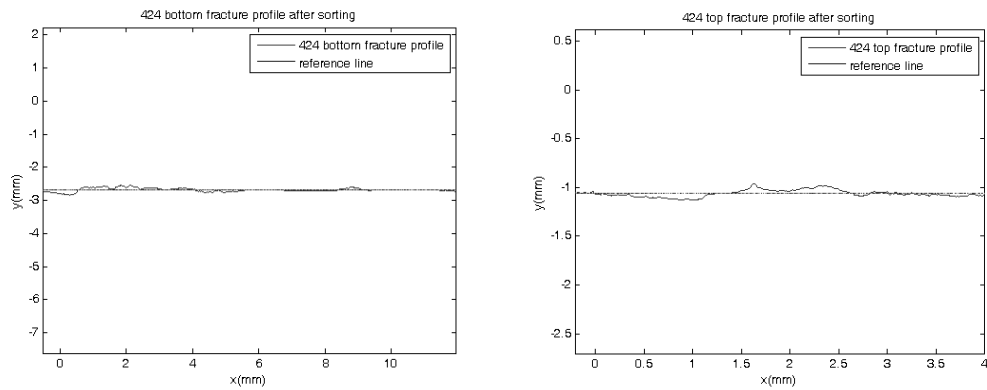


Figure 37 Experiment S475 in BSE-SEM images and down profile drawn. Biotite in red.



Experiment S475 was conducted at $V = 6.5\text{m/s}$ and $\sigma_n = 30\text{ MPa}$. The resulting frictional power dissipated at steady-state was 25.50 MW/m^2 . Along the bottom profile, biotite grains have a straight boundary with the pseudotachylyte; in one case, in the left side of profile, the biotite grains are in relief with respect to the neighbor quartz and feldspar grains. On the contrary, as it was the case for all the profiles described so far, embayments in correspondence of biotite grains are present (Fig. 40).

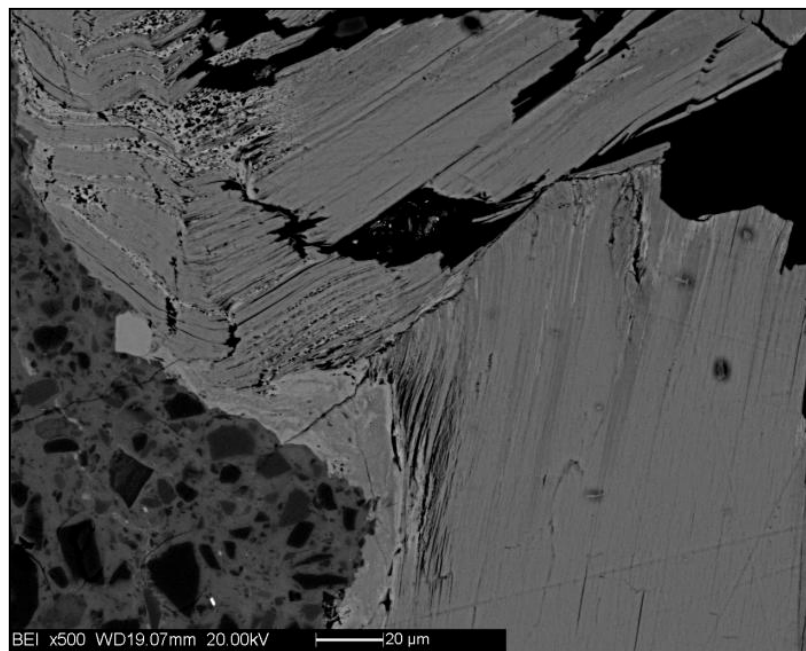


Figure 38 Particular of biotite embayment from experiment S475 with evidence of initial melting along cleavage surfaces.

Similarly to the previous experiments (S422 and S423), the pseudotachylyte consists of lithic clasts of angular quartz grains and rounded feldspar grains (grain size ranging from $< 1\text{ }\mu\text{m}$ to $50\text{ }\mu\text{m}$ for both) embedded in a glassy matrix.

Details of biotite grains at the contact with the glass show initial melting along cleavage surfaces and kinking of the cleavage (Fig 41).

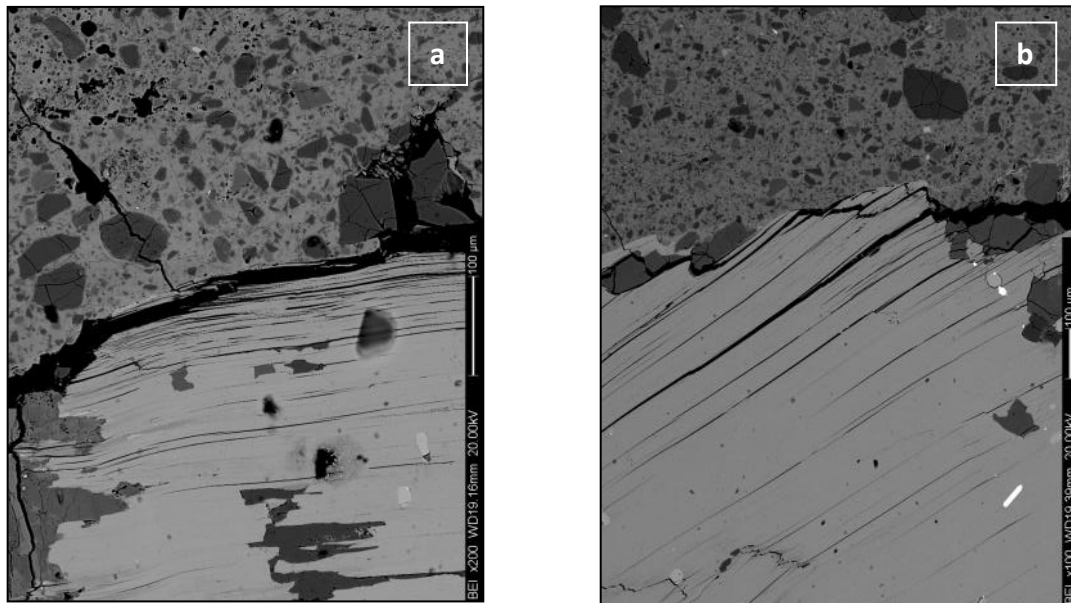


Figure 39 Particular of biotite with basal plane parallel to slip direction (a) and near parallel (b) to slip direction.

An image of biotite melting was taken, where is possible to see how minerals are broken and dragged within matrix (Fig. 42a). Around survivor clasts is visible a thin film of biotite-melt (white color). After melting, biotite is dragged into the matrix (Fig. 42b), so that in proximity of crystal, matrix presents light grey colour respect the rest of matrix.

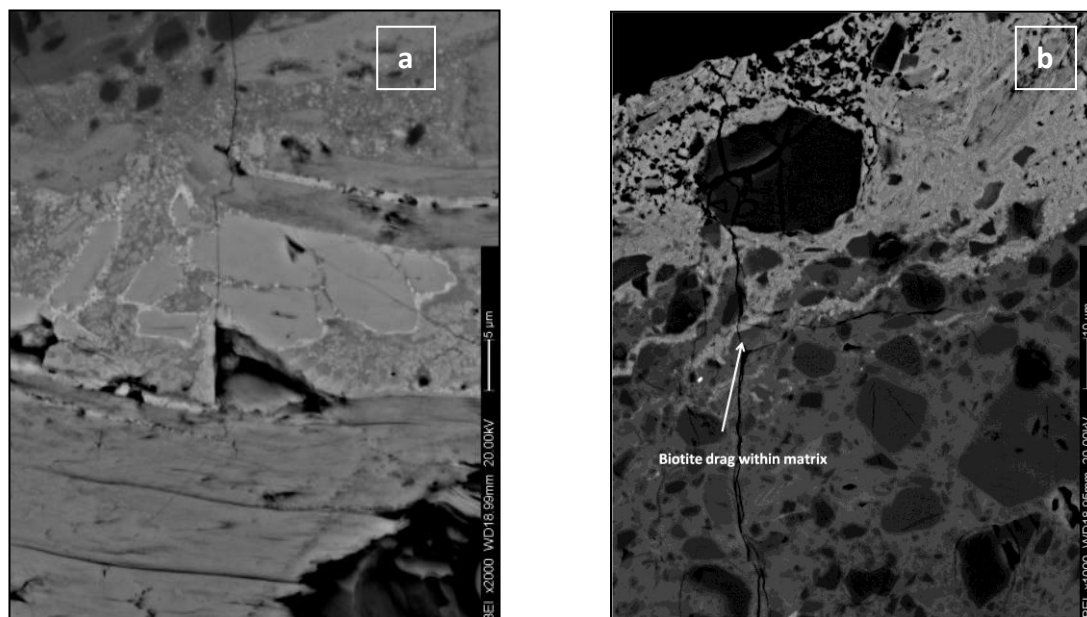


Figure 40 Particular of biotite melting and biotite-rich melt. a) fractured biotite grain dragged within melt and surrounded by thin layer of melted biotite; b) evidence of mingling the biotite-rich melt (whitish in color) with the feldspar-rich melt (grayish in color) wrapping a quartz survivor clast.

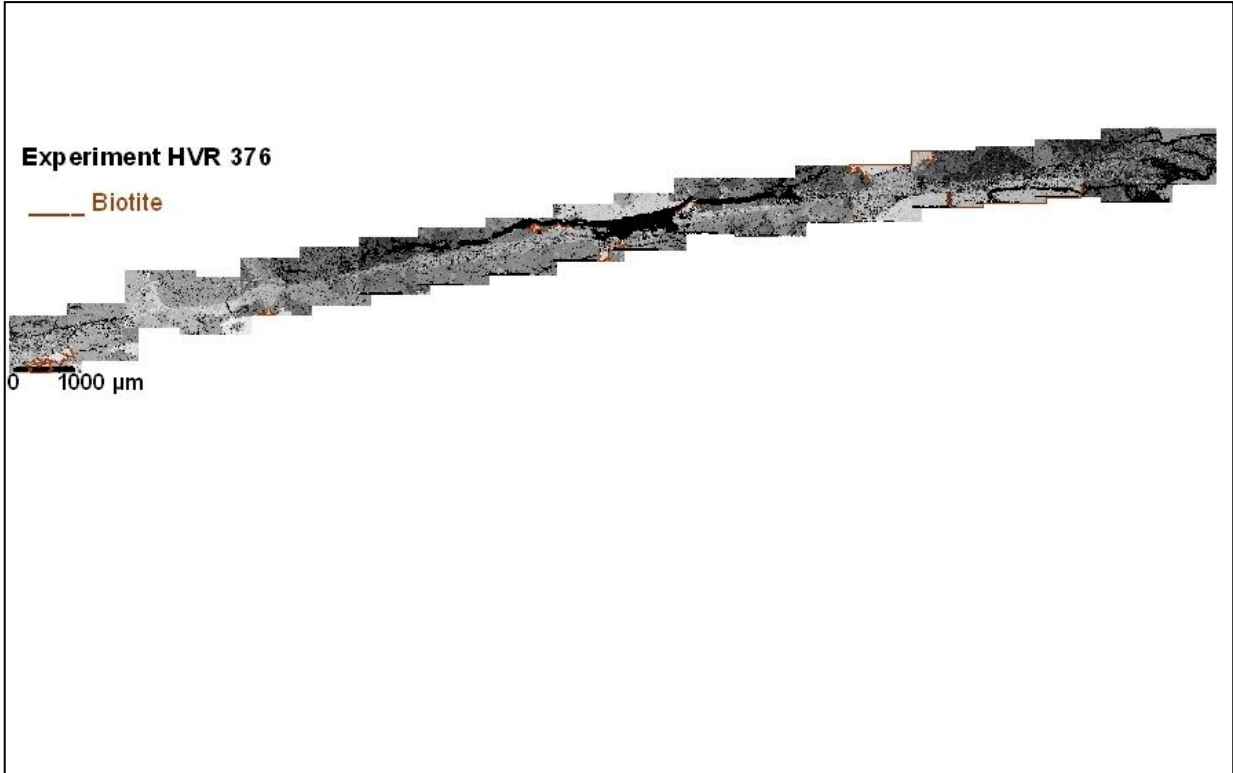
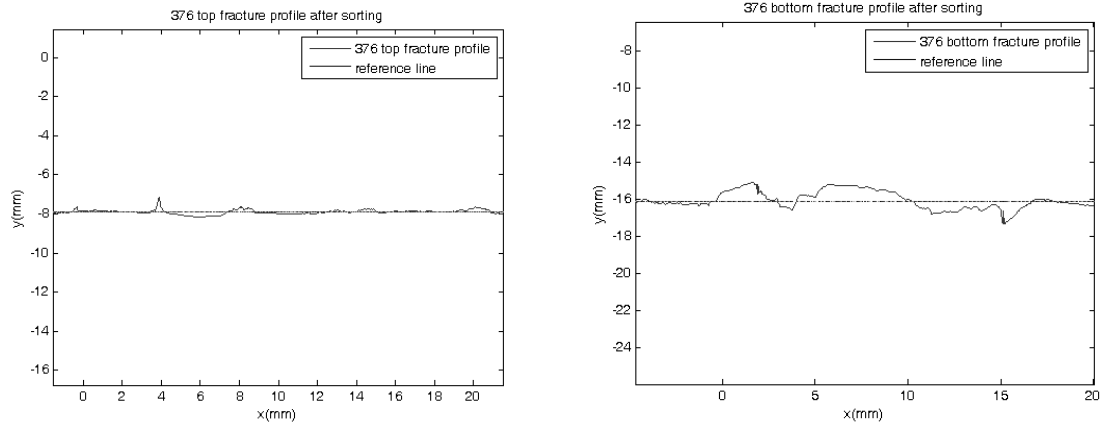


Figure 41 Experiment HVR376 in BSE-SEM images and down profile drawn. Biotite in red.



Experiment HVR376, was conducted on tonalite from the same outcrop at $V = 1.3$ m/s and $\sigma_n = 20$ MPa (Di Toro et al., 2006). The resulting frictional power dissipated was 5.02 MW/m². The sample was 23 mm in diameter (against the 50 mm of the experiments described so far) and an external aluminum ring, 1 mm thick, was emplaced before the experiment to sustain the walls of the tonalite sample. The thin section was cut perpendicular to the fault slipping zone and passes through the center of the sample. The profile represents the entire pseudotachylyte-wall rock boundary of the sample, though it should be almost orthogonal to the slip vector. Both the top and bottom boundary profiles are very irregular, with bottom more irregular than top one (see value in Table 4). As was found in all the experiments described so far, embayments along the boundary are deep in correspondence of biotite grains in the wall rocks and the pseudotachylyte consists of quartz (angular) and feldspar (rounded) grains suspended in a grayish in color (under the SEM-BSE) glassy matrix. At the center of profile and at the edges, a huge amount of vesicles (from 5 to 50 μm in size) is present. Also hematite/magnetite grains are abundant in the matrix (<10 μm in size). An intense fracturing of tonalite is visible at the sample edges, where the sample was in contact with the external aluminum ring.

Sample	Rock type	λ		ω_0		$\tau_{ss} V$	ω_0 / λ	λ / ω_0	Technique
		(mm)	s.d.	(mm)	s.d.	(MW m ⁻²)			
HVR376 top	tonalite exp	0,173		0,080		5,02	0,459755	2,175	SEM
HVR376 bottom	tonalite exp	0,158		0,101		5,02	0,636955	1,570	SEM
S422_C2A top	tonalite exp	0,204	0,037	0,092	0,001	22,36	0,449314	2,226	SEM
S422_C2A bottom	tonalite exp	0,132	0,022	0,071	0,000	22,36	0,542114	1,845	SEM
S423_top	tonalite exp	0,190	0,042	0,034	0,000	17,55	0,180333	5,545	SEM
S423_bottom	tonalite exp	0,233	0,030	0,052	0,001	17,55	0,220966	4,526	SEM
S475 top	tonalite exp	0,095	0,016	0,031	0,001	25,50	0,330003	3,030	SEM
S475 bot	tonalite exp	0,183	0,036	0,059	0,001	25,50	0,320674	3,118	SEM

S422_C2A top	tonalite exp	0,944	0,512	0,070	0,001	22,36	0,074153	13,486	OM
S422_C2A bottom	tonalite exp	0,559	0,320	0,116	0,000	22,36	0,207513	4,819	OM
S423_top	tonalite exp	0,689	0,076	0,043	0,001	17,55	0,062409	16,023	OM
S423_bottom	tonalite exp	0,617	0,108	0,059	0,001	17,55	0,095624	10,458	OM
S475 top	tonalite exp	0,835	0,489	0,04	0,001	25,50	0,047904	20,875	OM
S475 bot	tonalite exp	0,860	0,292	0,062	0,001	25,50	0,072093	13,871	OM

Table 4 Summarize of experimental data both for SEM and OM data.

Curiously, ω_0 (characteristic elevation of the asperities) and λ_{ave} (average micro-roughness asperity radius) are both different for the same profile described with OM and SEM images (see Table 4). This is a characteristic feature of all the measurements we performed in experimental samples. The difference for ω_0 is in the experimental error, but λ_{ave} is 3-8 times larger in profiles obtained from OM images than from SEM profiles. One explanation could be that the description of the micro-roughness is more detailed in SEM than in OM images and, in SEM images, small asperities can be drawn.

Chapter 5 Discussion

5.1 Comparison between natural and experimental microroughness

We can summarize as follows the microroughness measurements obtained for natural and experimental samples.

5.1.1 Microroughness in natural samples

In nature we recognize pure tensional domains in injection veins, and extensional, neutral and compressional domains in fault veins. We assume that, since the effective stress normal to the fault increases from a tensional crack (stress normal to the fault balanced by the fluid pressure) to the extensional, neutral and compressional domains (the latter being the largest), the power dissipated along a fault during seismic slip increases from the injection veins to the other domains.

Sample	λ		$\omega 0$		$\tau_{ss} V$		$\omega 0 / \lambda$	$\lambda / \omega 0$	notes
	(mm)	s.d.	(mm)	s.d.	(MW m ⁻²)	s.d.			
A1 west	0,922	0,331	0,438	0,008	0				injection vein
A1 east	1,92	0,55	0,677	0,008	0				injection vein
A2 west	1,005	0,121	0,693	0,018	0		0,689921	1,449	injection vein
A2 east	0,857	0,178	1,055	0,023	0		1,231438	0,812	injection vein
A2_02 top (vs. S)	0,855	0,318	0,464	0,004	70	40	0,542404	1,844	neutral/comp
A2_02 bot (vs.N)	2,411	0,435	0,069	0,000	70	40	0,028594	34,972	neutral/comp
A02_04 top (vs. S)	0,912	0,088	0,407	0,004	100	40	0,445966	2,242	comp
A02_04 bot (vs. N)	0,446	0,035	0,118	0,003	100	40	0,265084	3,772	comp
A4 top (vs. S)	0,540	0,115	0,229	0,004	70	40	0,424454	2,356	neutral
A4 bot (vs. N)	0,906	0,078	0,175	0,002	70	40	0,193647	5,164	neutral
A7 top (vs. S)	1,326	0,283	0,422	0,000	100	40	0,318293	3,142	comp
A7 bot (vs. N.)	1,201	0,389	0,138	0,001	100	40	0,114735	8,716	comp
A5 top (vs. S)	1,576	0,534	0,183	0,002	50	40	0,115807	8,635	extension
A5 bot (vs. N)	0,666	0,091	0,170	0,002	50	40	0,255283	3,917	extension

We reported the natural data shown in the table above in the diagrams above (all the data were obtained from optical microscope (OM) images).

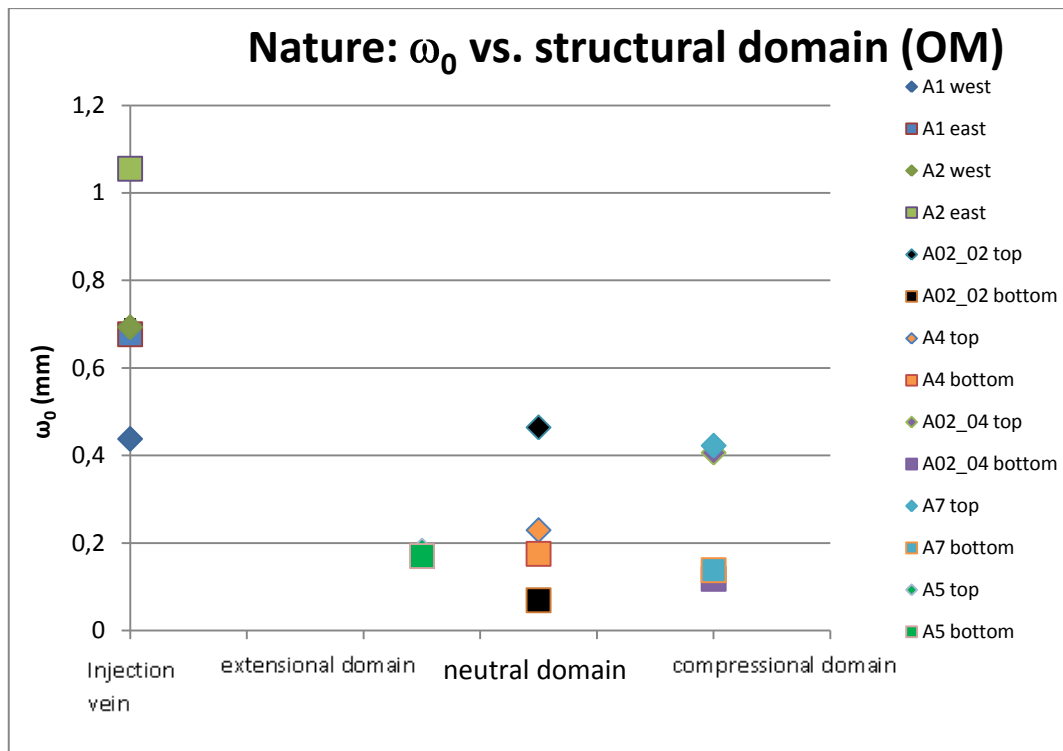


Figure 42 Characteristic asperities high versus frictional power dissipated for different structural domain. An evident trend where ω_0 decrease with increasing power dissipated is reported.

Clearly, ω_0 decreases switching from the microroughness measured in injection veins towards the microroughness measured in extensional, neutral and compressional domains of fault veins: ω_0 decreases with the frictional power dissipated on the fault surface during seismic slip. Note that the ω_0 values of the top profiles, corresponding to the South profile of the pseudotachylite-tonalite boundary, are systematically larger than the bottom profiles (corresponding to the geographic North). This is consistent with the larger abundance of injection veins intruding the southern sector of the Gole Larghe Fault Zone and interpreted as resulting from seismic rupture directivity (Di Toro et al., 2005). In the case of a strike-slip dextral fault striking East-West, for a crack propagating from the West to the East, the stress perturbation at the rupture tip induces a tensional stress field in the southern block and a compressive one in the northern block. Since rocks are ten times weaker in tension than in compression (~20 MPa vs. ~200 MPa in the case of tonalite), this asymmetric stress perturbation will result in larger damage in the Southern wall rock than in the Northern wall rock (Di Toro et al., 2005).

Assuming, for strike-slip faulting, a typical stress normal to the fault at a depth of 10 km, a hydrostatic pore pressure and a seismic slip rate of $V = 1 \text{ m/s}$, we might attribute a representative frictional power density to each domain as follows (see discussion in Griffith et al., 2010):

- 0 MW/m^2 for injection veins (the tangential slip rate to the surface is 0 m/s);

- 50 MW/m² for extensional domains;
- 70 MW/m² for neutral domains;
- 100 MW/m² for compressional domain.

We plot below ω_0 vs. frictional power for natural samples. Given the quite poor assumptions we introduced a large error bar corresponding to ± 30 MPa for the frictional power. Instead, for the measured ω_0 , the standard deviations are smaller than the symbol.

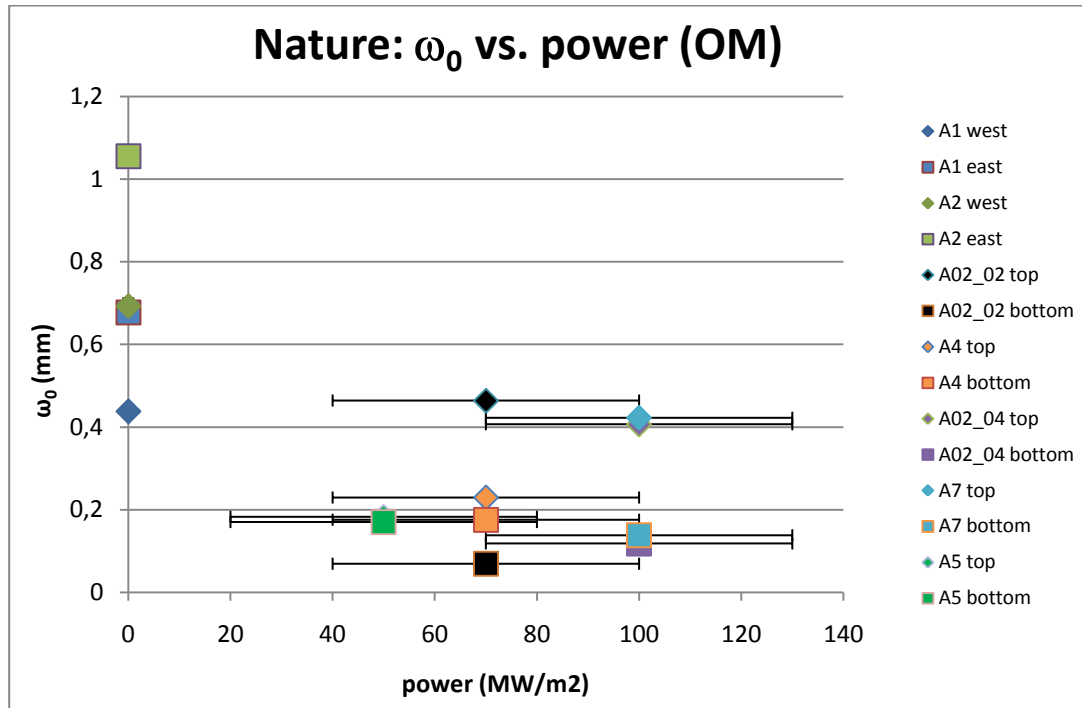


Figure 43 ω_0 versus power dissipated. In this graph are reported error bars to indicate that values for different domains are indicative.

Given the above assumptions, in nature ω_0 decreases with increasing power density.

We reported below λ_{ave} versus frictional power density.

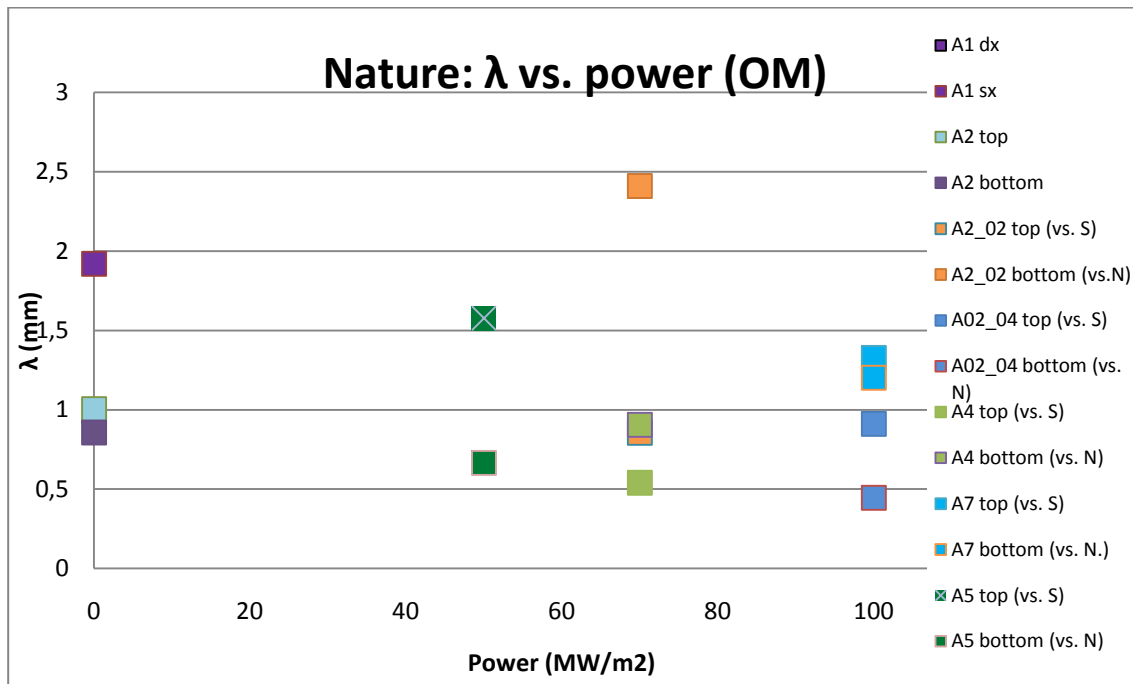


Figure 44 Characteristic average radii of asperities versus frictional power: λ_{ave} has an independent behavior from frictional power dissipation.

According to our data, the scattering of λ_{ave} suggests that the average roughness wavelength is independent of the structural domain and, as a consequence, of the frictional power dissipated. We plot below λ_{ave} vs. ω_0 .

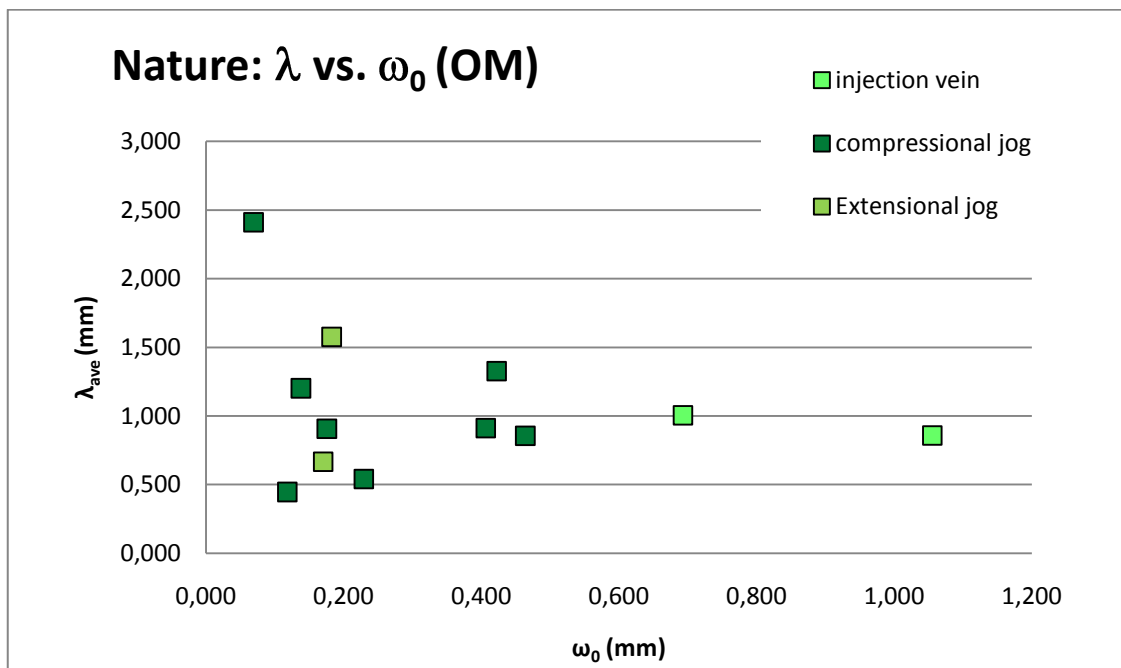


Figure 45 λ_{ave} versus ω_0 : even with some scatter, in this case λ_{ave} decrease with increasing ω_0 and approaching value 1.

In the above diagram, even if with some scatter, λ_{ave} decreases with ω_0 and tends to 1 at large ω_0 . Nielsen et al. (2010) discussed that with increasing penetration of the heat wave at lower power dissipated, this would result in large ω_0 and λ_{ave} should decrease because the curvature of the asperity becomes smaller. However, significant variations in λ_{ave} could result from the outlier.

If we plot ω_0 / λ_{ave} vs. frictional power, see below, we find a similar trend as in the previous diagram.

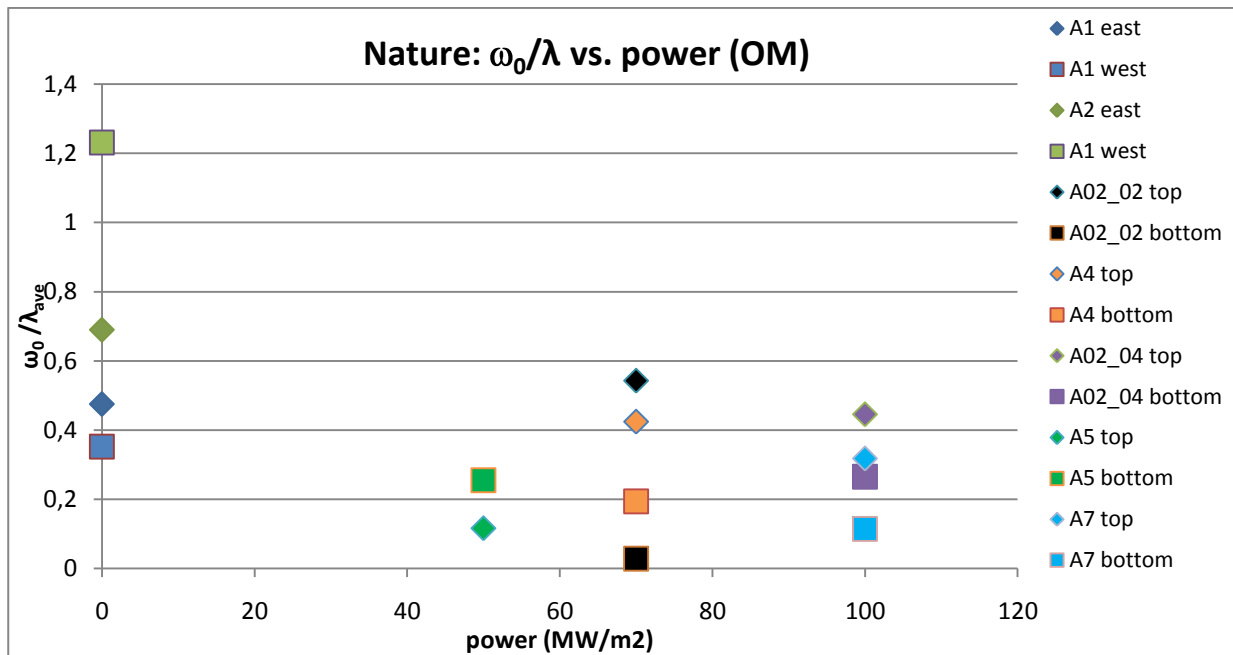


Figure 46 ω_0 / λ_{ave} versus frictional power: a similar trend like in Fig. 30 is found

For (assumed) power densities $\rightarrow 30 \text{ MW/m}^2$, $\omega_0 / \lambda_{ave} \sim 0.3$ and it is independent of the frictional power density (and of the structural domain). This result is at odds with the assumption of $\omega_0 / \lambda_{ave} \approx 1$ in Nielsen et al. (2010).

5.1.2 Microroughness in experimental samples

The data below were obtained from SEM and optical microscope (OM) images (see discussion in section 5.1.3). The type of images used is specified in each diagram. In the diagram below are reported values of ω_0 of experimental samples vs. the power dissipated at steady-state during each experiment.

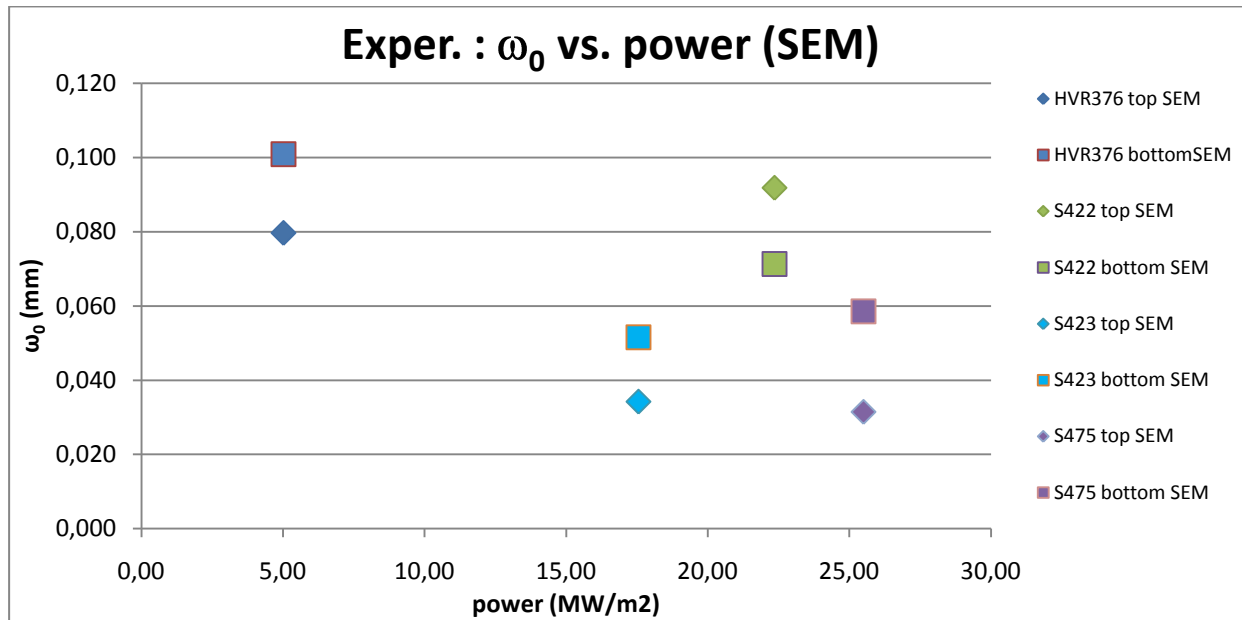


Figure 47 Experimental ω_0 versus frictional power: a scatter in S422 data is visible, but for the others experiments trend is respected

The ω_0 decreases with increasing power dissipated, though in experiment S422 the frictional power dissipated (22 MW/m²) is slightly out of this trend (see section 4 for discussion). Experiment S475, performed at $V = 6.5$ m/s and 30 MPa normal stress, has the highest frictional power dissipated (25.50 MW/m²) at steady-state and the lowest ω_0 . Experiment HVR376 performed at $V = 1.3$ m/s and 20 MPa normal stress has the lowest frictional power dissipated (5.05 MW/m²) at steady-state and the highest ω_0 .

We compared our microroughness data obtained from experiments performed on tonalite with SHIVA with microroughness data from frictional melting experiments performed with the HV-1 in Kyoto on gabbro (for details about the gabbro experiments, see Nielsen et al, 2010). Gabbro has the following differences with respect to tonalite:

- Grain size about 1 mm
- Mineral Composition (33% anorthite, 37% diopside, 30% other)
- Different melting temperature: anorthite 1560°C and diopside 1400°C.

The experiments on gabbro were performed at lower normal stress (< 2 MPa) and slip rate (1.3 m/s) than the experiments performed on tonalite described here. This results in a smaller frictional power dissipated on the sliding surface (< 3.0 MW/m²). As we can see in the figure below, the characteristic asperities height of the pseudotachylyte-gabbro boundary (ω_0) is higher than in the case of pseudotachylyte-tonalite boundary, but the power dissipated during these experiments is lower, so the general trend of decreasing ω_0 with increasing frictional power density is confirmed.

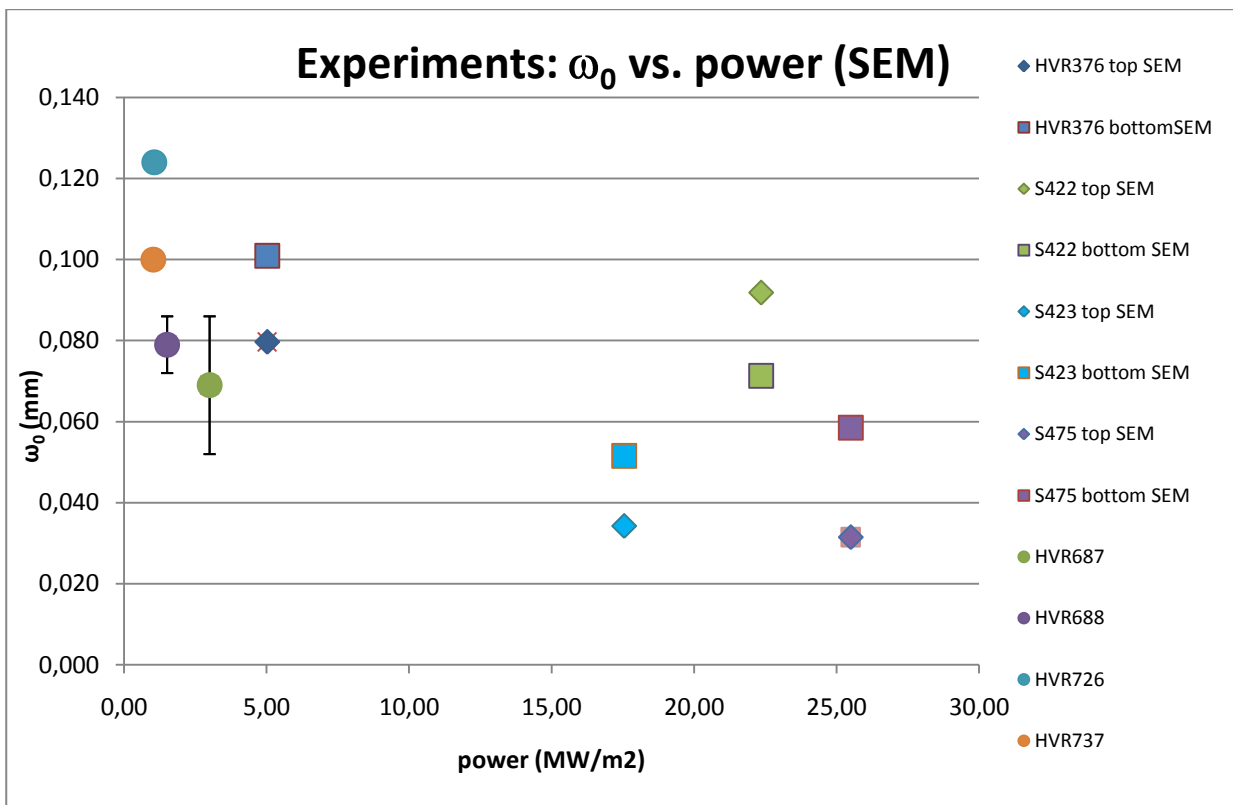


Figure 48 ω_0 versus frictional power: experimental data from tonalite and gabbro experiments. Also in this case trend is confirmed

We focus below on the dependence of λ_{ave} and ω_0 / λ_{ave} vs, frictional power density as we did for the natural samples. As shown in the diagram below, in the case of the tonalite experimental samples, λ_{ave} decreases slightly with frictional power density for power > 15 MW/m², but in general, the dependence of λ_{ave} vs. power seems poor.

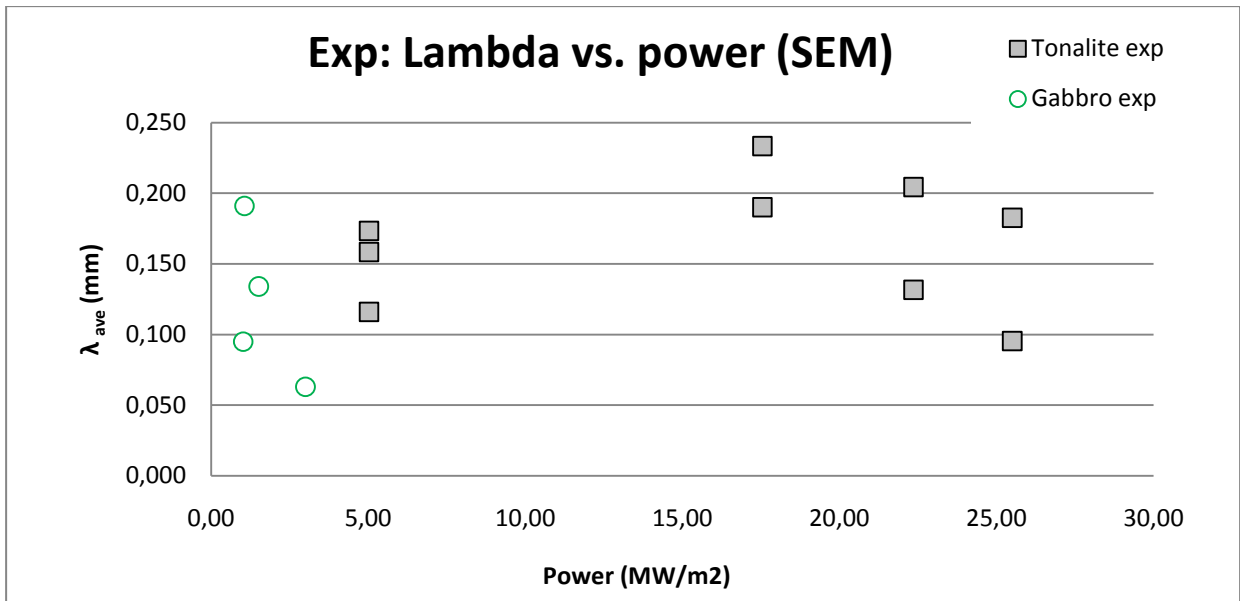


Figure 49 Characteristic average radii of asperities versus frictional power: also in this case, dependence of λ_{ave} of frictional power is poor

In the figure below, we plot ω_0/λ_{ave} vs, frictional power density: the dependence is very poor.

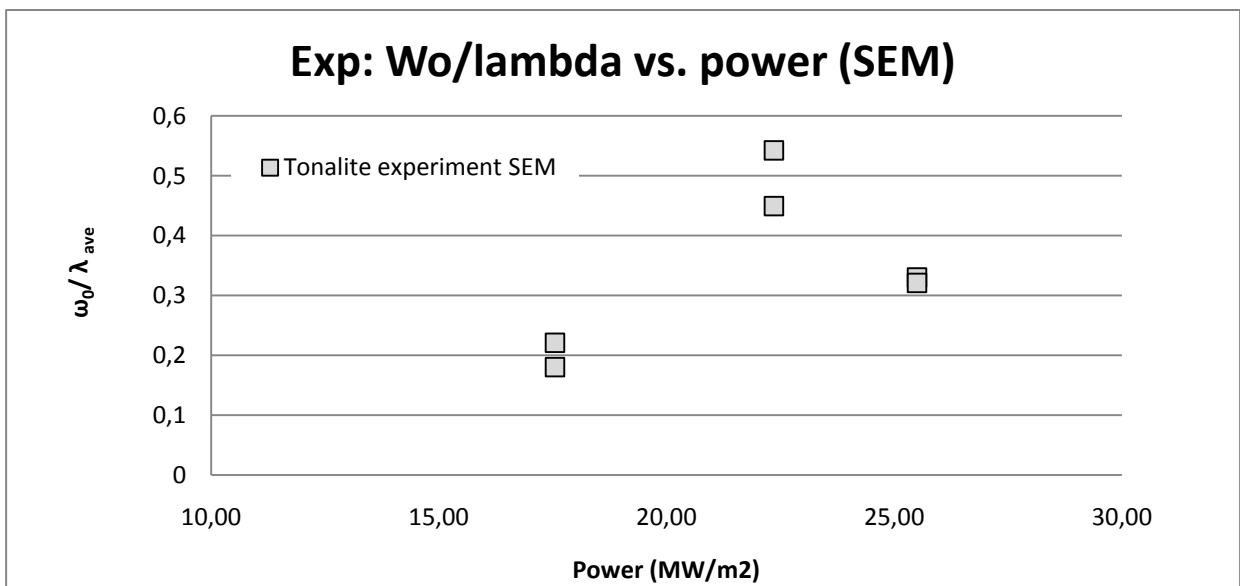


Figure 50 ω_0/λ_{ave} ratio shows as dependence of these two parameters is poor respect frictional power

In conclusion, as it was the case for the natural samples, the most robust parameter to describe the microroughness dependence with frictional power in experimental samples is ω_0 .

5.1.3 Experimental microroughness measurements from optical and BSE-SEM images

Microroughness of the pseudotachylite-tonalite boundary was obtained from OM images in natural samples and SEM images from experimental samples. To compare the two dataset, we measured the microroughness in experimental samples using OM images. Below we report the plot λ_{ave} vs. ω_0 measured in SEM and OM images.

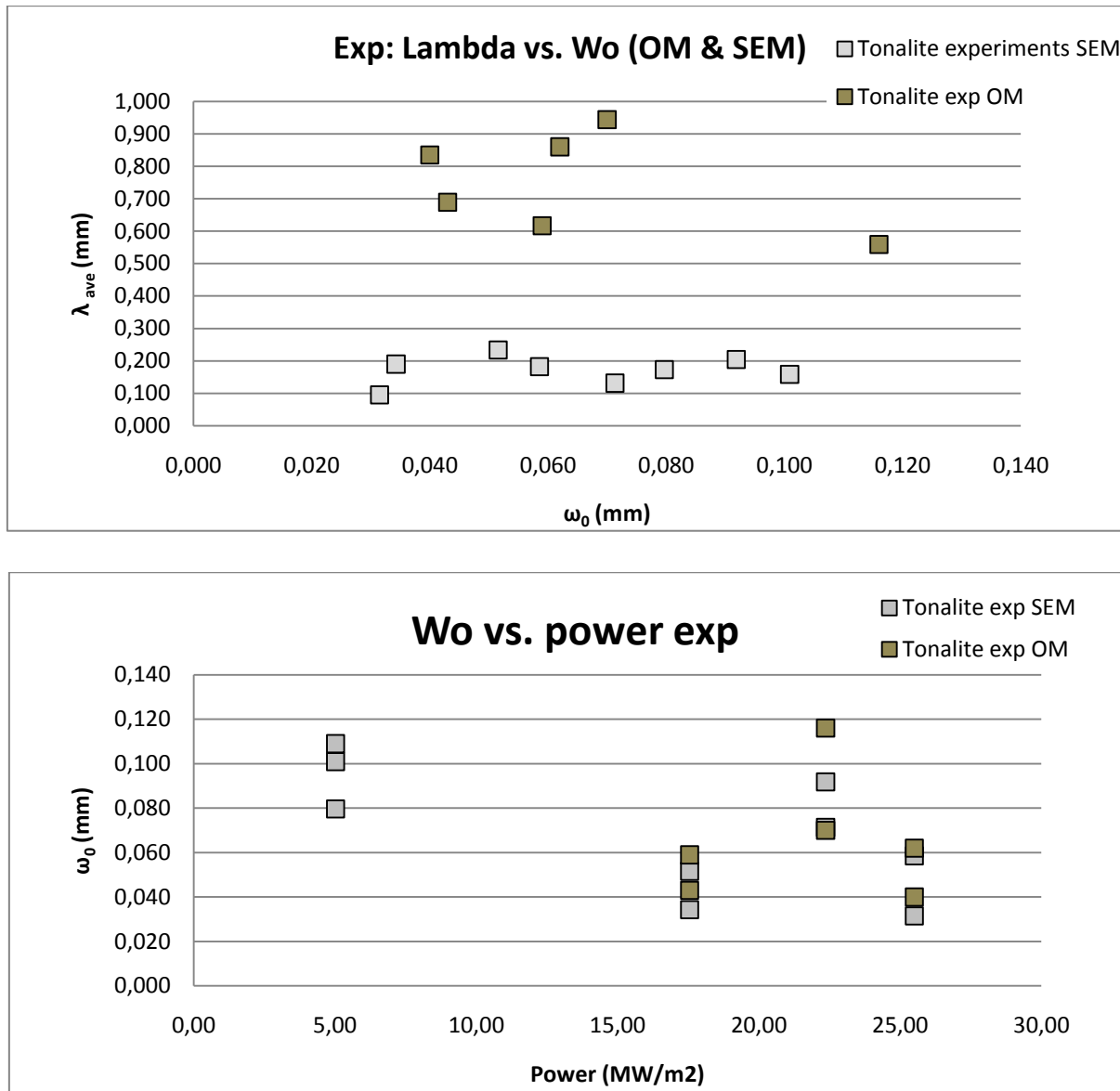


Figure 51 In the graph above, λ_{ave} are plotted against ω_0 value: a scatter between data collected from different image analyses is clear, but if only ω_0 values both for OM and SEM images are plotted, in the graph below, is shown as ω_0 is slightly affected by type of image used.

Clearly, the λ_{ave} of the microroughness is larger when it is measured from OM images. Instead, as shown in the second graph above (Fig.53), the measure ω_0 is slightly affected by the type of image used.

Summarizing:

- 1) λ_{ave} is almost independent of the frictional power dissipated in the experiments,
- 2) ω_0 depends on the frictional power dissipated in the experiments and on the structural domain in nature,
- 3) ω_0 measurements depends slightly on the technique used for its determination (OM and SEM images),

As a consequence in the section below we compared natural and experimental microroughnesses of ω_0 obtained from SEM and OM images.

5.1.4 Comparison between natural and experimental samples

In the plot below are reported all the ω_0 measurements for natural (tonalite) and experimental (gabbro and tonalite) samples.

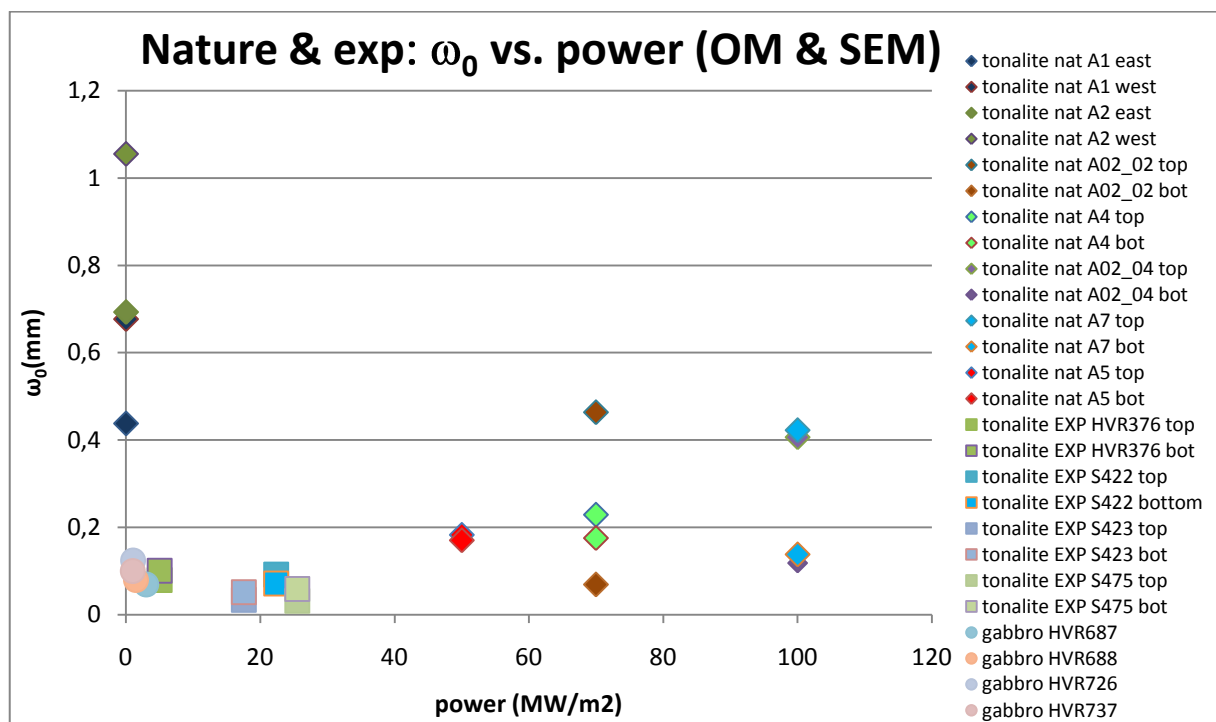


Figure 52 All data (natural and experimental) are plotted versus frictional power. Is visible the different magnitude between natural and experimental values. Is also visible how trend of ω_0 is present in both case.

The common feature is that ω_0 decreases with increasing frictional power density but natural ω_0 are from 3 to 10 times larger than experimental ω_0 . The difference in ω_0 can result for the reasons discussed below.

Experimental samples have a smooth initial sliding surface. The latter is polished with a grinder and a lathe to minimize the initial roughness (and asperity height) which might trigger spurious

vibrations at the initiation of sliding. Vibrations could result in sample failure (the samples are not confined in these experiments). In this case, the microroughness is mainly controlled by the grain size of the rock. Instead, in natural samples, beyond this, the roughness depends on the geometry of the fault surface (see section 3) (Bistacchi et al., 2011; Griffith et al., 2010). Experimental faults have a length of about 150 mm (the circumference of a hollow cylinder with 25 mm of radius), and, after polishing, a maximum asperity height of about 0.05 mm. Natural faults over a length along slip direction of 150 mm have an asperity height of the order of mm-cm (Bistacchi et al 2011). Clearly, fault surface roughness is, for a given fault length along strike, larger in natural than in experimental faults. As shown in the sketch below (Fig. 55), for experimental samples, surface refinement and roughness evolution due to frictional power dissipation during sliding is mainly controlled by grain size. But in the case of natural samples stem from the Gole Larghe Fault Zone, fault roughness is controlled by the evolution from pre-existing joints to faults, fracturing in compressional jogs, formation of en-echelon cracks, etc. (see section 3). As a further complication, the selected faults accommodated displacements ranging from 0.3 to 10 m: such large displacements allow the superposition of neutral or compressional domains with extensional domains. The resulting microroughness could be the result of an individual coseismic slip which, for instance, transferred compressional domains into extensional domains.

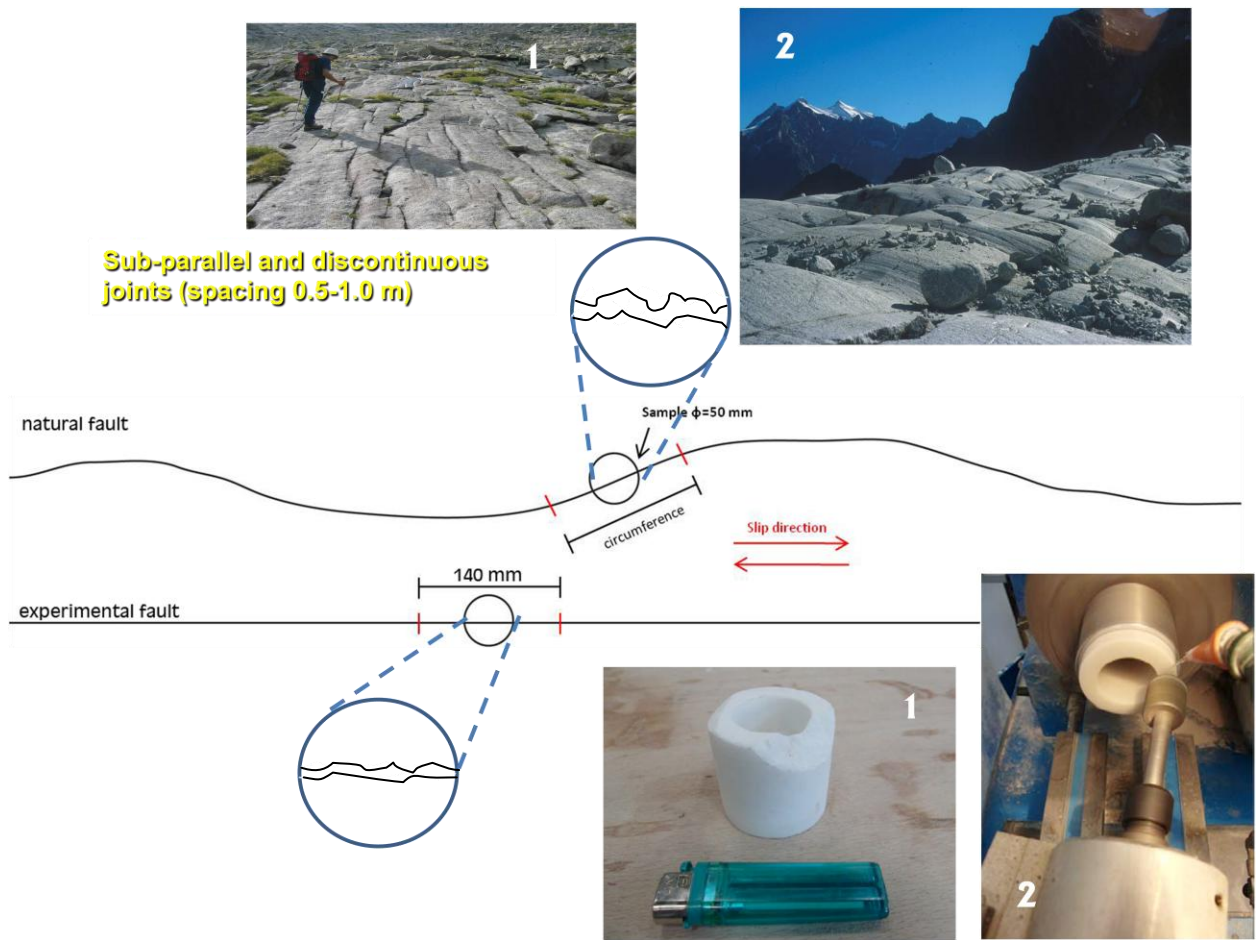


Figure 53 Simple sketch to show difference between natural and experimental case. Wavy trend of natural fault is exaggerated.

5.1.5 Estimate of frictional power dissipated during earthquakes

In this section we showed that the microroughness of natural and experimental faults described by ω_0 increases with the dissipated frictional power density. However, as visible in Fig. 54, a shift between natural and experimental ω_0 was also found. This shift implies that a quantitative estimate of the power dissipated during seismic slip at seismogenic depths is not possible yet. We can retrieve only qualitative observations about the trend of the microroughness with structural domains in nature.

Chapter 6 Conclusions

Pseudotachylytes are solidified friction melts produced during seismic slip. Since pseudotachylytes are co-seismic rocks, they yield information on earthquake source parameters. Today, it is possible to retrieve information about seismic source parameters (e.g., average stress drop, radiated energy, rupture velocity and directivity) by means of seismological investigations. However, the inversion of seismic waves allows to estimate the stress drop, and with some difficulties. The determination of the absolute value of stress, which controls the seismic energy budget, the co-seismic fault strength and triggers several physico-chemical processes possibly responsible for fault weakening, is out of the range of seismic inversion analysis.

In this thesis, we attempted to evaluate the frictional power density (τV) dissipated during an ancient seismic event at seismogenic depth (about 10 km) by measuring the microroughness of the pseudotachylyte-wall rock boundary. The basic idea is that higher is the frictional power dissipated during seismic slip, smoother (less rough) will be the boundary between the pseudotachylyte and the wall rock. Here we measured and compared the micro-roughness of natural (samples from the Gole Larghe Fault Zone, Italian Southern Alps) and experimental (obtained from experiments that reproduce seismic slip) pseudotachylytes. Natural pseudotachylyte samples were collected from different domains (pure tensile cracks, extensional, neutral and compressional domains) along selected wavy faults. The different domains should represent domains of different frictional power dissipation (i.e., compressional domain will dissipate larger power densities than extensional domains). For comparison, we performed experiments by imposing a target slip rate (6.5 m/s) but different normal stress ($\sigma_n = 20, 30, 40$ MPa, respectively). The combination of the two resulted in different powers dissipated on the sliding surface. We analyze OM images (natural samples) and BSE-SEM and OM images (experimental samples) of the redrawn pseudotachylyte-wall rock boundary. We used MatLab scripts to measure the microroughness of the profiles and determine the main surface roughness parameters: the characteristic asperity height (ω_0) and the average radius of each asperity (λ_{ave}). We found:

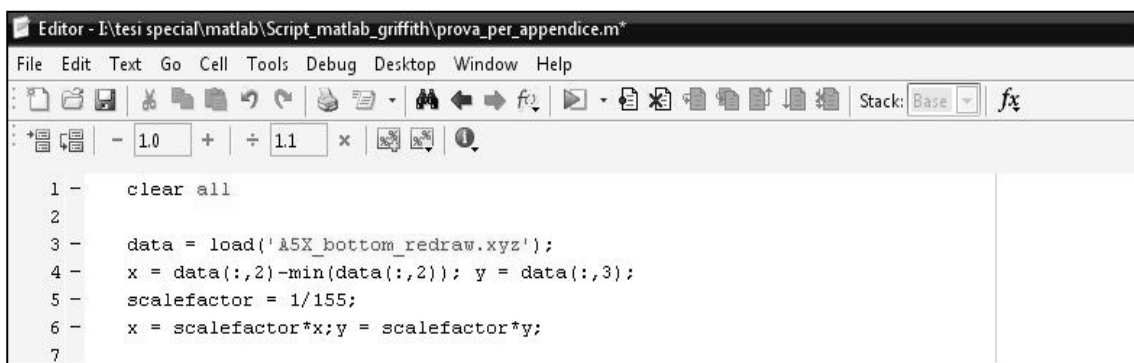
- ω_0 decreases with increasing power dissipated both in natural and experimental samples; this is consistent with theoretical studies.
- that λ_{ave} is related to ω_0 but the dependence with frictional power is poor; so in our analysis we considered only ω_0 to compare experimental and natural datasets.
- ω_0 in natural pseudotachylytes is 3 to 10 times larger than in experimental pseudotachylytes. Such a large mismatch does not allow a straightforward comparison of natural and experimental

measurements and impedes the quantification the frictional power dissipated at seismogenic depth during earthquakes.

Additional experiments and theoretical work are necessary to address the last issue

Appendix A: MatLab script

1. In the first part of script, data are translated in the origin and a scalefactor is calculated (i.e. from a scalefactor of 1 section measured 4676.089 mm along the x-axis, that's the maximum value of x. Section measured 30 mm, so to calculate scalefactor is necessary to make a ratio $4676.089/30=155$).

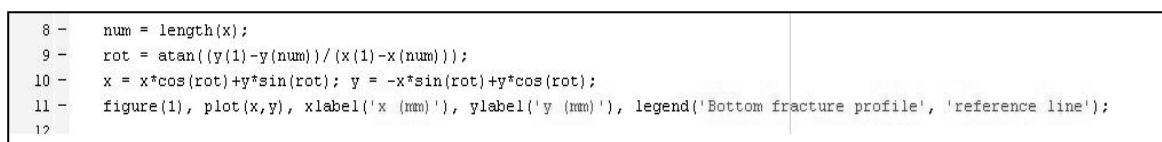


```

Editor - I:\tesi special\matlab\Script_matlab_griffith\prova_per_appendice.m*
File Edit Text Go Cell Tools Debug Desktop Window Help
Stack: Base
1 - clear all
2
3 - data = load('A5X_bottom_redraw.xyz');
4 - x = data(:,2)-min(data(:,2)); y = data(:,3);
5 - scalefactor = 1/155;
6 - x = scalefactor*x;y = scalefactor*y;
7

```

2. After, all the profile is rotated so the tips correspond with a reference line (fig. 1).



```

8 - num = length(x);
9 - rot = atan((y(1)-y(num))/(x(1)-x(num)));
10 - x = x*cos(rot)+y*sin(rot); y = -x*sin(rot)+y*cos(rot);
11 - figure(1), plot(x,y), xlabel('x (mm)'), ylabel('y (mm)'), legend('Bottom fracture profile', 'reference line');
12

```

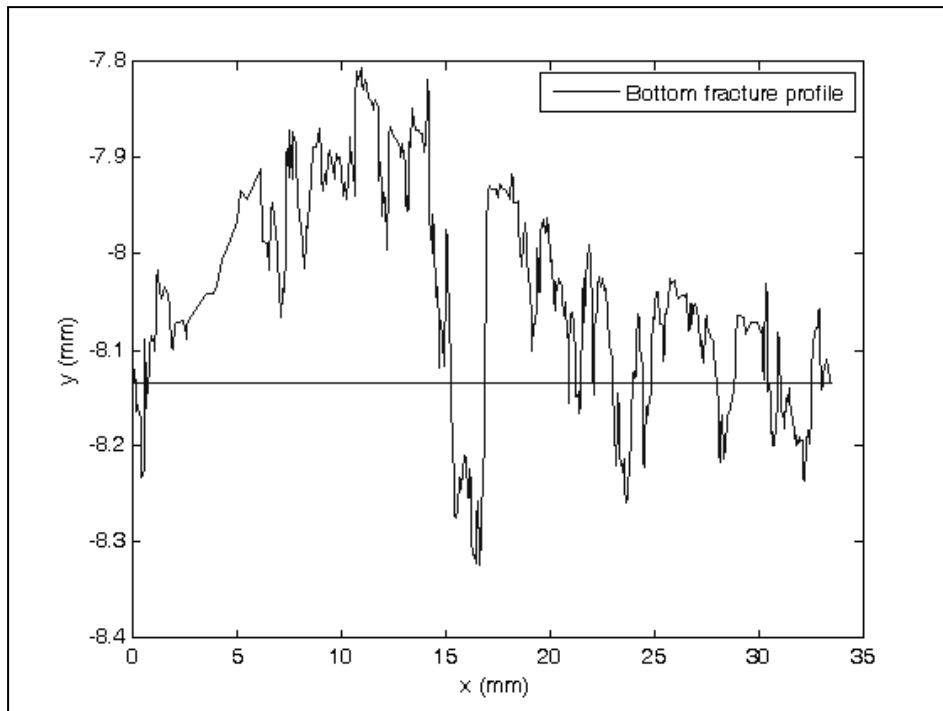


Figure 54 Example of fracture profile after tilting of tip-end of profile respect a reference line.

3. In this part a “for” loop is used to resort data so that points are increased in x (i.e. if two dapoints in x are coincident, one point are moved of certain quantity along x-axis). Two figure are plotted with “fracture profile after sorting” (fig.2).

```

13 - XY = sortrows([x y]);
14 - x1 = XY(:,1); y1 = XY(:,2);
15 - for m = 1:length(x1)-1
16 -     if x1(m)==x1(m+1)
17 -         x1(m+1)=x1(m)+0.01*mean(diff(x1));
18 -     end
19 - end
20 - figure(2), plot(x1,y1, 'r'), axis equal;
21 - xlabel('x (mm)'), ylabel('y (mm)'), title('Bottom fracture profile after sorting');
22
23
24 - ref =mean(y1);
25 - hold on, plot(x1, ref), legend('Bottom fracture profile', 'reference line');
--

```

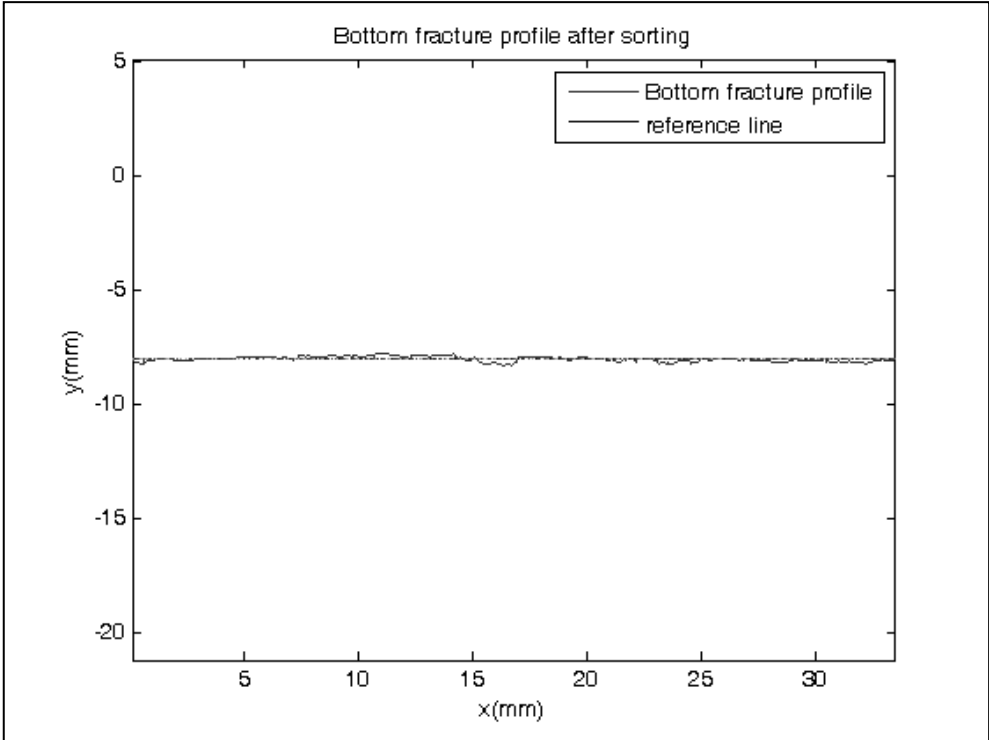


Figure 55 Example of fracture profile after sorting data along x-axis and plotted respect a referenced line.

4. Here is calculated the moving average. If you put a moving average=1 the profile is unfiltered, while if you put moving average=10 is totally filtered. Drawing, are inserted errors, so is necessary interpolate datapoints with moving average. In this work we used an average of moving average between values of 3, 4 (fig. 3) and 5.

```
32 - figure(4)
33 - lm = 4;
34 - a=1;
35 - b = (1/lm)*ones(1, lm);
36 - z = filter(b,a,z_rough);
37 - plot(x1, z, 'r'), xlabel('x(mm)'), ylabel('y(mm)'), title ('Bottom fracture profile after smoothing')
```

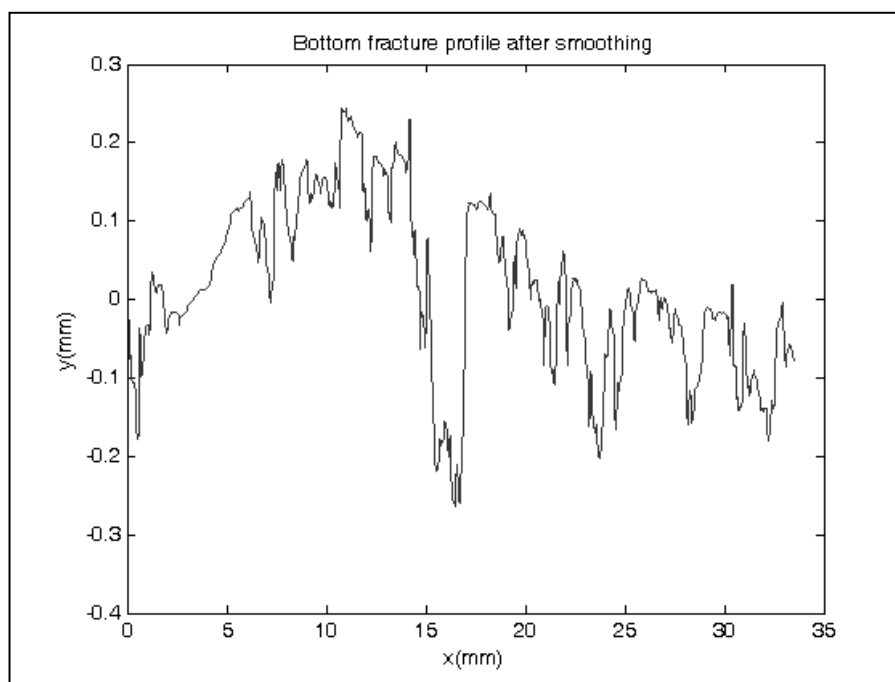


Figure 56 Example of fracture profile after application of moving average (lm=4).

5. After smoothing, script calculates local maxima in the profile. Profile is treated as a frequency. For every asperity present along profile, is calculated the radius of curvature at peaks and the base radius, where “kZ” is in a range of +1;-1 to find horizontal distance from peaks to inflection point in positive and negative direction, respectively.

```

39 - [lmval, i]=lmin(z,5);
40 - cX = x;
41 - cZ = z;
42 - i_top=i;
43
44 - for j = 2:length(x)-1
45 -     dcX(j) = (cX(j+1)-cX(j-1));dcX(1)=mean([dcX(2) dcX(end)]);
46 -     dcZ(j) = (cZ(j+1)-cZ(j-1));dcZ(1) = mean([dcZ(2) dcZ(end)]);
47 -     dsX(j) = abs(x(j)-x(j-1))+abs(x(j)-x(j+1));dsX(1)=mean([dsX(2) dsX(end)]);
48 -     dsZ(j) = abs(z(j)-z(j-1))+abs(z(j)-z(j+1));dsZ(1)=mean([dsZ(2) dsZ(end)]);
49 - end
50 - ds = sqrt(dsX.^2+dsZ.^2);
51 - tX = dcX./ds;
52 - tZ = dcZ./ds;
53 - for j = 2:length(x)-2
54 -     kX(j) = (tX(j+1)-tX(j-1))./ds(j);kX(1)=1;
55 - end
56
57 - %*****radius of curvature (R)*****
58 - kappa = sqrt(kX(i).^2+kZ(i).^2);
59 - R = 1./kappa;
60
61 - %*****base radius (a)*****
62 - sgn = kZ./abs(kZ);

```

6. A histogram with value of ω_0 is plotted (fig. 4).

```

110 - z_s = z(i);
111 - %X = [-2 -1.5 -1 -0.5 0 0.5 1 1.5 2]*10^4-1;
112 - [H1, X] = hist(z_s, 20);
113 - rms_z = sqrt(1/length(z_s)*sum(z_s.^2));
114 - figure(5)
115 - subplot(211, bar(X, H1,1), xlabel('z (nm)'), ylabel('N'), title(['A5 bottom ', \omega_0 = ' num2str(rms_z) 'nm,']), axis square
116 - %*****
117

```

7. A histogram with λ_{ave} is plotted (fig.4).

```

70
71 *****approximate wavelength*****
72 - l = 1;
73 - while l <= length(R)
74 -     if R(l) > 1
75 -         R(l) = []
76 -     end
77 -     l = l+1;
78 - end
79 - lambda = R;
80 - [H2, X] = hist(lambda, 20);
81 - subplot 212, bar(X, H2, 1), xlabel('\lambda (mm)'), ylabel('N'), colormap('white'), axis square
82 - lm_ave = mean(lm);
83 - title(['A5 bottom' ', \lambda_{ave}= ' num2str(mean(lambda)) 'mm,']);
84 - *****
85
86 *****real asperity density (n)*****
87 - nt=length(i);
88 - ntop=nt./ (2*mean(a) * (max(x) -min(x)));
89 - *****
90 - *****
91 - *****
92

```

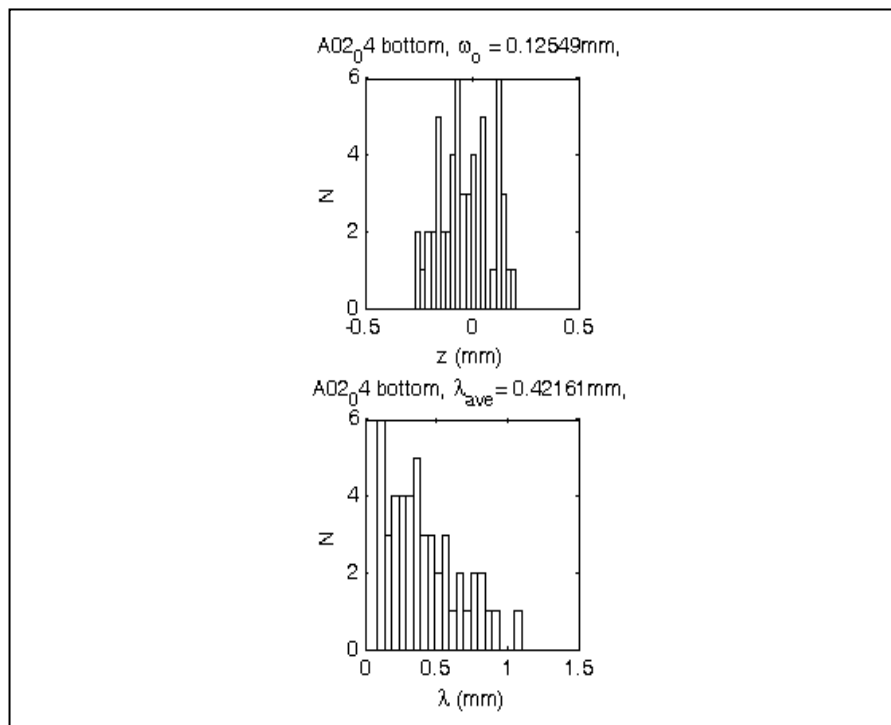


Figure 57 Histogram of rougness (upper) and average wavelength (down).

REFERENCES

- Bhat, H. S., R. Dmowska, J. R. Rice, and N. Kame, 2004. *Dynamic slip transfer from the Denali to Totschunda faults, Alaska: Testing theory for fault branching*, Seismol. Soc. Am. Bull., 94, S202–S213.
- Bistacchi, A., Griffith, W.A., Smith, S.A., Di Toro, G., Jones, R., Nielsen, S., 2011. *Fault roughness at seismogenic depths from LIDAR and photogrammetric analysis*. Pure and Applied Geophysics 168, 2345e2363.
- Brantut N, Schubnel A, Rouzaud JN, Brunet F, Shimamoto T, 2008. *High-velocity frictional properties of a clay bearing fault gouge and implications for earthquake mechanics*. J Geophys Res 113:B10401. doi:10.1029/2007JB005551
- Bianchi&Dal Piaz, 1948a . *Differenziazioni petrografiche e metamorfismi selettivi di contatto nel massiccio dell'Adamello*. Rend. Soc. Min.It, 5: 79-102
- Bianchi, A., Callegari, E., Jobstraibizer, P.G., 1970. *I tipi petrografici fondamentali del plutone dell'Adamello (tonaliti, quarzodioriti, granodioriti e loro varietà leucocrate)*. Mem. Ist. Geol. Min. Univ.Padova 27, 1–148.
- Brack, P., 1983. *Multiple intrusions — examples from the Adamello batholith (Italy) and their significance on the mechanisms of intrusions*. Mem. Soc. Geol. Ital. 26, 145–157.
- Callegari, E., Brack, P., 2002. *Geological map of the Tertiary Adamello batholith (Northern Italy) — explanatory notes and legend*. Mem. Sci. Geol. 54, 19–49.
- Candela, T., Renard, F., Bouchon, M., Brouste, A., Marsan, D., Schmittbul, J., and Voisin C. (2009), *Characterization of fault roughness at various scales: implications of three-dimensional high resolution topography measurements*, Pure and Applied Geophysics 166 (10), 1817-1851, DOI:10.1007/s00024-009-0521-2.
- Cowan DS, 1999. *Do faults preserve a record of seismic faulting? A field geologist's opinion*. J Struct Geol 21:995–1001
- Del Gaudio P, Di Toro G, Han R, Hirose T, Nielsen S, Shimamoto T, Cavallo A, 2009. *Frictional melting of peridotite and seismic slip*. J Geophys Res 114. doi:1029/2008JB005990
- Del Moro A., Ferrara G., Tonarini S. & Callegari E. (1985a) – *Rb-Sr systematics on rock from the Adamello batholith (Southern Alps)*. In Dal Piaz G. V. (Ed): Il magmatismo tardo alpino nelle Alpi. Mem. Soc. Geol. It., 26 (1983):261-284
- Del Moro A., Pardini G., Quercioli C., Villa I.M. & Callegari E., 1985b – *Rb/Sr and K/Ar chronology of Adamello granitoids, Southern Alps*. In Dal Piaz G.V. (Ed): Il magmatismo tardo alpino nelle Alpi. Mem. Soc. Geol. It., 26 (1983): 285-299
- Di Toro, G. & Pennacchioni, G., 2004. *Superheated friction-induced melts in zoned pseudotachylytes within the adamello tonalites (Italian Southern Alps)*, J. Struct. Geol., 26, 1783–1801.
- Di Toro, G., Nielsen, S. & Pennacchioni, G., 2005. *Earthquake rupture dynamics frozen in exhumed ancient faults*, Nature, 436, 1009–1012.

- Di Toro, G., Pennacchioni, G. & Teza, G., 2005. *Can Pseudotachylyte be used to infer earthquake source parameters? An example of limitations in the study of exhumed faults*, *Tectonophysics*, **402**, 3-20
- Di Toro, G., Hirose, T., Nielsen, S., Pennacchioni, G. & Shimamoto, T., 2006a. *Natural and experimental evidence of melt lubrication of faults during earthquakes*, *Science*, **311**, 647–649.
- Di Toro, G., Hirose, T., Nielsen, S., Shimamoto, T., 2006b. *Relating high-velocity rock friction experiments to coseismic slip*. In: Abercrombie, R., McGarr, A., Di Toro, G., Kanamori, H. (Eds.), *Earthquakes: Radiated Energy and the Physics of Faulting*, vol. 170. American Geophysical Union, Washington D.C, pp. 121e134.
- Di Toro G, Nielsen S, Pennacchioni G (2009). *Pseudotachylytes and earthquake source mechanics*. In: Fukuyama E (ed) *Fault-zone properties and earthquake rupture dynamics*. International Geophysics Series. Elsevier, Amsterdam, pp 87–133
- Di Toro, G., Niemeijer, A., Tripoli, A., Nielsen, S., Di Felice, F., Scarlato, P., Spada, G., Alessandroni, R., Romeo, G., Di Stefano, G., Smith, S., Spagnuolo, E., Mariano, S., 2010. *From field geology to earthquake simulation: a new state-of-the-art tool to investigate rock friction during the seismic cycle (SHIVA)*. *Rendiconti Lincei*, 1e20.
- Di Toro, G., Han, R., Hirose, T., De Paola, N., Nielsen, S., Mizoguchi, K., Ferri, F., Cocco, M., Shimamoto, T., 2011. *Fault lubrication during earthquakes*. *Nature* 471, 494e498. doi:10.1038/nature09838.
- Goldsby DL, Tullis TE, 2002. *Low frictional strength of quartz rocks at subseismic slip rates*. *Geophys Res Lett* 29. doi:10.1029/2002GL01240
- Goldsby, D.L., Tullis, T.E., 2011. *Flash heating leads to low frictional strength of crustal rocks at earthquake slip rates*. *Geology* 334, 216e218.
- Greenwood, J., 1992. *Contact of rough surfaces*, in *Fundamentals of Friction: Macroscopic and Microscopic Processes*, eds Singer, I. & Pollock, H., Kluwer, Dordrecht.
- Griffith W. A., S. Nielsen, G. Di Toro and S. A. F. Smith, 2010. *Rough faults, distributed weakening, and off-fault deformation*. *J.G.R.*, VOL. 115, doi:10.1029/2009JB006925, 2010
- Han R, Shimamoto T, Hirose T, Ree J-H, Ando J, 2007. *Ultralow friction of carbonate faults caused by thermal decomposition*. *Science* 316:878–881
- Heaton, T.H., 1990. *Evidence for and implications of self-healing pulses of slip in earthquake rupture*. *Physics of the Earth and Planetary Interiors* 64, 1e20.
- Hirose, T., Shimamoto, T., 2003. *Fractal dimension of molten surfaces as a possible parameter to infer the slip-weakening distance of faults from natural pseudotachylytes*. *Journal of Structural Geology* 25 (10), 1569e1574
- Hirose, T., Shimamoto, T., 2005b. *Slip-weakening distance of faults during frictional melting as inferred from experimental and natural pseudotachylytes*. *Bulletin of the Seismological Society of America* 95 (5), 1666e1673.
- John, B.E., Blundy, J.D., 1993. *Emplacement-related deformation of granitoid magmas, southern Adamello Massif, Italy*. *Geol. Soc. Amer. Bull.* 105, 1517–1541.
- Kanamori, H., Rivera, L., 2006. *Energy partitioning during an earthquake*. In: Abercrombie, R., McGarr, A., Di Toro, G., Kanamori, H. (Eds.), *Radiated Energy and the Physics of Faulting*. *Geophysical Monograph Series*, vol. 170. American Geophysical Union, Washington, D.C., pp. 3e13.

Lee, J.-J., and Bruhn, R.L., 1996. *Structural anisotropy of normal fault surfaces*. Journal of Structural Geology 18 (8), 1043-1059.

Kame, N., J. R. Rice, and R. Dmowska, 2003. *Effects of prestress state and rupture velocity on fault branching*, J. Geophys. Res., 108(B5),2265, doi:10.1029/2002JB002189.

McKenzie D, Brune JN, 1972. *Melting on fault planes during large earthquakes*. Geophys J R Astron Soc 29:65–78

Niemeijer, A., Di Toro, G., Nielsen, S., Di Felice, F., 2011. *Frictional melting of gabbro under extreme experimental conditions of normal stress, acceleration and sliding velocity*. Journal of Geophysical Research 116, B07404. doi:10.1029/2010JB008181.

Nielsen, S., and L. Knopoff, 1998. *The equivalent strength of geometrical barriers to earthquakes*, J. Geophys. Res., 103, 9953–9965.

Nielsen S, Di Toro G, Hirose T, Shimamoto T, 2008. *Frictional melt and seismic slip*. J Geophys Res 113:B01308. doi:10.1029/2007JB0051222008

Nielsen, S., Di Toro, G., Griffith, W.A., 2010a. *Friction and roughness of a melting rock interface*. Geophysical Journal International 182 (1), 299e310.

Pennacchioni G, Di Toro G, Brack P, Menegon L, Villa IM, 2006. *Brittle-ductile-brittle deformation during cooling of tonalite (Adamello, Southern Italian Alps)*. Tectonophysics 427:171–197

Persson, B., 2000. *Sliding Friction, Physical Principles and Applications*, Springer-Verlag, New York.

Pittarello L, Di Toro G, Bizzarri A, Pennacchioni G, Hadizadeh J, Cocco M, 2008. *Energy partitioning during seismic slip in pseudotachylite-bearing faults (Gole Larghe Fault, Adamello, Italy)*. Earth Planet Sci Lett 269:131–139

Power W.L., Tullis T.E., Brown S.R., Boitnott G.N., and Scholz C.H. (1987), *Roughness of natural fault surfaces*. Geophysical Research Letters 14 (1), 29-32.

Rice JR, 2006. *Heating and weakening of faults during earthquake slip*. J Geophys Res 111:B05311. doi:10.1029/2005JB004006

Riklin K.A., 1983. *Kontaktmetamorphose Permischer Sandstein in Adamello-Massiv (Nord-Italien)*. Ph.D Thesis; Diss. ETH nr. 7415, 140 pp., Zurich.

Sagy A., Brodsky E.E., and Axen G.J. , 2007. *Evolution of fault surface roughness with slip*. Geology 35 (3), 283-286.

Scholz, C.H., 2002. *The Mechanics of Earthquakes and Faulting*. Cambridge University Press, Cambridge.

Shand SJ, 1916. *The pseudotachylite of Parijs (Orange Free State) and its relation to “trap-shotten gneiss” and “flinty crush rock”*. Q J Geol Soc Lond 72:198–221

Sibson RH, 1975. *Generation of pseudotachylite by ancient seismic faulting*. Geophys J R Astron Soc 43:775–794

Shimamoto, T., Tsutsumi, A., 1994. *A new rotary-shear high-speed friction testing machine its basic design and scope of research*. Journal of the Tectonic Research Group of Japan 39, 65e78 (in Japanese with English abstract).

Spray JG, 1987. *Artificial generation of pseudotachylyte using friction welding apparatus: simulation of melting on a fault plane*. J Struct Geol 9:49–60

Spray JG, 1995. *Pseudotachylyte controversy: fact or friction?* Geology 23:1119–1122

Spray, J.G., 2005. *Evidence for melt lubrication during large earthquakes*, *Geophys. Res. Lett.*, **32**, L07301.

Stipp, M., Stünitz, H., Heilbronner, R., Schmid, S.M., 2002. *The eastern Tonale fault zone: a 'natural laboratory' for crystal plastic deformation of quartz over a temperature range from 250 to 700 °C*. J. Struct. Geol. 24, 1861–1884.

Stipp, M., Fügenschuh, B., Gromet, L.P., Stünitz, H., Schmid, S.M., 2004. *Contemporaneous plutonism and strike-slip faulting: a case study from the Tonale fault zone north of the Adamello pluton (Italian Alps)*. Tectonics 23, TC3004, doi:10.1029/2003TC001515.

Trener, G.B., 1912. *Die sechsfache Eruptionfolge des Adamello. Das postrhätische Alter der Tonalitzwillingsmasse*. Verh. Kais.-K. Geol. Wien 1912/13, 98–112.

Werling, E., 1992. *Tonale-, Pejo-und Judicarien-Linie: Kinematik, Mikrostrukturen und Metamorphose von Tectoniten aus räumlich interferierenden aber verschiedenaltigen Verwerfungszonen*. PhD thesis, ETH Zürich, 276pp.